Search for Dark Matter and Neutrinoless Double Beta Decay in XENON1T and Calibration of the Photosensors in XENONnT

DISSERTATION

zur
Erlangung der naturwissenschaftlichen Doktorwürde
(Dr. sc. nat.)

vorgelegt der
Mathematisch-naturwissenschaftlichen Fakultät
der
UNIVERSITÄT ZÜRICH

von
CHIARA CAPELLI
aus
Italien

PROMOTIONSKOMMISSION
Prof. Dr. Laura Baudis (Vorsitz)
Prof. Dr. Florencia Canelli
Dr. Michelle Galloway

ZÜRICH, 2020

Abstract

Numerous cosmological and astrophysical observations indicate that ordinary matter and radiation make up $\sim$15% of the total matter density of the Universe while the particle nature of the remaining matter, called dark matter, is unknown. One of the favourite candidates is the weakly interacting massive particle (WIMP). The XENON1T experiment used a dual-phase xenon time projection chamber (TPC) located underground in the Laboratori Nazionali del Gran Sasso (LNGS), Italy, to directly search for WIMP-nuclei interactions. With one tonne-year exposure in 278.8 days of data taking, XENON1T set the currently leading exclusion limit for the spin-independent WIMP-nucleon interaction cross section with a minimum of $4.1\times10^{-47}\,\mathrm{cm}^2$ for $30\,\mathrm{GeV/c}^2$ WIMPs at 90% CL, the best to date above $6\,\mathrm{GeV/c}^2$. In the context of the main WIMP search analysis, studies on electron drift velocity and their mean free path in liquid xenon are presented here, as well as on the activity of the ^{220}Rn source used to calibrate the electronic recoil band.

Neutrinoless double beta decay ($0\nu\beta\beta$) is a nuclear transition predicted by extensions of the Standard Model but never observed. Its positive detection would prove the violation of the total lepton number and the Majorana nature of neutrinos and, in addition, would provide information on the neutrino mass ordering. Experimentally, the direct dark matter detection and the $0\nu\beta\beta$ search present multiple common characteristics but also different requirements. The central part of this thesis describes a method developed to allow for the ^{136}Xe $0\nu\beta\beta$ search, at a Q-value of $(2457.83 \pm 0.37)\,\mathrm{keV}$, with the XENON1T detector and with dual-phase TPCs in general. Specifically, a signal saturation correction software technique is applied to restore the linearity of the detector in the region of interest of the $0\nu\beta\beta$ decay. A world-record energy resolution in liquid xenon of $\sigma/\mu = (0.80 \pm 0.02)\,\%$ at $2.46\,\mathrm{MeV}$ is achieved in XENON1T. As a proof of concept for dual-phase TPCs, a higher-level analysis is performed as well. Despite XENON1T not being competitive with currently leading double beta experiments, the study opens the path for the next generation experiments, as XENONnT and DARWIN, to be able to perform a simultaneous search for dark matter and $0\nu\beta\beta$.

XENONnT, the new experiment within the XENON programme, is installed and commissioned in the same place as XENON1T, following the upgrade of many subsystems. It exploits 8.4 t of liquid xenon, of which 5.9 t will be used as target. In case no WIMP signal will be discovered, the experiment will cover a region down to a cross section of $\sim 10^{-48}\,\mathrm{cm}^2$ for the spin-independent WIMP-nucleon interaction. The final part of this thesis focuses on the calibration of the photomultiplier tubes (PMTs) of the XENONnT detector. A total of 494 PMTs view the active volume of the detector, arranged in two hexagonal arrays, 253 in the top and 241 at the bottom. The calibration and monitoring of these photosensors is fundamental. The design of the PMT calibration system was finalised using GEANT4 optical simulations in order to have an uniform light collection on the arrays. The assembly and installation of the new TPC, carried out at LNGS, is described with particular attention to the optical fibres for the light calibration. During the first phase of the XENONnT commissioning, the connection of the photosensors and their readout were tested in-situ. Moreover, the software for the gain calibration of the 494 PMTs was developed, and it is currently used for the ongoing commissioning steps and will be employed for the upcoming calibrations during the lifetime of the experiment.

Acknowledgments

The PhD has been an amazing experience that I would highly recommend to the bravest. This was one of the most difficult and at the same time wonderful period of my life, but I would need to write a book to narrate it. So now I just want to thank many people who contributed to this achievement, each of them in different and important ways.

First of all, I would like to thank my supervisor, Prof. Dr. Laura Baudis, for giving me this unique opportunity. Through her example she taught me more than words could say. I hope this was just the beginning of a long lasting work relationship. I also want to thank the other members of my committee, Prof. Dr. Florencia Canelli and Dr. Michelle Galloway, for following my work and providing feedbacks through the last 4 years.
A special thank go to the astroparticle physics group at the University of Zurich, of which I am proud to be part of. It was a wonderful experience to meet such a melting pot of people and I am really glad to have worked and shared time with all of you. Thank you! Adam, we shared most of the PhD experiences along the way, including the bar appointments, and I consider myself very lucky for this. Giovanni, more than a colleague, you are a friend and, even if briefly, a flatmate. The one you complain about it but that you actually really like. I will keep complaining about you. Yanina, I could not wish to meet such a wonderful person and friend. I know you will continue to be my friend and part of my life. Francesco, firstly thanks for making the late evenings in the office productive, and then for being a friend still along the years.
My experience as a PhD student and researcher would not be so without the XENON family (as Elena likes to call it). All my fears have fallen thanks to the amazing people that welcomed, guided, helped and trusted me. A special mention also to the LNGS crew without whom I could not say that an earthquake, the assembly and a pandemic were not so bad after all.

Of course, my time in Zurich would have been much different and way less fun without many people I got the chance to meet and became friends with. I would need many more

pages to thank all of you, so I just say I am so happy to have seen the rise of the "In vino veritas" group!
Galeotta fu la festa di halloween where I met Marzia, Dario and Andrea and shortly after Iaros and Riccà (because Riccardo sounds aggressive). Thanks for all the fun, the support, the late nights and amazing memories, and what we cannot remember but I am sure it was fun, but most important thanks for the support and the friendship.
Myriam, meeting you in Zurich was very unexpected and I am really glad of it.

Finally, I want to thank the people who were not physically present in Zurich during the last years but without whom I could not keep up to this moment.
Federica, Andrei, Valeria, thanks for always being there for me. For our incredible adventures around the world and at home. Being your friend opened a world to me I could not know otherwise. I am looking forward to book our rooms in a retirement home on a beach.
I want to spend a few last words to thank my family. You have always supported and encouraged me to pursue my dreams, even when they brought me far away from you. To my mother, who always believed I could do the impossible if I tried and who would listen for hours about a world so far from hers to be part of mine, I want to dedicate this thesis.

Contents

Abstract I

Acknowledgments III

Introduction 1

1 Dark Matter and Neutrinos 2

1.1 Dark Matter 2

1.1.1 Evidence 2

1.1.2 The WIMP Miracle 4

1.1.3 Detection Methods 6

1.2 Neutrino Physics 11

1.2.1 Flavour Oscillations 11

1.2.2 Dirac and Majorana Neutrinos 15

1.3 Neutrinoless Double Beta Decay 18

1.4 $0\nu\beta\beta$ Experimental Overview 22

1.5 Simultaneous Search for Dark Matter and $0\nu\beta\beta$ 26

2 The XENON Dark Matter Project **28**

2.1 Liquid Xenon as Detection Medium 29

2.2 The XENON1T Experiment 33

2.2.1 The Time Projection Chamber 33

2.2.2 Spin-Independent WIMP-Nucleon Cross Section 35

2.3 The XENONnT Experiment 40

2.3.1 Overview 40

2.3.2 The Time Projection Chamber 41

2.3.3 Physics Reach 43

3 Signal Reconstruction in the MeV Energy Range 45
3.1 Signal Reconstruction in XENON1T 45
3.2 High Energy Reconstruction 47
    3.2.1 Saturation Correction 48
    3.2.2 Additional Corrections 51
3.3 Electronic Recoil Energy Calibration 53
    3.3.1 Energy Reconstruction and Resolution 54
    3.3.2 Low Gain and Low Anode Tests 60
3.4 Outlook 61

4 Neutrinoless Double Beta Decay Search in XENON1T 63
4.1 Data Selection and Efficiency 64
    4.1.1 Fiducial Volume 69
    4.1.2 Total Acceptance 72
4.2 Background Model 73
4.3 Preliminary Results and Outlook 77

5 Building XENONnT 80
5.1 The Light Calibration System 80
    5.1.1 Optical Simulations 82
    5.1.2 Optical Fibres 86
5.2 TPC Assembly and Installation 88
    5.2.1 Assembly Above Ground 89
    5.2.2 Installation Underground 92
    5.2.3 First PMT Commissioning 95
5.3 PMT Gain Calibration 99
    5.3.1 Model Independent Method 99
    5.3.2 Software and First Results 101
5.4 Outlook 104

6 Conclusions 106

A The Xurich-II Dual-Phase TPC 109
A.1 Detector Characterisation 109
A.2 Measurements with Electronic Recoil Sources 111

B ^{220}Rn Calibration: Detector Operation 114

List of figures **117**

List of tables **120**

Bibliography **121**

Introduction

I conducted my Ph.D. work in the group of Prof. Dr. Laura Baudis at the University of Zürich, during which I was involved in the dark matter search program with the XENON collaboration. During the last four years I performed studies on xenon properties with the Xurich-II experiment located at the University of Zürich. I have been working on the XENON1T data analysis and on the XENONnT detector upgrade and software development. The majority of the work was performed at the University of Zürich; additionally, I carried out hardware work and shift at the Laboratori Nazionali del Gran Sasso, Italy. I have also spent a month-long secondment with the XENON group at Columbia University, USA.

This thesis is organised into five main chapters. A summary of the dark matter evidence and the WIMP direct detection is given in the first part of chapter 1. In the second part of the chapter an overview of neutrino physics and $0\nu\beta\beta$ decay is given, and the current experimental landscape is reviewed. The common characteristics and differences between dark matter and $0\nu\beta\beta$ search experiments are also presented. In chapter 2, the signal generation in liquid xenon and the time projection chamber (TPC) working principle are described. The design of the XENON1T and XENONnT TPCs with the latest WIMP search results and future projections are given in this chapter. The main content of the Ph.D. work starts in chapter 3, where the software development for the signal reconstruction at the ^{136}Xe Q-value is described, as well as the procedure for the electronic recoil energy reconstruction and calibration with the resulting energy resolution. In chapter 4 the high-level analysis for the $0\nu\beta\beta$ decay search with XENON1T is described. The results prior to unblinding are reported. The work performed for the XENONnT experiment is described in chapter 5. Here the design, hardware and the development of the software for the light calibration system of the photosensors is presented, along with the installation of the TPC performed at the Laboratori Nazionali del Gran Sasso. Finally, the conclusions are given in chapter 6. In appendix A the work performed on a small dual-phase TPC at the University of Zürich is reported. Appendix B describes the study performed on the acquisition of ^{220}Rn calibration data.

CHAPTER 1

Dark Matter and Neutrinos

This chapter provides an introduction to dark matter (DM), section 1.1, with a focus on the weakly interacting massive particle (WIMP) and the current status of the direct detection search. Section 1.2 summarises neutrino physics and open questions in the field. An overview on the neutrinoless double beta decay ($0\nu\beta\beta$) and the status of the current experimental search are given in sections 1.3 and 1.4. Finally, in section 1.5 a summary of the characteristics that make an experiment suitable for both DM and $0\nu\beta\beta$ search is presented.

1.1 Dark Matter

Cosmological observations indicate that the majority of the constituents of the Universe is unknown. The standard model of cosmology, Λ Cold Dark Matter (ΛCDM), predicts that ordinary matter and radiation make up ~5% of the Universe while dark matter accounts for ~27% of its density (overall density of matter and energy, while it constitutes ~84% of the total matter density). The remaining ~68% is constituted by dark energy [1].

1.1.1 Evidence

The existence of dark matter was first suggested by F. Zwicky in 1933 after observing the velocity dispersion of galaxies in the Coma cluster [2]. The measured gravitational mass resulted to be at least 400 times larger than expected from the visible mass alone. Since then, through several cosmological and astrophysical observations, it was shown that dark matter constitutes about 84% of the matter in the Universe, more than 5 times the amount of the luminous baryonic mass.

Further evidence was provided in 1978, when V. Rubin et al. studied the dependency of the rotation curves of stars on the distance from the galactic centre [3]. In figure 1.1

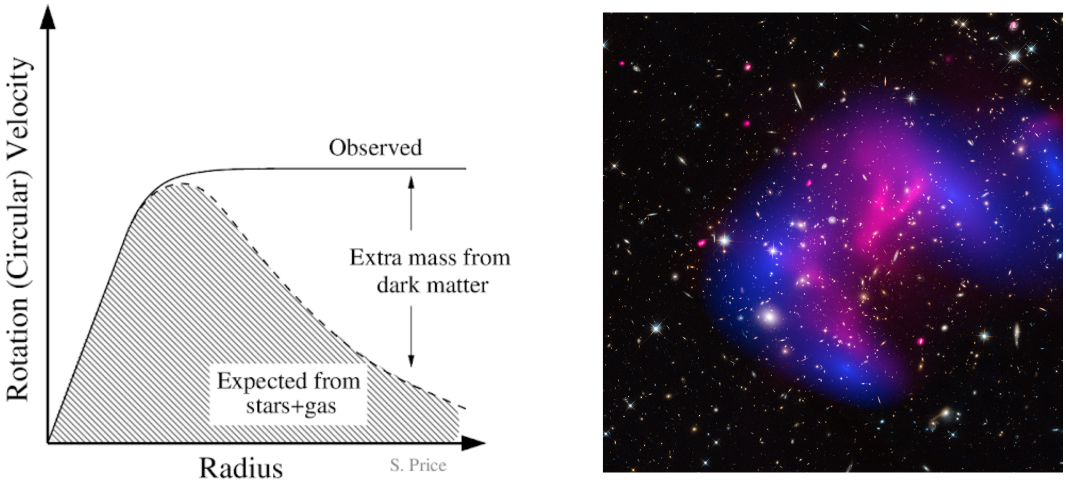

Figure 1.1: Left: sketch of the galactic rotation curve as expected from visible matter in stars and gas (dashed-shaded) and the observed trend. The gap can be explained by the presence of DM. Picture from [9]. Right: galaxy cluster MACS J0717.5+3745 [10]. The pink distributions are hot gas, baryonic matter, detected by the Chandra observatory in X-rays. The blue areas are reconstructed from gravitational lensing and show where most of the mass in the clusters is concentrated. An optical image from the Hubble Space Telescope shows the galaxies in orange and white. Credit: X-ray: NASA/CXC/Ecole Polytechnique Federale de Lausanne, Switzerland/D.Harvey & NASA/CXC/Durham Univ/R.Massey; Optical & Lensing Map: NASA, ESA, D. Harvey (Ecole Polytechnique Federale de Lausanne, Switzerland) and R. Massey (Durham University, UK).

on the left a sketch of this dependence is shown. The curve saturates at large radii in contradiction to what is expected from the Newton's gravitation law taking into account only the visible matter [4]. The gap between the expected and the observed trend is explained by assuming the presence of DM. This result is confirmed by other cosmological observations like gravitational lensing [5], stars distributions and X-ray spectroscopy [6, 7]. Another evidence comes from the observation of the colliding galaxy clusters [8], shown in figure 1.1 on the right, obtained from the comparison of X-ray and gravitational lensing measurements. The optical image showing the galaxies is also overlapped.

Beside the observations on galaxies and clusters, evidence for DM comes also from anisotropies in the cosmic microwave background (CMB) and the structure of the Universe. The variations in the CMB provide information on the density distribution and perturbations during the recombination time, when charged electrons and nuclei first became bound to form electrically neutral atoms [11, 12]. Latest measurements from the Planck experiment indicate that the temperature fluctuations in the CMB are in the order of 10^{-5} and produce a series of peaks in the angular power spectrum, as shown in figure 1.2. If the presence of dark matter is included in the standard ΛCDM cosmology model, the prediction is matching the observed data. This result gives indication of a flat Universe

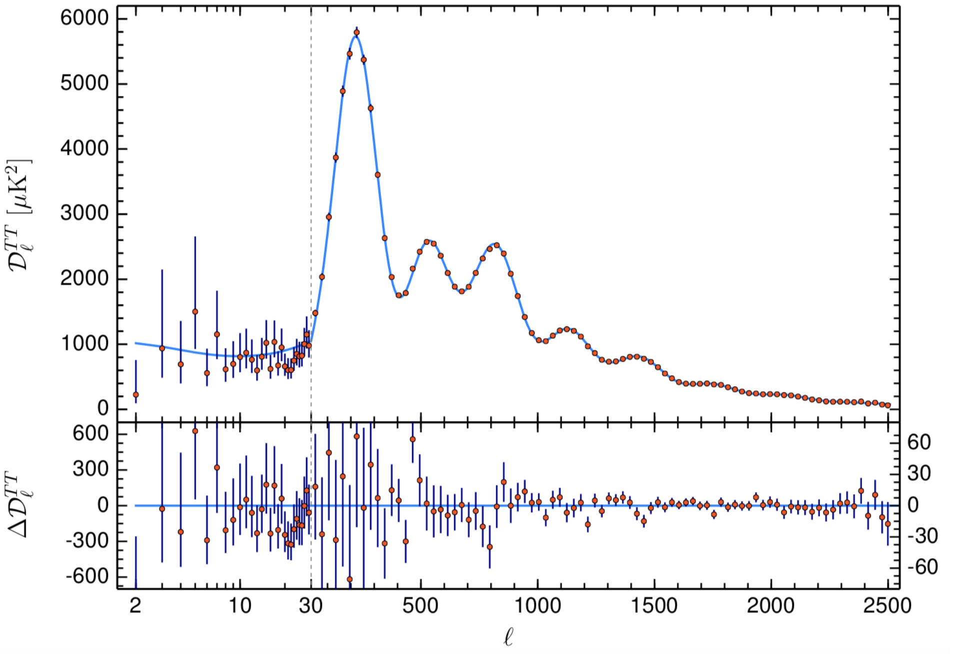

Figure 1.2: Temperature power spectrum as function of the multipole moment, ℓ, measured by the Planck experiment (blue points), with the best-fit from the ΛCDM model (red line). Residuals between data and model are shown in the bottom panel. Figure from [13].

with a dark matter density about five times higher than that of baryonic matter [13]:

$$\Omega_{\mathrm{DM}}h^2 = 0.120 \pm 0.001 \tag{1.1}$$

where Ω_{DM} is the dark matter density parameter and h is the dimensionless Hubble parameter.

The current large scale structure of the Universe requires an early beginning. Structure formation due to baryons is suppressed before the recombination, due to the photon pressure working against the growth of density perturbations [14]. This is not the case for DM particles, which may start forming structures at an earlier stage. In particular, structure formation requires non-relativistic DM and thus rules out relativistic candidates such as light neutrinos.

1.1.2 The WIMP Miracle

Some properties of DM can be inferred from the cosmological observations and thus it is possible to point few candidates out. The DM candidates should be non-baryonic, electrically neutral, stable and interacting gravitationally and possibly also weakly. The two primary candidates are axions and weakly interacting massive particles (WIMPs). Axions include a wide set of possible candidates that provide a solution to the strong CP problem, namely why the quantum chromodynamics (QCD) Lagrangian conserves CP symmetry with no fundamental reason. An explanation, proposed by Peccei and Quinn in 1977 [15], can be provided introducing an extra symmetry into the theory that leads to a new light pseudoscalar particle, the axion [16, 17].

One of the most attractive candidates is the WIMP, a particle not part of the Standard Model (SM) that is predicted by the supersymmetry [18] theory, among other extensions of the SM. This candidate follows from the *freeze-out* hypothesis according to which DM is a thermal relic of the early Universe. At the very beginning, all the particles are considered relativistic and in thermal equilibrium. While the Universe cools down, some particle species become non-relativistic and their number density reduces rapidly. Let us consider a particle χ with mass M_χ and annihilation cross section σ. Starting from the Boltzmann equation and assuming a single species annihilation of 2-to-2 particles, the number density n_χ is then given by [1]:

$$\frac{\mathrm{d}n_\chi}{\mathrm{d}t} - 3Hn_\chi = -\left\langle \sigma v \right\rangle \left(n_\chi^2 - n_{\chi(eq)}^2\right) \tag{1.2}$$

where $\langle \sigma v \rangle$ is the thermally averaged annihilation cross section times relative velocity and $n^2_{\chi(eq)}$ is the number density at equilibrium. Equation 1.2 shows that the time evolution at which the number density approaches the equilibrium is determined by the annihilation cross section and the particle flux, while a drop in density is due to Universe expansion and it depends on the Hubble rate ($H = (67.4 \pm 0.5)\,\mathrm{kms^{-1}Mpc^{-1}}$ [13]). As the Universe expands, the latter term starts to be dominant, the annihilation stops, and the remaining particles freeze out with a constant co-moving number density. This sequence is shown in figure 1.3. If the particle is stable then the relic density is what we measure today. Considering the annihilation cross section of the weak interaction:

$$\sigma_{EW} \approx 10^{-8}\,\mathrm{GeV}^{-2} \tag{1.3}$$

we obtain a relic density $\Omega_\chi \approx 0.3$, of the same order as the observed value $\Omega_{\mathrm{DM}} \approx 0.26$ [19]. This is referred to as *WIMP miracle*. Even though the mass density at the freeze-out is independent of M_χ, the WIMP mass is related to its abundance. From the present DM abundance it is thus possible to estimate a range for the WIMP mass, M_χ, from the GeV to ∼100 TeV.

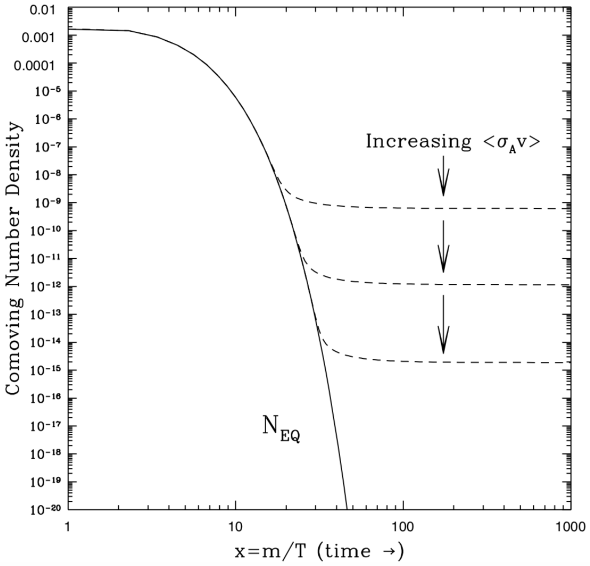

Figure 1.3: Equilibrium (solid line) and relic abundance (dashed lines) of WIMP particles. Figure and caption from [6] (originally from [18]). The x-axis (m/T) is the ratio between the WIMP mass, m, and the temperature, T, and it is proportional to the time starting from the Big Bang.

1.1.3 Detection Methods

There is no evidence so far for any type of DM interactions other than gravitational. Several methods and experiments are under investigation with this goal. DM searches are based on three main approaches and exploit different detection methods. An overview of the processes is shown in figure 1.4. In this section the indirect search and the production at colliders are introduced. More insights are provided for the direct detection method and the current state-of-art of direct DM experiments.

Indirect Search: DM particles could be detected through the self-annihilations products in astrophysical objects such as dwarf galaxies, the Sun or the galactic centre. Here the DM interaction rate is higher due to the enhanced DM density. The expected annihilation processes are:

$$\chi\chi \rightarrow \gamma\gamma, \gamma Z, \gamma H, q\bar{q}, W^{-}W^{+}, Z\bar{Z} \tag{1.4}$$

with the unstable states further decay into $e^{+}e^{-}, p\bar{p}, \gamma\gamma$. In 2009 the PAMELA [20] experiment reported a bump in the positron spectrum. However one of the main challenges in this type of search is the astrophysical background as the bump can be produced also by a nearby pulsar [21]. Results from the Fermi-LAT telescope [22] rejected the result and the positron excess remains inconclusive. The AMS [23] satellite is also looking for anti-fermions DM self-annihilations products. Earth Cherenkov telescopes like MAGIC [24], H.E.S.S. [25] and CTA [26] look for annihilation into gamma-rays. Moreover, the latter propagate in

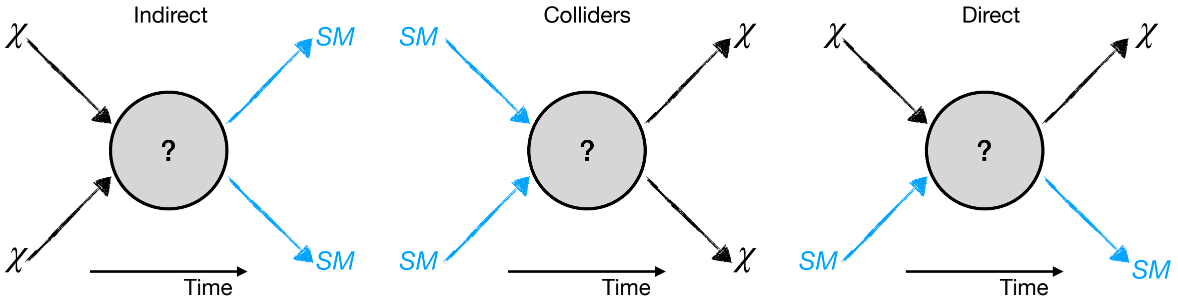

Figure 1.4: Three approaches for DM search: indirect detection (left), production at colliders (centre) and direct detection (right). The indirect detection looks for SM signals of DM annihilation from astrophysical objects. The production at collider, from collision of SM particles, results in missing energy in the final states. The direct search looks for signals of relic DM particles scattering off nuclei.

straight lines opening up the possibility to distinguish those from DM annihilation through directionality. So far, no evidence for indirect DM detection has been confirmed [27, 28].

Production at Colliders: High energy colliders, like the Large Hadron Collider (LHC) at CERN, through p-p collisions, are looking for new physics that also predicts new particles. The DM particle would escape the detector resulting in missing transverse energy and momentum. The possible combinations of final states depend on the considered model [29]. The energy available in the centre of mass of the collisions can prove different DM candidates, being a complementary method to other types of experiments. No signal has been detected so far [30, 31, 32]. Even if a new particle is discovered in colliders, its validity as DM candidate must be proven by direct detection.

Direct Search: If DM particles interact with the baryonic matter they could be directly detected by scattering off nuclei in Earth-based detectors. DM particles of the order $\mathcal{O}$(GeV) produce a nuclear recoil signal in the keV energy range. Thus scattering experiments measure mainly the interaction rate from which the DM-nucleon cross section is inferred. The recoiling nucleon can deposit energy through three channels: heat (or phonons), charge (or ionisation) and light (or scintillation). Several experiments are designed to exploit one or two of these channels. A summary of the main experiments with the particular channel used for the detection of the recoiling nucleon is shown in figure 1.5.

The WIMP differential recoil spectrum from a DM interaction can be written as [34]:

$$\frac{\mathrm{d}R}{\mathrm{d}E_{nr}} = \frac{\rho_0 M}{m_N M_\chi} \int_{v_{\mathrm{min}}}^{v_{\mathrm{esc}}} v f(v) \frac{\mathrm{d}\sigma}{\mathrm{d}E_{nr}} \mathrm{d}v \tag{1.5}$$

where E_{nr} is the energy of the nuclear recoil, M is the target mass, m_N the mass of the

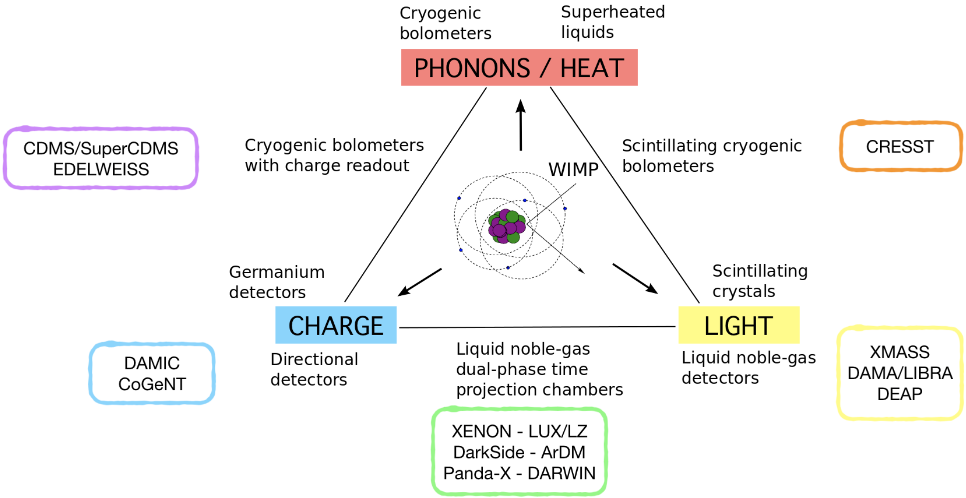

Figure 1.5: Energy deposition channels of a recoiling nucleon in direct detection search. Several experiments, mentioned in the coloured boxes, exploit one or two channels using different techniques. Figure modified and adapted from [33].

target nucleus and σ the scattering cross section. The astrophysical parameters describing the WIMP distribution are the local DM density ρ_0 and the normalised WIMP velocity distribution $f(v)$. A simplified model assumes DM is a collisionless gas with isotropic initial velocity. At equilibrium, the pressure of DM compensates the gravitational force pushing toward the centre of the DM halo. The density distribution scales as $\rho(r) \propto r^{-2}$, shaping an isothermal sphere in the galactic centre. The local DM density near the Sun can be inferred from the rotation curve measurements and a value of $\rho_0 = 0.3\,\mathrm{GeV cm^{-3}}$ is usually adopted[1], although with an uncertainty of ∼50% [35]. The WIMP velocity is assumed to follow the Maxwell-Boltzmann distribution:

$$f(v) = \frac{1}{\sqrt{2\pi\sigma_0}} \exp\left(-\frac{|v|^2}{2\sigma_0^2}\right) \tag{1.6}$$

where $\sigma_0 = \sqrt{3/2}v_c$ is the velocity dispersion and $v_c(r)$ the average circular velocity around the galactic centre of an object at distance r. For the Sun $v_c(r_{\mathrm{sun}}) \simeq 220\,\mathrm{km/s}$. The maximum velocity above which a body is not affected by the gravitational potential is the escape velocity $v_{\mathrm{esc}} \simeq 544\,\mathrm{km/s}$ [36]. The minimum WIMP velocity to produce a nuclear recoil of energy E_{nr} is $v_{\mathrm{min}} = \sqrt{m_N E_{nr}/2\mu^2}$, where μ is the reduced WIMP-nucleon mass.

The cross section σ in equation 1.5 depends on the assumption on the physics processes involved. In particular, if the WIMP interaction is spin-independent (SI) neutrons and protons contribute equally to the scattering process. If the interaction is spin-dependent (SD) only unpaired nucleon spins contribute to the scattering, meaning that only nuclei with

---

[1] Assuming c=1

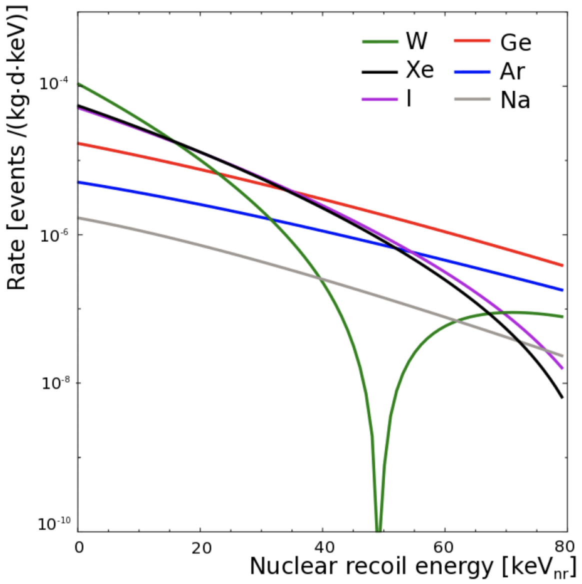

Figure 1.6: Differential event rate for the direct detection of a 100 GeV/c^2 WIMP with a SI cross-section of 10^{-45} cm^2 in experiments using tungsten (green), xenon (black), iodine (magenta), germanium (red), argon (blue) and sodium (grey) as target materials. Figure and caption from [33].

an odd isotopic number are sensitive to the interaction [33]. The differential WIMP-nucleon cross section $\mathrm{d}\sigma/\mathrm{d}E_{nr}$ can be written as sum of the SI and SD contributions:

$$\frac{\mathrm{d}\sigma}{\mathrm{d}E_{nr}} = \frac{m_N}{2\mu_N^2 v^2}[\sigma_0^{\mathrm{SI}} \cdot F_{\mathrm{SI}}^2(E_{nr}) + \sigma_0^{\mathrm{SD}} \cdot F_{\mathrm{SD}}^2(E_{nr})] \tag{1.7}$$

where μ_N is the WIMP-nucleus reduced mass, $\sigma_0^{\mathrm{SI,\,SD}}$ are the cross sections at zero momentum transfer for SI and SD interactions, respectively, and $F_{\mathrm{SI,\,SD}}$ the nuclear form factors.

For the SI interaction, the cross section at zero momentum transfer is given by the following:

$$\sigma_0^{\mathrm{SI}} = \frac{4\mu^2}{\pi}[f^p Z + f^n(A-Z)]^2 \tag{1.8}$$

where A and Z are the mass and atomic number of the target nucleus, respectively. $f^{p,n}$ are the proton and neutron contributions to the total coupling strength. The assumption $f^p \approx f^n$ is commonly used and thus the dependence of the cross section on the number of nucleons is reduced to $\sigma_0^{\mathrm{SI}} \propto A^2$. The impact of the target isotopes' form factor and mass number on the DM rate is shown in figure 1.6 for a 100 GeV/c^2 WIMP and a cross section of 10^{-45} cm^2. Heavier targets are preferred for DM search due to the higher A. The form factor is responsible for the rate decreasing at higher recoil energies due to coherence loss.

For SD interactions, form factors are determined from the nuclear shell model [37] or chiral effective-field theory currents [38] calculations. The cross section can be expressed as:

$$\sigma_0^{\mathrm{SD}} = \frac{32}{\pi}\mu_N^2 G_F^2 [a_p \langle S^p \rangle + a_n \langle S^n \rangle]^2 \cdot \frac{J+1}{J} \tag{1.9}$$

where G_F^2 is the Fermi coupling constant, $a_{p,n}$ are the effective WIMP-proton/neutron couplings, J is the total nuclear spin and $\langle S^{p,n} \rangle$ are the expected spin values of the proton and neutron groups in the nucleus. Since $\langle S^{p,n} \rangle = 0$ for an even number of nucleons, only odd isotopes are sensitive to the SD interaction.

Different methods can be exploited for the direct DM detection. Experiments such as DAMA/LIBRA [39] and SABRE [40] use solid scintillation detectors to look for annual modulation of DM due to the Earth motion through the Milky Way. SuperCDMS [41], EDELWEISS [42] and CRESST [43] use the bolometric technique with charge or light readout and they are sensitive to low DM masses, $\mathcal{O}(1\,\mathrm{GeV})$. Silicon charged-coupled devices (CCDs) are employed by DAMIC [44] to detect the charge generated by low-DM particles. Superheated liquids are also used in experiments such as PICO-60 [45], which operates a bubble chamber filled with C_3F_8 to capture images and acoustic signals from bubble nucleation. Noble liquids are also used as targets. XMASS [46] and DEAP-3600 [47] observe the scintillation light in the xenon and argon liquid-phase, respectively. The best constraints on the SI WIMP-nucleon cross section come from the dual-phase xenon time projection chambers (TPCs) technology, from LUX [48, 49] and XENON [50, 51]. Dual-phase TPCs are used also with argon, as done by Dark-Side-50 [52].

Only DAMA/LIBRA claims the detection of DM modulation, but the corresponding WIMP-nucleon cross section has been ruled out by other experiments. The upper limits on the SI DM are shown in figure 1.7. The light-blue region indicates the irreducible background due to the neutrino flux from the Sun, the atmosphere and the diffuse supernovae background. The next generation of direct DM experiments, such as DARWIN [53], aim to reach this lower bound. A possible discrimination of this background can be provided by detectors capable of measuring the direction of the recoiling nucleus. Current R&Ds can pave the way to future large scale directional detectors, such as the CYGNUS network [54, 55].

Beside looking for different DM candidates, experiments built for DM direct detection are suitable for other rare-event searches. Another main topic of study in the astroparticle physics field is the neutrino. Particularly, both the search for the neutrinoless double beta decay process and the direct search of DM interactions with ordinary matter utilise ultra-low background detectors running in deep underground laboratories. Ideally it would be possible to search for both in DM and neutrinoless double beta decay, but so far it has not been demonstrated. In the rest of the chapter an overview on neutrino physics and

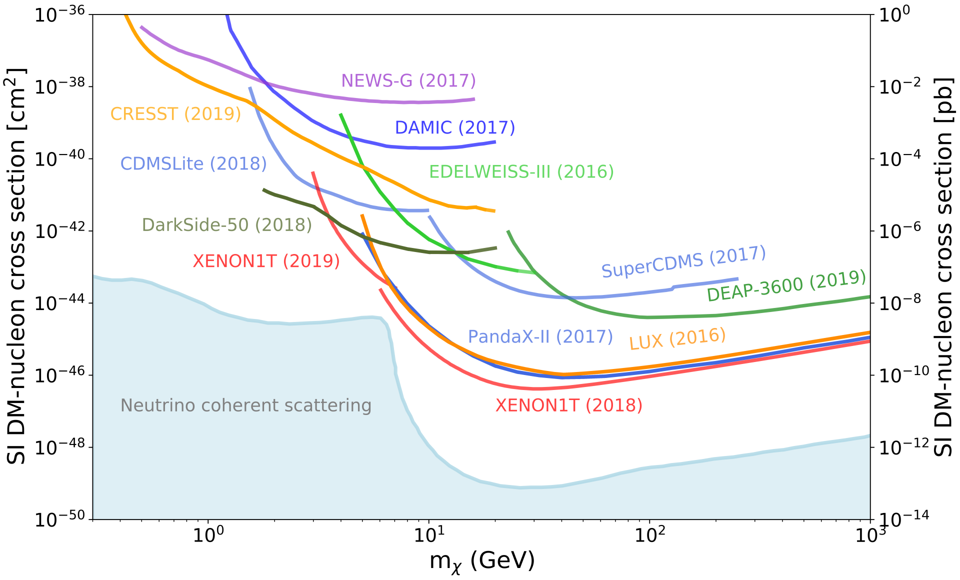

Figure 1.7: Upper limits on the SI DM-nucleon cross section as a function of the DM mass. Figure and caption from [1].

neutrinoless double beta decay process are described, concluding with a discussion on the challenges for a detector able to be at the forefront of DM and neutrinoless double beta decay search.

1.2 Neutrino Physics

In this section neutrinos, their oscillations and the mass ordering problem are described, with an introduction to the Dirac and Majorana formulations for the neutrino masses.

1.2.1 Flavour Oscillations

The first experimental evidence of the neutrino dates back to 1956, when F. Reines and C. Cowan [56, 57] observed the inverse beta decay caused by an anti-neutrino interaction ($\bar{\nu}_e + p \rightarrow n + e^+$). Similarly to the quark interactions through the CKM (Cabibbo–Kobayashi–Maskawa) mixing matrix, Pontecorvo in 1957 introduced the idea of flavour oscillations among neutrinos [58]. To measure the flux of electron neutrinos, ν_e, coming from the Sun, R. Davis conducted a radiochemical experiment in the late 1960s in the Homestake mine. He measured a solar flux of about 1/3 of the one predicted by the J. Bahcall solar model [59]. This discrepancy in the solar neutrino flux, known as Solar Neutrino Puzzle, was confirmed by the following experiments SAGE [60] and GALLEX/GNO [61]. In 1985 Mikheyev and Smirnov [62], expanding the work of Wolfenstein [63], noted that flavour oscillations can be modified when neutrinos propagate through matter. The phenomenon, called Mikheyev–Smirnov–Wolfenstein (MSW) effect, influences neutrinos emitted by the Sun on their way to detectors on Earth. In 1998 Super-Kamiokande announced the discovery of neutrino oscillations [64] studying high energy atmospheric neutrinos, ν_μ, and confirming the hypothesis of Pontecorvo. The solar neutrino discrepancy was solved in 2002 by the Sudbury Neutrino Observatory (SNO) collaboration [65]. The detector consisted of a vessel containing heavy water and the interactions were viewed by photomultiplier tubes (PMTs). The experiment was sensitive to all the neutrino flavour interactions. The missing ν_e transforms into another neutrino lepton flavour $\nu_e \to \nu_x$ following an oscillatory behaviour. More recently, in 2010 OPERA announced the measurement of a τ flavour particle starting from a pure ν_μ beam [66]. The following year, the T2K experiment [67, 68] measured the appearance of ν_e from a ν_μ beam.

For a non-zero mass, it is possible to define the flavour states $|\nu_\alpha\rangle$ as combination of the mass eigenstates $|\nu_i\rangle$:

$$|\nu_\alpha\rangle = \sum_{i=1}^{3} U_{\alpha i} |\nu_i\rangle \tag{1.10}$$

where the coefficients $U_{\alpha i}$ are elements of the PMNS (Pontecorvo-Maki-Nakagawa-Sakata) neutrino mixing matrix:

$$\begin{pmatrix} \nu_e \\ \nu_\mu \\ \nu_\tau \end{pmatrix} = \begin{pmatrix} U_{e1} & U_{e2} & U_{e3} \\ U_{\mu 1} & U_{\mu 2} & U_{\mu 3} \\ U_{\tau 1} & U_{\tau 2} & U_{\tau 3} \end{pmatrix} \begin{pmatrix} \nu_1 \\ \nu_2 \\ \nu_3 \end{pmatrix} \tag{1.11}$$

It follows that the flavour eigenstates $(\nu_e, \nu_\mu, \nu_\tau)$ do not coincide with the mass eigenstates (ν_1, ν_2, ν_3) and it can happen that a neutrino produced in a state α is measured, after a certain time, in a state β. Using the parametrisation of Chau and Keung [69] for three flavours, we can express the PMNS using three angles, θ_{12}, θ_{13}, θ_{23}, and a CP (charge parity) violating phase, δ. For Majorana neutrinos two additional phases, α_1 and α_2, have to be added because of an additional mass term whose phases cannot be absorbed due to the condition $\nu_l^c = \nu_l$ (see section 1.2.2). The matrix in equation 1.11 can be written as[2]:

$$U_{\mathrm{PMNS}} = \begin{pmatrix} c_{12}c_{13} & s_{12}c_{13} & s_{13}e^{-i\delta} \\ -s_{12}c_{23} - c_{12}s_{23}s_{13}e^{i\delta} & c_{12}c_{23} - s_{12}s_{23}s_{13}e^{i\delta} & s_{23}c_{13} \\ s_{12}s_{23} - c_{12}c_{23}s_{13}e^{i\delta} & -c_{12}s_{23} - s_{12}c_{23}s_{13}e^{i\delta} & c_{23}c_{13} \end{pmatrix} \times \begin{pmatrix} 1 & 0 & 0 \\ 0 & e^{i\alpha_1/2} & 0 \\ 0 & 0 & e^{i\alpha_2/2} \end{pmatrix} \tag{1.12}$$

We neglect now the second term of the matrix related to the Majorana neutrinos and we will come back to it in sections 1.2.2 and 1.3. From equation 1.10, it follows for the mass eigenstates:

$$|\nu_i\rangle = \sum_\alpha (U^\dagger)_{i\alpha} |\nu_\alpha\rangle = \sum_\alpha U^*_{\alpha i} |\nu_\alpha\rangle \tag{1.13}$$

whose time evolution can be described as plane waves[3]:

$$|\nu_i(x,t)\rangle = e^{-iE_it} |\nu_i(x,0)\rangle = e^{-iE_it} e^{ipx} |\nu_i\rangle \tag{1.14}$$

Assuming ultra-relativistic neutrinos, $p_i \gg m_i$ with p_i neutrino momentum and m_i its mass, emitted at $(x,\ t) = (0,0)$, we can use the approximation:

$$\sqrt{p_i^2 + m_i^2} \simeq p_i + \frac{m_i^2}{2p_i} \simeq E_i + \frac{m_i^2}{2E_i} \tag{1.15}$$

that allows to express the time evolution as function of the distance L covered by neutrinos:

$$|\nu_i(x,t)\rangle = e^{-im_i^2 \frac{L}{2E_i}} |\nu_i\rangle \ . \tag{1.16}$$

Thus the probability, after a distance L, to have neutrinos in the same flavour eigenstate is given by:

$$P(\alpha \to \alpha) = 1 - \sum_{\alpha \neq \beta} P(\alpha \to \beta) \tag{1.17}$$

---

[2] $c_{ij} = \cos(\theta_{ij})$ and $s_{ij} = \sin(\theta_{ij})$

[3] $\hbar = c = 1$

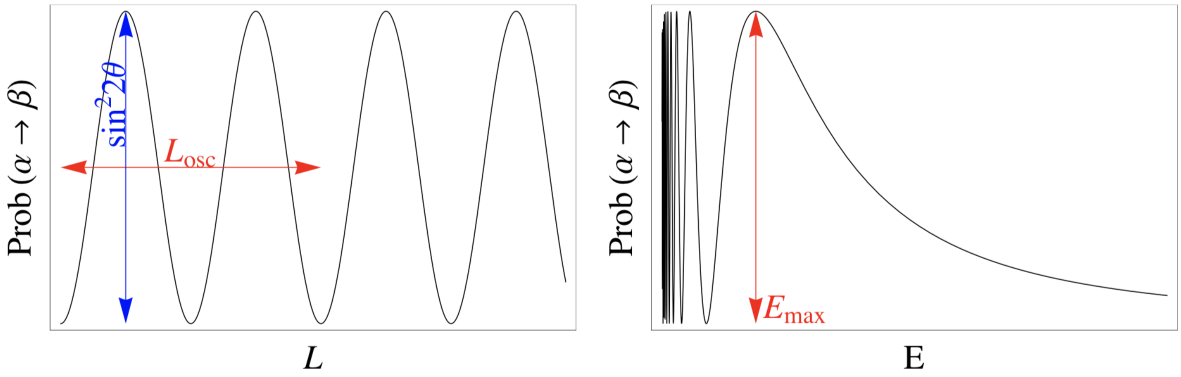

Figure 1.8: Left: two-family appearance oscillation probability as a function of the baseline distance L at fixed neutrino energy. Right: same probability shown as a function of the neutrino energy for fixed baseline. Figure and caption from [70].

where

$$\begin{aligned} P(\alpha \to \beta) = \delta_{\alpha\beta} - 4\,\mathrm{Re} \sum_{i>j=1}^{3} (U_{\alpha i} U^*_{\alpha j} U^*_{\beta j} U_{\beta j}) \sin^2\left(\Delta m^2_{ij} \frac{L}{4E}\right) \\ +2\,\mathrm{Im} \sum_{i>j=1}^{3} (U_{\alpha i} U^*_{\alpha j} U^*_{\beta j} U_{\beta j}) \sin^2\left(\Delta m^2_{ij} \frac{L}{4E}\right) \end{aligned} \tag{1.18}$$

with $\Delta m^2_{ij} = m^2_i - m^2_j$ and $L = ct$ distance between the source and the detector. From equation 1.18 it follows that the flavour oscillations are possible only if at least one of the mass eigenstates has a finite and not-zero mass value and if off-diagonal terms are present in the U matrix. The oscillatory behaviour is generated from the interference between two mass eigenstates and it depends on the phase of equation 1.18, that it is often rewritten as:

$$\phi_{ij} = 1.27 \Delta m^2_{ij} [eV^2] \frac{L\,[km]}{E\,[GeV]} \tag{1.19}$$

The sensitivity to neutrino oscillations depends on experimental variables. Because neutrino beams are not monoenergetic and detectors have a finite energy resolution, what is measured is an average oscillation probability. For $E/L \gg |\Delta m^2_{ij}|$ the phenomenon is negligible, while for $E/L \ll |\Delta m^2_{ij}|$ several oscillation cycles occur between the production and detection and the oscillating phase is averaged to $\langle \sin^2 \phi_{ij} \rangle = 1/2$. The appearance probability as function of the baseline distance L and the neutrino energy E is shown in figure 1.8. The oscillation experiments are sensitive only to the differences of the squared masses and not to their absolute values. The measurement of the neutrino mass, the determination of its nature and the study of the CP violation in the neutrino sector are the major goals of the current neutrino experiments.

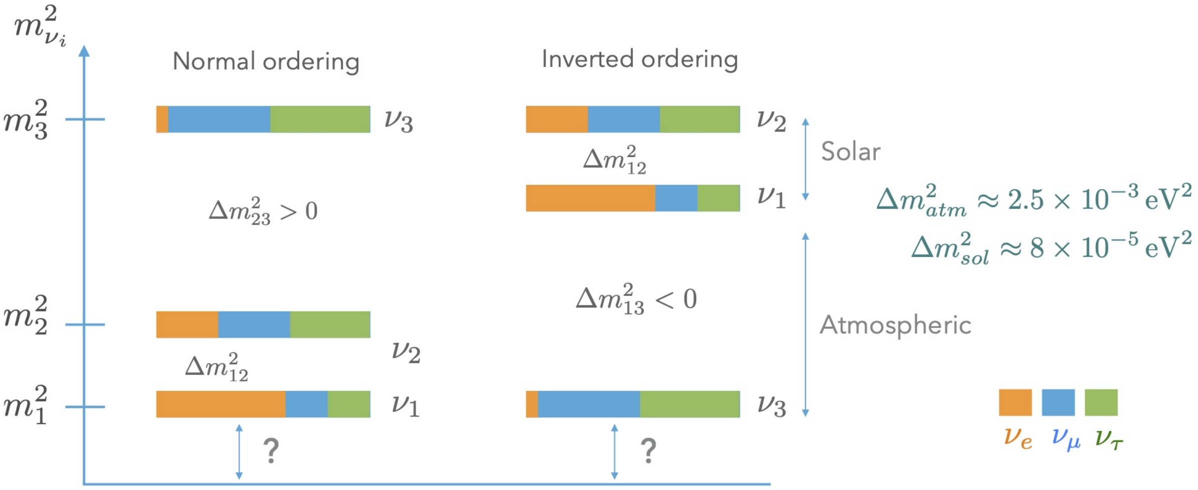

Figure 1.9: Normal ordering (left) and inverted ordering (right). Each horizontal bar is a neutrino mass eigenstate and the colours represent the flavour component in each of them. Credit: L. Baudis.

The data from oscillation experiments are in agreement with the three flavours model. In this framework there are two independent Δm^2_{ij}: Δm^2_{21} and Δm^2_{31}. The sign of Δm^2_{21} is positive and thus $m_1 < m_2$. However, it is not possible from the data to assign the sign of Δm^2_{31} and two mass ordering scenarios are possible.

- Normal Ordering (NO): $m_1 < m_2 \ll m_3$;
- Inverted Ordering (IO): $m_3 \ll m_1 < m_2$.

The degenerate case is for $|\Delta m^2_{ij}| \ll m_1 \approx m_2 \approx m_3$. A representation of the mass ordering scenarios is shown in figure 1.9. The values for θ_{12} and Δm^2_{21} are determined from experiments measuring solar neutrinos (ν_e) and antineutrinos from reactors ($\bar{\nu}_e$) while θ_{23} and Δm^2_{32} from atmospheric neutrinos (ν_μ e $\bar{\nu}_\mu$). An overview of the measured parameters from oscillation experiments is reported in table 1.1.

1.2.2 Dirac and Majorana Neutrinos

In the Standard Model (SM) neutrinos are described as left-handed leptons, ν_{lL} with $l = e, \mu, \tau$, without mass and charge and only weakly interacting. If we introduce right-handed neutrinos, ν_{lR}, the Higgs mechanism generates neutrino masses through the Yukawa coupling. The extended SM Lagrangian term for neutrinos can then be expressed as [72]:

$$\mathcal{L}^Y = -\sqrt{2} \sum_{l',l} \overline{L_{l'L}} Y_{l'l} \nu_{lR} \tilde{\Phi} + \text{h.c.} \tag{1.20}$$

Table 1.1: Neutrino oscillation parameters summary from frequentist global fit [71].

Parameter	**Best fit ± 1σ**	**2σ range**	**3σ range**
$\Delta m^2_{21}[10^{-5}\mathrm{eV}^2]$	$7.50^{+0.22}_{-0.20}$	7.11 – 7.93	6.94 - 8.14
$\lvert\Delta m^2_{31}\rvert[10^{-3}\mathrm{eV}^2]$ (NO)	$2.56^{+0.03}_{-0.04}$	2.49 – 2.62	2.46 - 2.65
$\lvert\Delta m^2_{31}\rvert[10^{-3}\mathrm{eV}^2]$ (IO)	2.46±0.03	2.40 – 2.52	2.37 - 2.55
$\sin^2\theta_{12}/10^{-1}$	3.18±0.16	2.86 – 3.52	2.71 - 3.70
$\sin^2\theta_{13}/10^{-2}$ (NO)	$2.225^{+0.055}_{-0.078}$	2.081 – 2.349	2.015 - 2.417
$\sin^2\theta_{13}/10^{-2}$ (IO)	$2.250^{+0.056}_{-0.076}$	2.107 – 2.373	2.039 - 2.441
$\sin^2\theta_{23}/10^{-1}$ (NO)	$5.66^{+0.16}_{-0.22}$	5.05 – 5.96	4.41 - 6.09
$\sin^2\theta_{23}/10^{-1}$ (IO)	$5.66^{+0.18}_{-0.23}$	5.14 – 5.97	4.46 - 6.09
δ/π (NO)	$1.20^{+0.23}_{-0.14}$	0.93 – 1.80	0.80 - 2.00
δ/π (IO)	1.54±0.13	1.27 – 1.79	1.14 - 1.90

where $Y_{l'l}$ are the dimensionless Yukawa coupling constants, $L_{l'L}$ is the lepton doublet and Φ the Higgs doublet:

$$L_{lL} = \begin{pmatrix} \nu_{lL} \\ l_L \end{pmatrix}, \; \Phi = \begin{pmatrix} \Phi^{(+)} \\ \Phi^{(-)} \end{pmatrix} \tag{1.21}$$

For the spontaneous breaking of the electroweak gauge symmetry $\mathrm{SU}_L(2)\times\mathrm{U}_Y(1)$:

$$\tilde{\Phi} = i\sigma_2\Phi^* = \frac{1}{\sqrt{2}}\begin{pmatrix} v+H \\ 0 \end{pmatrix} \tag{1.22}$$

where σ_2 is the second Pauli matrix, H the Higgs boson field and $v \simeq 246\,\mathrm{GeV}$ its vacuum expectation value. Substituting equations 1.21 and 1.22 into the 1.20 we can obtain the Dirac mass term:

$$\mathcal{L}^D = -\sum_{l',l} \overline{\nu_{l'L}} v Y_{l'l} \nu_{lR} + \mathrm{h.c.} \tag{1.23}$$

The Dirac neutrino masses are then obtained from the diagonalisation of the Y matrix and are:

$$m_i = v y_i \tag{1.24}$$

Considering negligible the mass of the lightest neutrino, the mass of the heaviest one is $\sim \sqrt{|\Delta m^2_{31}|} \simeq 5\times 10^{-2}\,\mathrm{eV}$ for both NO and IO; this gives a Yukawa coupling of $y \simeq 2\times 10^{-13}$. This value is at least ten orders of magnitude smaller compared to the Yukawa couplings of quarks and charged leptons. The neutrino masses are now included in the neutrino minimal standard model (νMSM), however the small value of the Yukawa couplings and the presence of the right-handed particles, non interacting in the SM, led to consider the Majorana formulation. It is possible to write the right-handed neutrinos as parametrisation of the left-handed ones. Using the charge conjugation matrix C which satisfy the conditions:

$$C\gamma_\alpha^T C^{-1} = -\gamma_\alpha \qquad \text{and} \qquad C^T = -C \tag{1.25}$$

with γ_α the Dirac matrices, α =(0,...,3), we can write the right-handed neutrinos as:

$$\nu_{lR} = C\overline{\nu_{lL}}^T = \nu_{lL}^c \tag{1.26}$$

The Majorana neutrino field and its charge conjugate are then:

$$\nu_l = \nu_{lL} + \nu_{lR} = \nu_{lL} + \nu_{lL}^c \tag{1.27}$$

$$\nu_l^c = (\nu_{lL} + \nu_{lL}^c)^c = \nu_{lL}^c + \nu_{lL} = \nu_l \tag{1.28}$$

The Majorana neutrino is its own antiparticle and has no electric charge or lepton number. The Majorana mass term can thus be written as:

$$\mathcal{L}^M = -\frac{1}{2}\sum_{l',l} \overline{\nu_{l'L}} M_{l'l}^L \nu_{lL}^c + \text{h.c.} \tag{1.29}$$

where M^L is a symmetric matrix and it can be diagonalised using the unitary neutrino mixing matrix U_{PMNS}. Equation 1.29 becomes:

$$\mathcal{L}^M = -\frac{1}{2}\sum_{i=1}^{3} m_i \bar{\nu}_i \nu_i \tag{1.30}$$

where $\nu_i = \nu_i^c$ is the field of the Majorana neutrino with mass m_i. This term is forbidden by the symmetries of the SM as it violates the total lepton number conservation. In order to generate the Majorana mass term, we can introduce a non-renormalisable[4] term, beyond the SM, which is suppressed at low energy. This is done by introducing an effective Lagrangian:

$$\mathcal{L}^{\text{eff}} = -\frac{1}{\Lambda}\sum_{l',l} \overline{L_{l'L}} \tilde{\Phi} \overline{Y}_{l'L} \tilde{\Phi}^T L_{lL}^c + \text{h.c.} \tag{1.31}$$

---

[4] The renormalisability in the SM requires that the terms in the Lagrangian have dimension 4. The non-renormalisable term should thus have a higher dimension [72].

where $\Lambda \gg v$ is a parameter, with dimension of a mass, that indicates the high energy scale at which the total lepton number is violated. Similarly to the previous procedure, after spontaneous symmetry breaking, we obtain the neutrino masses from diagonalisation:

$$m_i = \frac{v^2}{\Lambda}\bar{y}_i \tag{1.32}$$

The parameter Λ acts as a suppression factor of the electroweak scale v. This suppression is called *seesaw mechanism*. Assuming $m_i \sim 5 \times 10^{-2}\,\mathrm{eV}$ and $\bar{y}_i \sim 1$, we find $\Lambda \sim 10^{15}\,\mathrm{GeV}$. Thus the small value of the neutrino masses could be explained by a violation of the total lepton number at a very large scale [72].

1.3 Neutrinoless Double Beta Decay

The double beta decay (DBD) is a rare spontaneous transition in which two neutrons in the nucleus are converted to protons, and two electrons are emitted. This decay occurs with the emission of two antineutrinos ($2\nu\beta\beta$). Following the Majorana formulation, another similar process is predicted, the DBD without neutrino emission (*neutrinoless*, $0\nu\beta\beta$). While the former is predicted by the SM and it has been measured in 11 different isotopes[5], the latter has not been observed yet [73]. The processes can be described as:

$$2\nu\beta\beta : (A, Z) \to (A, Z+2) + 2e^- + 2\bar{\nu}_e \tag{1.33}$$

$$0\nu\beta\beta : (A, Z) \to (A, Z+2) + 2e^- \tag{1.34}$$

where A is the atomic mass and Z is the atomic number of the nucleus. The Feynman diagrams of the two DBD processes are shown in figure 1.10 on the left. The $0\nu\beta\beta$ transition violates the lepton number conservation by 2 units and its discovery would prove that this is not a symmetry of nature. The signature of the decay modes described is given by the sum of the electrons energies and they are distinctive. The two-neutrino mode has a continuum spectrum with a maximum at ~1/3 of the end-point or Q-value ($Q_{\beta\beta}$) because most of the energy is carried by the neutrinos. In the $0\nu\beta\beta$ instead the electrons carry the whole energy and the spectrum is a monoenergetic peak at $Q_{\beta\beta}$, broadened by the experimental energy resolution. The spectra are shown in figure 1.10 on the right.

The DBD is possible if the nucleus (A, Z) has a lower mass and higher binding energy than the $(A, Z{+}1)$ one and higher mass and lower binding energy than the $(A, Z{+}2)$. Therefore the process is allowed for several even-even nuclei with spin zero, while it is

---

[5] Additionally, the double-electron capture process has been measured in 3 other isotopes.

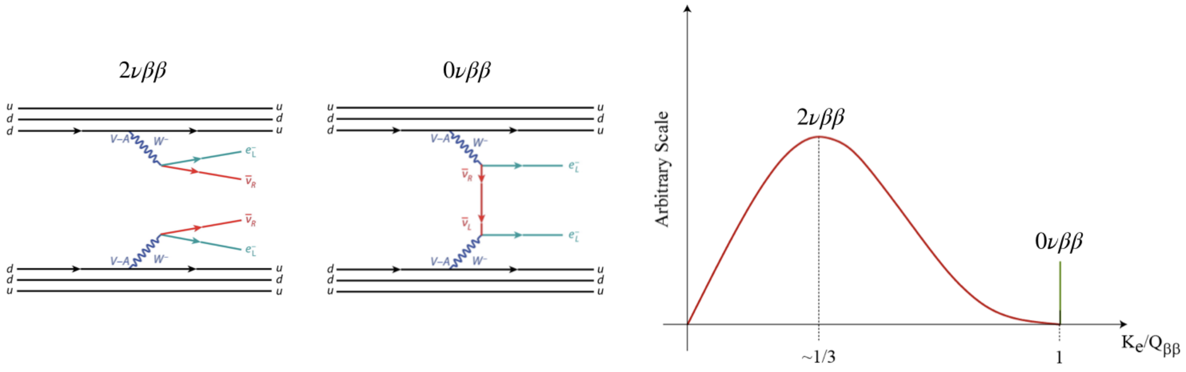

Figure 1.10: Left: Feynman diagrams for the DBD processes. Figure adapted from [74]. Right: signature for the $2\nu\beta\beta$ (red) and $0\nu\beta\beta$ (green) in the sum of the electrons energies space. The spectra are not on scale, the $0\nu\beta\beta$ peak is plotted much larger for visualisation.

suppressed for odd-odd nuclei [75]. A parametrisation of the nuclear binding energy in the ground state is provided by a semi-empirical expression based on the *liquid drop nuclear model*[6] [74, 76]:

$$B(Z,A) = a_{\mathrm{v}}A - a_{\mathrm{s}}A^{\frac{2}{3}} - a_{\mathrm{c}}\frac{Z^2}{A^{\frac{1}{3}}} - a_{\mathrm{a}}\frac{(N-Z)^2}{A} + \delta(Z,A) \tag{1.35}$$

$$\text{where} \quad \delta(Z,A) = \begin{cases} +a_{\mathrm{p}}A^{-1/2} & \text{MeV} \quad A \text{ even} \quad Z,N \text{ even} \\ 0 & \text{MeV} \quad A \text{ odd} \\ -a_{\mathrm{p}}A^{-1/2} & \text{MeV} \quad A \text{ even} \quad Z,N \text{ odd} \end{cases}$$

$\delta(Z,A)$ is the *pairing energy* term and the parameters a_i $(i = v, s, c, a, p)$ are the volume, surface, Coulomb repulsion, asymmetry and pairing coefficients, respectively, and they are determined empirically. In figure 1.11 the nuclear mass behaviour, for a given mass number, is shown.

The rate of the DBD decay modes can be computed starting from the Fermi rules for the single β decay. The transition probability $\Gamma^{2\nu}$ for the two-neutrino mode can be expressed as:

$$\Gamma^{2\nu} = \frac{1}{T^{2\nu}_{1/2}} = G^{2\nu}(Q_{\beta\beta}, Z)|M^{2\nu}|^2 \tag{1.36}$$

where $G^{2\nu} \propto Q^{11}_{\beta\beta}$ is the phase space integrated on the energies and angles of the leptons in the final state and it is calculated exactly. $M^{2\nu}$ is the nuclear matrix element (NME) associated with the structure of the transition and $T^{2\nu}_{1/2}$ is the half-life of the decay. Similarly,

---

[6] The nucleus is treated like a drop of incompressible fluid made of nucleons and affected by the strong nuclear force.

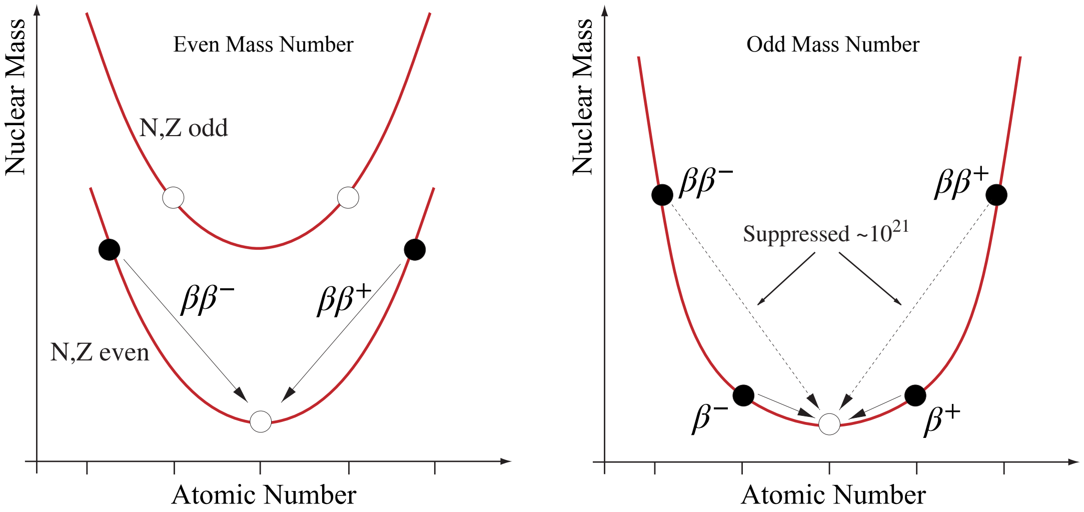

Figure 1.11: Nuclear mass as a function of the atomic number Z in the case of an isobar candidate with A even (left) and A odd (right). Figure and caption adapted from [75].

for the neutrinoless mode:

$$\Gamma^{0\nu} = \frac{1}{T^{0\nu}_{1/2}} = G^{0\nu}(Q_{\beta\beta}, Z)|M^{0\nu}|^2 \frac{|\langle m_{ee}\rangle|^2}{m_e^2} \tag{1.37}$$

where m_e is the electron mass and all the other parameters are similar to the ones of the $2\nu\beta\beta$ but relative to the $0\nu\beta\beta$ with $G^{0\nu} \propto Q^5_{\beta\beta}$. A more detailed discussion on the phase space factors is given in [77]. The parameter $\langle m_{ee}\rangle$ is the *effective Majorana mass*. Starting from equation 1.29 it is possible to diagonalise the matrix M_{ee} and we can define:

$$\langle m_{ee}\rangle \equiv \left|\sum_{i=1}^{3} U^2_{ei} m_i\right| \tag{1.38}$$

where the index i runs on the neutrino masses and U is the PMNS mixing matrix with the Majorana term that includes the two additional phases α_1 and α_2, as shown in equation 1.12. Thus the measurement of the $0\nu\beta\beta$ decay can be directly linked to the constraints of the Majorana phases and the absolute scale of the neutrino masses. The $\langle m_{ee}\rangle$ is derived experimentally from the decay half-life measurement and it is inferred using the phase space and NME factors. The calculation of the NME is the main source of uncertainty. One of the main difficulties in calculating the NME arises from the consideration, beside the ground state, of all the possible transitions with the many excited states. Several theoretical model have been used to this extent, the most relevant are *Interacting Shell Model* (ISM) [78], *Quasiparticle Random Phase Approximation* (QRPA) [79], *Interacting Boson Model* (IBM-2) [80] and *Energy Density Functional Method* (EDF) [81]. A review

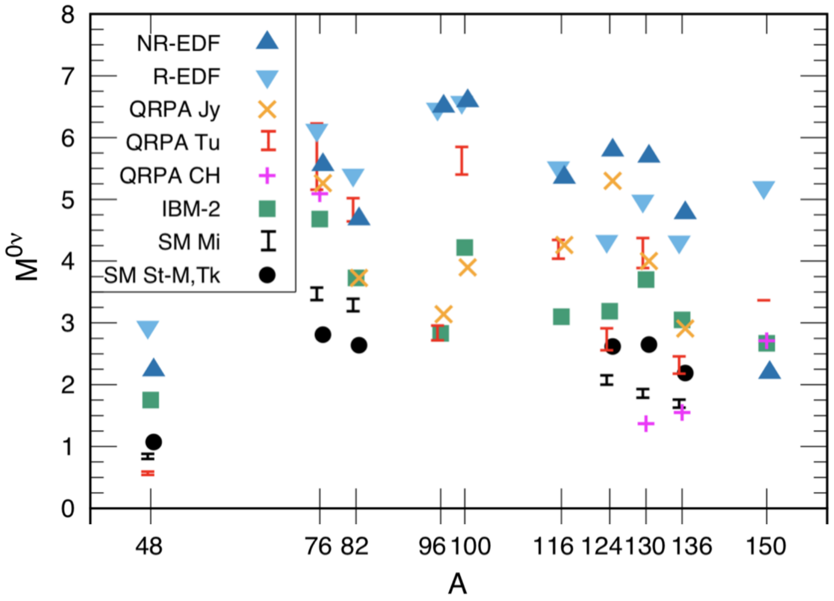

Figure 1.12: Nuclear matrix elements for some of the $0\nu\beta\beta$ decay candidates as function of mass number. For more details on the models and their uncertainties refer to [82], from which the figure is taken.

of these methods can be found in [82]. The values obtained for the $0\nu\beta\beta$ decay from the different methods are shown in figure 1.12 for the DBD candidates most used in the experiments. While the uncertainties on the single models are on the order of 20%, the discrepancies among them are even larger.

Several isotopes fulfil the requirements to undergo a DBD decay. However the ones with a higher Q-value are preferred from an experimental point of view due to the higher transition probability (as mentioned $\Gamma^{0\nu} \propto G^{0\nu} \propto Q^5_{\beta\beta}$) and a lower electromagnetic natural radioactivity that lies below the ^{208}Tl peak from the ^{232}Th chain, at 2615 keV. The γ and β decays from the natural decay chains are a source of background for the experiments searching for DBD. Another critical property affecting the choice of the best candidate is the natural abundance of the decaying isotope. In table 1.2 the DBD candidates with a Q-value above 2 MeV are reported. The natural abundance and the phase space factors for $2\nu\beta\beta$ and $0\nu\beta\beta$ decays are also reported. The experimental requirements and results are discussed in more detail in section 1.4.

Table 1.2: Double beta decay candidates with Q-value above 2 MeV. Transitions and natural abundances (Nat. Ab.) of the decays are from [83]. The $Q_{\beta\beta}$ and the phase space factors, relative to the ground state, for $2\nu\beta\beta$ and $0\nu\beta\beta$ decays are extracted from [77].

Transition	$Q_{\beta\beta}$ [keV]	Nat. Ab. [%]	$G^{2\nu}$ [10^{-19}yr^{-1}]	$G^{0\nu}$ [10^{-15}yr^{-1}]
^{48}Ca → ^{48}Ti	4274.26(4.04)	0.187	155.5	24.81
^{76}Ge → ^{76}Se	2039.061(7)	7.8	0.4817	2.363
^{82}Se → ^{82}Kr	2995.12(2.01)	9.2	15.96	10.16
^{96}Zr → ^{96}Mo	3350.37(2.89)	2.8	68.16	20.58
^{100}Mo → ^{100}Ru	3034.40(17)	9.6	33.08	15.92
^{110}Pd → ^{110}Cd	2017.85(64)	11.8	1.377	4.815
^{116}Cd → ^{116}Sn	2813.50(13)	7.5	27.64	16.70
^{124}Sn → ^{124}Te	2286.97(1.53)	5.64	5.530	9.040
^{130}Te → ^{130}Xe	2526.97(23)	34.5	15.29	14.22
^{136}Xe → ^{136}Ba	2457.83(37)	8.9	14.33	14.58
^{150}Nd → ^{150}Sm	3371.38(20)	5.6	364.30	63.03

1.4 $0\nu\beta\beta$ Experimental Overview

The first effort to measure the half-life of a double beta decay was performed by Fireman in 1948 using the ^{124}Sn isotope [84]. The process was measured for the first time by Inghram and Reynolds in 1950 in a series of geochemical experiments using ^{130}Te [85]. These experiments were based on measurements on the daughter nuclei of the decay and were not able to distinguish between two-neutrino or neutrinoless DBD. Since 1950 many experiments have been conducted using different techniques and candidates. High-resolution germanium diode gamma-ray spectrometers as both source and detector for a double-beta decay experiment were introduced in 1967 [86]. The first direct observation of the $2\nu\beta\beta$ decay was achieved in 1987 in ^{82}Se [87]. Modern experiments are based on the direct measurement of the electrons emitted in the process. Two main approaches can be distinguished:

i. Passive source: the source and the detector are separated. This method allows for tracking and thus a good external background reduction and event reconstruction. Nevertheless, because of the low energy resolution (∼10% FWHM) the $2\nu\beta\beta$ decay constitutes a severe background for the $0\nu\beta\beta$ search. Moreover the efficiency is low (∼30%) and it is difficult to achieve large masses.

ii. Active source: the detector is made of a material acting also as source. This technique provides high efficiency (≥90%) and energy resolution (∼0.1% FWHM) and large masses can be easily achieved. However it is not possible to reconstruct the event topology and they require a dedicated cleaning campaign of the materials used.

In order to compare the performances of different experiments, it is common to use a figure of merit for the sensitivity to the $0\nu\beta\beta$ decay, indicated as $S^{0\nu}$. It is defined as the process half-life and corresponds to the maximum number of signal events that could be hidden by background fluctuations at a certain confidence level (CL). At 1σ level it is defined as [88]:

$$S^{0\nu} \equiv \ln(2)\varepsilon\frac{N_{\beta\beta}}{n_{\mathrm{bkg}}}t \tag{1.39}$$

where ε is the detection efficiency, $N_{\beta\beta}$ is the number of candidate nuclei that can undergo the transition, n_{bkg} is the maximum number of counts that could be hidden by a background fluctuation and t is the live-time of the measurement. For a given isotope, $N_{\beta\beta}$ can further be expanded as:

$$N_{\beta\beta} = \alpha\frac{N_{\mathrm{A}}M}{A} \tag{1.40}$$

where α the isotopic abundance (natural or enriched), N_{A} is Avogadro's number, M is the source mass and A is the atomic mass number of the decaying isotope. The background in the region of interest (ROI) around the $Q_{\beta\beta}$ scales with the mass and the definition of the ROI itself depends on the energy resolution of the detector. Assuming that the number of background counts, N_{bkg}, follows Poisson statistics, n_{bkg} can be written as:

$$n_{\mathrm{bkg}} = \sqrt{N_{\mathrm{bkg}}} = \sqrt{\Delta E b M t} \tag{1.41}$$

where ΔE is the ROI, conventionally defined as the full-width-at-half-maximum (FWHM) and b is the background rate per unit mass, time and energy. Combining equations 1.40 and 1.41 into 1.39, we obtain:

$$S^{0\nu} = \ln(2)\varepsilon\frac{\alpha N_{\mathrm{A}}}{A}\sqrt{\frac{M\cdot t}{\Delta E\cdot b}} \tag{1.42}$$

If the background rate in the ROI for a given exposure $(M \cdot t)$ is compatible with zero and thus the experiment is in a so called zero-background regime, the assumption of Poisson distribution is not valid and n_{bkg} is defined as a constant n_0 indicating the maximum number of counts compatible with the observed background. The figure of merit in this case becomes:

$$S^{0\nu}_{0\mathrm{bkg}} = \ln(2)\varepsilon\frac{\alpha N_{\mathrm{A}}}{A}\frac{M\cdot t}{n_0} \tag{1.43}$$

In view of the dependencies of the sensitivity showed in equations 1.42 and 1.43, the experimental requirements needed to perform a $0\nu\beta\beta$ search can be summarised as follow:

- High isotopic abundance or possibility to enrich the source with the decaying candidate;
- High detector performance in terms of efficiency and energy resolution;
- High detector mass and long live-time measurement to maximise the exposure;
- Low background rate in the ROI, involving proper selection and cleaning of the materials, as well as good background discrimination techniques.

To date the $0\nu\beta\beta$ decay has never been observed. The experiments place constraints, or lower limits, on its half-life and thus on the effective Majorana mass $\langle m_{ee} \rangle$, as evident from equation 1.37. The current most sensitive experiments exploit different techniques and various isotopes. GERDA and MAJORANA use solid state germanium diodes enriched in ^{76}Ge. GERDA [89] is the first experiment in this field to reach a "background-free" level in the ROI and the MAJORANA demonstrator [90] achieved an excellent energy resolution of 2.53 keV FWHM at the Q-value. These collaborations merged into a common one, LEGEND [91], to push even further the search for the neutrinoless double beta decay with ^{76}Ge in order to reach a sensitivity of $\sim 10^{27}$ yr and $\sim 10^{28}$ yr with LEGEND-200 and LEGEND-1000, respectively. Cryogenic bolometers are being exploited by the CUORE [92] experiment, still in a data-taking phase, to search for the decay in ^{130}Te. Several R&D activities have shown the possibility to use this technique with scintillating crystals to allow for particle identification and further background reduction. This was successfully tested in a few demonstrators using also different isotopes as ^{100}Mo, ^{82}Se and ^{116}Cd. The next generation of this type, CUPID [93], will indeed use Li_2MoO_4 crystals enriched to 95% in ^{100}Mo. Liquid and gaseous ^{136}Xe is used by several experiments in single phase or high pressure TPCs, such as EXO-200 [94] and NEXT-White [95]. Future experiments improving these technologies are already foreseen with nEXO [96] and NEXT-100 [97]. The current lower limit on the half-life of the ^{136}Xe is set by KamLAND-Zen, $T^{0\nu}_{1/2} > 1.07 \times 10^{26}$ years at 90% CL [98], a large scale Xe-loaded liquid scintillator. The experiment is now running with an increased mass of 745 kg of xenon, aiming to reach a sensitivity $> 4.6 \times 10^{26}$ years.

A summary of the present experiments with the most recent results and the projected sensitivity for the future experiments is reported in table 1.3. To compare the results of the experiments exploiting different isotopes we can convert the half-life into the effective Majorana mass using the corresponding phase space factors and NME. This is shown in

Table 1.3: Some of the leading present, planned and future experiments for $0\nu\beta\beta$ search. Where not indicated specifically in the Ref. column, the values are from [99]. (*) Super-NEMO will use an external source and therefore it can study different isotopes.

Experiment	**Isotope**	$\mathbf{T^{0\nu}_{1/2}}$ **[yr]**	$\langle \mathbf{m_{ee}} \rangle$ **[meV]**	**Ref.**
Present		*limit at 90% CL*		
GERDA	^{76}Ge	9×10^{25}	104 - 228	[89]
MAJORANA	^{76}Ge	2.7×10^{25}	200 - 433	[90]
CUORE	^{130}Te	3.2×10^{25}	75 - 350	[92]
EXO-200	^{136}Xe	3.5×10^{25}	93 - 286	[94]
KamLAND-Zen	^{136}Xe	10.7×10^{25}	61 - 165	[98]
Planned		*3σ discovery sensitivity*		
LEGEND-200	^{76}Ge	9.4×10^{26}	35 - 73	
NEXT-100	^{136}Xe	7.0×10^{25}	65 - 281	
Super-NEMO	^{82}Se (*)	-	$\geq$50	
Future		*3σ discovery sensitivity*		
LEGEND-1000	^{76}Ge	1.2×10^{28}	10 - 20	
CUPID	^{100}Mo	1.1×10^{27}	12 - 20	[93]
AMoRE	^{100}Mo	-	20 - 50	
nEXO	^{136}Xe	5.7×10^{27}	7.3 - 22.3	[96]
NEXT-HD	^{136}Xe	1.7×10^{27}	13 - 57	

figure 1.13 as a function of the lightest neutrino mass, together with the allowed parameter space for the neutrino mass orderings. So far, the probed effective Majorana mass allowed to exclude part of the degenerate ordering, but it is not included in the parameter space predicted by the IO or the NO. The next generation of experiments will be able to probe the $\langle m_{ee} \rangle$ predicted in the entire parameter space of the IO, down to 10 meV.

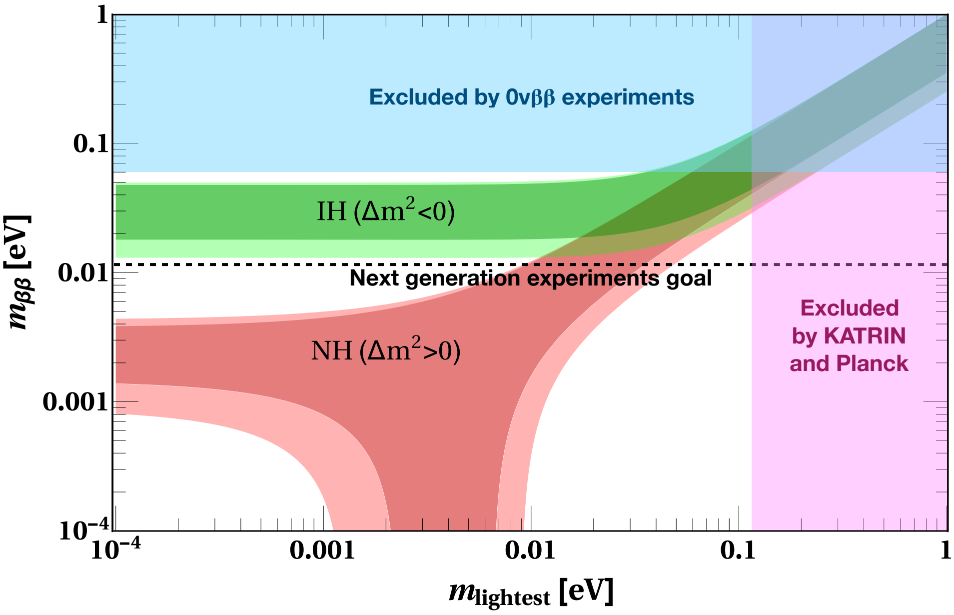

Figure 1.13: Effective Majorana mass $|m_{\beta\beta}| \equiv |m_{ee}|$ as function of the lightest neutrino m_{lightest}. The shaded areas correspond to the 3σ region due to error propagation of the oscillation parameters uncertainties. The parameter space excluded by the $0\nu\beta\beta$ experiments is reported in light blue on the top of the figure. The masses excluded by cosmology (Planck) and direct mass measurement (KATRIN) are also shown in pink. Figure modified from [75].

1.5 Simultaneous Search for Dark Matter and $0\nu\beta\beta$

In this chapter two of the main puzzles of modern astroparticle physics have been highlighted. Several experiments in the past and present years pushed the technology and the research state-of-art to investigate either the composition of DM or neutrino nature. Future experiments will foresee even more challenges to improve their sensitivity or discovery potential. The continuously increasing detector masses are also limited by the availability of required materials or isotopes. The direct DM detection and the $0\nu\beta\beta$ search present multiple characteristics that allow the experiments looking for these phenomena to push in the same direction. They indeed belong to the class of experiments that look for rare events and thus their primary goal is to reduce the background that can hide or mimic a signal. This is achieved by placing the detectors underground, shielded from cosmic rays by kilometres of rock. Screening, selection and cleaning of the materials are also employed, even though focusing on different energy regions. They both benefit from scalable and stable technologies that would allow to increase the exposure and from detector developments aiming to higher efficiencies and accuracy. One challenge is due to the isotopic abundance. Enriching in $0\nu\beta\beta$ candidate isotope results in a higher $2\nu\beta\beta$ background that is often dominant in regions of interest for the DM search. Although different technologies such as dual-phase TPCs allow to discriminate signal and background based on particle identification, and thus also distinguish a $\beta\beta$ interaction from a WIMP, this is not always possible for other DM models such as Axion Like Particles (ALPs). Therefore the choice for enrichment needs to be considered based on the natural abundance, the overall absolute mass of the candidate isotope and the effects on the other physics channels. The main challenges to prove the viability of a detector able to simultaneously search for DM and $0\nu\beta\beta$ can be summarised into:

- A large cleaning and material screening and selection effort to reduce the backgrounds affecting the interesting signals;
- Choose an isotope to maximise the sensitivity to both types of interactions;
- Develop a read-out system and/or software techniques that allow for a high efficiency and resolution in a wide energy region;
- Optimise the level of enrichment needed to perform competitive measurements in both searches.

Most of these points can be easily overcome. Planning ahead of time and considering a more intense cleaning campaign or selecting more carefully the materials would reduce the background sufficiently in both ROI with a limited increase of costs. Regarding the candidates, the ^{136}Xe isotope is already extensively used for $0\nu\beta\beta$ searches by some of the currently most sensitive experiments and the xenon is used also by the leading experiments in the WIMP-DM sector. The main experimental challenge that will be studied in this thesis is the possibility of having a high detector performance simultaneously for both searches. In particular, this effort is based on the XENON1T data [51]. In this case the detector, the software and the analysis framework were developed for the few keV energy region relevant for WIMP interaction and this work aims to extend the excellent performance of the dual-phase TPCs to the MeV region, due to the $Q_{\beta\beta}$ of the ^{136}Xe isotope. Despite the fact that the materials of the XENON1T experiment, and the currently under commissioning XENONnT upgrade, were not selected to search for the $0\nu\beta\beta$ decay, proving the possibility of a simultaneous search would open the path for future experiments toward this opportunity. The results achieved are indeed taken into account by the DARWIN collaboration, which included the $0\nu\beta\beta$ decay search among the mail channels of its physics goals [100].

CHAPTER 2

The XENON Dark Matter Project

Liquid xenon is used for direct dark matter searches, looking for interaction of hypothetical WIMPs with atomic nuclei. The XENON experiments use dual-phase xenon TPCs located at the Laboratori Nazionali del Gran Sasso (LNGS) at ∼3600 m.w.e[1], in order to search for WIMP scatters off xenon nuclei [101].

The first detector was XENON10 [102], installed in 2005 and operational until 2007, featuring a total LXe mass of 15 kg, with 5.4 kg used as fiducial mass. The experiment was successful in proving the dual-phase xenon time projection chamber technology and, using 58.6 days of science data, established the world-record upper limits on both spin-independent and spin-dependent WIMP-nucleon cross section (couplings to neutrons), with a minimum of $4.5\times10^{-44}\,\mathrm{cm}^2$ [103] and $5\times10^{-39}\,\mathrm{cm}^2$ [104], respectively, for 30 GeV/c^2 WIMP mass at 90 % CL. The next phase, XENON100 [105], exploited 161 kg of LXe, with 62 kg used as active volume in the TPC. The fiducial volume chosen for the analyses was 34 kg or 48 kg, according to the background level in the runs. Thanks to the higher mass and a factor 100 background reduction, XENON100 reached an upper limit on the WIMP SI cross section of $1.1\times10^{-45}\,\mathrm{cm}^2$ for 50 GeV/c^2 mass at 90 % CL, using 447 live-days. The experiment also established new upper limits for the spin-dependent interaction, with minima at $2.0\times10^{-40}\,\mathrm{cm}^2$ and $5.2\times10^{-39}\,\mathrm{cm}^2$ for 50 GeV/c^2 mass at 90 % CL, for couplings to neutrons and protons, respectively [106]. To further increase the sensitivity to the WIMP dark matter search, the collaboration deployed multi-tonne detectors, XENON1T first and currently XENONnT. These will be described in detail in this chapter and they are the experiments on which the work of this thesis is based.

This chapter describes, in section 2.1, the characteristics that make xenon one of the best choices as a detection medium and the signal production process in an interaction. The working principle of dual-phase TPCs is also introduced. The design of the XENON1T

---

[1] *meter water equivalent*: unit used to indicate a place or object is shielded from cosmic rays as if it would be placed below a certain amount of water.

detector and its main WIMP searches results are shown in section 2.2. The XENONnT experiment and its physics reach are presented in section 2.3.

2.1 Liquid Xenon as Detection Medium

The good scintillation and ionisation properties, together with its high atomic mass, made liquid xenon a largely used detection medium for high energy and astroparticle physics experiments. Among noble gasses, xenon has several properties that make it one of the best atoms to look for WIMP-nucleon interactions. It has one of the highest atomic masses (A∼131) that enhances the spin independent cross section, proportional to A^2 as pointed out in section 1.1.3, relevant especially in the few keV nuclear recoil region. It contains different isotopes, including the odd spin components ^{129}Xe and ^{131}Xe, that allow to search for spin-dependent dark matter interaction. The isotope components of natural xenon are reported in table 2.1. Furthermore it has a high stopping power that makes the active volume self-shielding. This property can be exploited for background reduction by fiducialisation, where a low-radioactive central detector region can be defined. A high liquid density of $\sim$2.9 g/cm^3, in combination with a boiling point of 178 K at a pressure of 2 bar allows for building compact detectors with large target masses and comparably simple cryogenic systems.

An interaction in liquid xenon produces a number of total quanta that depends on the incident energy. The transferred energy produces excitation, ionisation (Xe^+) and heat. Colliding with other xenon atoms the excitons (Xe^*) create excited molecular states called excimers (Xe_2^*). The excimers decay after 4.3 ns or 22.0 ns, corresponding to the singlet or triplet states, to the ground state by emitting a photon peaked at a wavelength of 178 nm.

Table 2.1: Isotope components of natural xenon. The odd spin components ^{129}Xe and ^{131}Xe allow to search for spin-dependent dark matter interaction. Values are from [107].

Isotope	Atomic Mass	Abundance [%]	Nuclear Spin
^{124}Xe	123.9	0.09	0
^{126}Xe	125.9	0.09	0
^{128}Xe	127.9	1.92	0
^{129}Xe	128.9	26.4	1/2
^{130}Xe	129.9	4.08	0
^{131}Xe	130.9	21.2	3/2
^{132}Xe	131.9	26.9	0
^{134}Xe	133.9	10.4	0
^{136}Xe	135.9	8.87	0

The process is shown as:

$$\mathrm{Xe}^* + \mathrm{Xe} \rightarrow \mathrm{Xe}_2^* \tag{2.1}$$

$$\mathrm{Xe}_2^* \rightarrow 2\mathrm{Xe} + h\nu \tag{2.2}$$

The electron-ion pairs from the ionisation process can recombine, producing also excitation states. The recombination decreases if an electric field that drifts the electrons away from the interaction site is applied. Also in the case of recombination an excimer is produced and thus a photon is emitted. The process is the following:

$$\mathrm{Xe}^+ + \mathrm{Xe} \rightarrow \mathrm{Xe}_2^+ \tag{2.3}$$

$$\mathrm{Xe}_2^+ + \mathrm{e}^- \rightarrow \mathrm{Xe}^{**} + \mathrm{Xe} \tag{2.4}$$

$$\mathrm{Xe}^{**} \rightarrow \mathrm{Xe}^* + \mathrm{heat} \tag{2.5}$$

$$\mathrm{Xe}^* + \mathrm{Xe} \rightarrow \mathrm{Xe}_2^* \tag{2.6}$$

$$\mathrm{Xe}_2^* \rightarrow 2\mathrm{Xe} + h\nu \tag{2.7}$$

The total number of scintillation photons, N_{ph}, produced by an interaction is then:

$$N_{ph} = a \cdot N_{ex} + b \cdot r \cdot N_i \tag{2.8}$$

where N_{ex} is the number of direct excitons, N_i is the number of ions, r is the fraction of ions that recombine and a,b are the respective efficiencies to produce photons [108]. The number of electrons produced would then be:

$$N_e = b \cdot (1 - r) \cdot N_i \tag{2.9}$$

The recombination factor r depends on the electric field applied. The energy released in the interaction can be written as in equation 2.10.

$$E = W \cdot (N_{ph} + N_e) \tag{2.10}$$

where W=(13.7±0.2) eV/quantum [108] is the average energy needed to generate either a photon or a free electron. The scintillation photons and ionisation electrons are then detected as S1 and S2 signals, with a photon detection efficiency of g_1 and charge amplification factor of g_2. The energy transferred in an interaction can thus be expressed as:

$$E = W \cdot \left(\frac{\mathrm{S1}}{g_1} + \frac{\mathrm{S2}}{g_2} \right) \tag{2.11}$$

g_1 and g_2 are detector-dependent parameters that can be determined using mono-energetic peaks [109]. Details on how to reconstruct the electronic recoil energy will be presented in section 3.3.

Dual-Phase Xenon Time Projection Chambers: Dual-phase TPCs exploit both the scintillation light and ionised electrons produced in the interaction of a particle with the atoms of a detection medium. Typically the TPC is filled with a noble gas in liquid phase up to almost the top, with a gas phase above it. When a particle interacts the prompt scintillation signal (S1) is detected by two arrays of photosensors, one on the top and one at the bottom of the TPC. The charge signal is detected by drifting the free electrons toward the liquid-gas interface under an applied field. Here they are extracted into the gas phase by another field that accelerates the electrons through the gas where they produce an electro-luminescence signal (S2) also detected by the photosensor arrays. The electric fields are produced by electrodes installed inside the TPC. The working principle is shown in figure 2.1.

Different photosensors can be used to detect the light and charge signals, like photomultiplier tubes (PMTs) or Silicon Photomultipliers (SiPMs). The main advantage in such a type of detector is the three-dimensional position reconstruction, given by the hit pattern on the light sensor arrays and by the delay time between light and charge signals. Additionally, it allows for electronic (ER) and nuclear recoil (NR) interaction identification thanks to the different ionisation process, and thus a different ratio of the detected signals.

$$\left(\frac{S2}{S1} \right)_{\mathrm{ER}} > \left(\frac{S2}{S1} \right)_{\mathrm{NR}} \tag{2.12}$$

This property can be used to further reduce the background.

More detailed descriptions of the XENON1T and XENONnT TPCs are provided in sections 2.2.1 and 2.3.2, respectively. The work done, at the beginning of my Ph.D. studies, to characterise a small dual-phase TPC at the University of Zurich and study the liquid xenon properties is briefly described in appendix A.

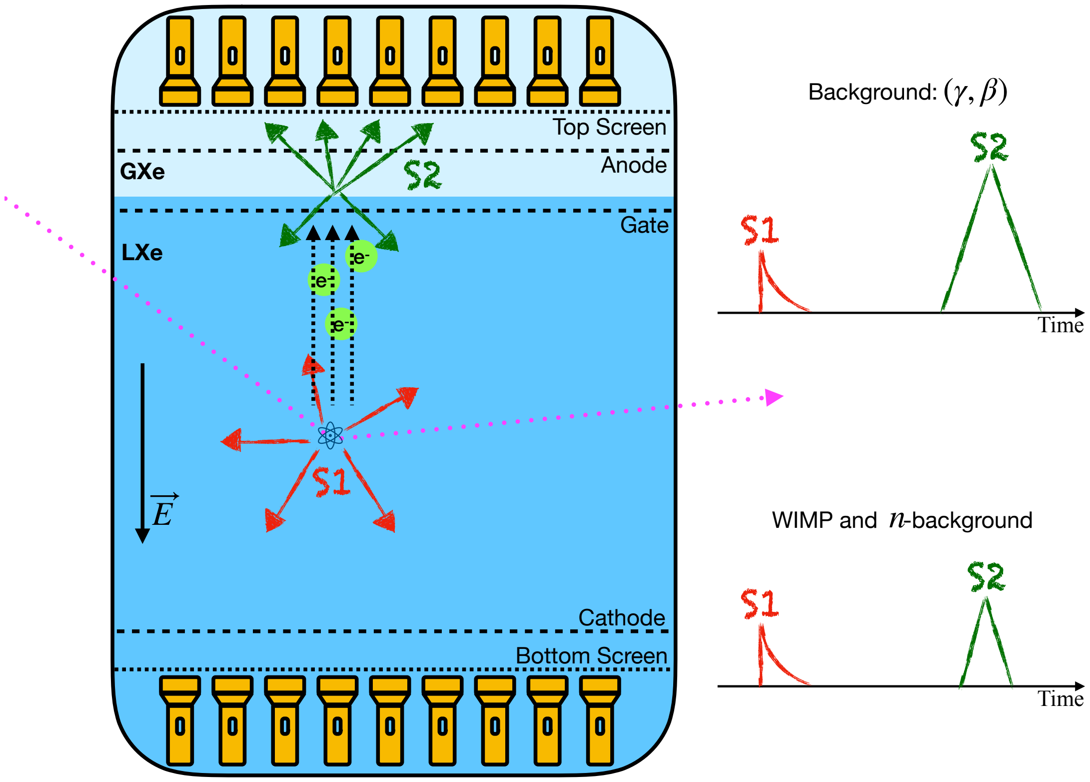

Figure 2.1: Working principle of a dual-phase TPC: the prompt scintillation light (S1) generated in the LXe is recorded by PMTs installed above and below the target. The delayed secondary-light signal S2 is created by proportional scintillation induced by ionisation electrons (e^-) in the gas phase and it is also measured by the PMTs. Five electrodes are used to establish the required electric fields. The S2 pattern observed by the top PMTs and the time difference between S1 and S2 are used for a 3-dimensional position reconstruction. The charge to light ratio (S2/S1) allows for the identification of the interaction type.

2.2 The XENON1T Experiment

The XENON1T detector is located underground, in the Hall B of LNGS. The TPC is installed inside a double-walled vacuum cryostat in the centre of a 10.2 m high and 9.6 m wide water tank, containing about 700 t of deionised water, and equipped with 84 Hamamatsu R5912ASSY 8” PMTs, that serves as passive shield as well as Cherenkov muon veto detector [110]. Several systems ensure the functionality of the experiment, such as the cryogenics, purification and gas systems, the xenon storage, distillation column for krypton removal, data acquisition and slow control. The TPC calibration systems are installed in the gas recirculation and on the top of the water shield.

XENON1T was commissioned in spring 2016 and acquired science data from November 2016 to December 2018 when it was decommissioned to allow for the upgrade to XENONnT, started in spring 2019. In this section the characteristics of the XENON1T TPC and the main WIMP search results will be presented.

2.2.1 The Time Projection Chamber

The XENON1T detector is a dual-phase xenon TPC which consists of a 97 cm length and 96 cm diameter cylindrical active detection volume containing 2 t of ultra-pure liquid xenon (LXe) out of a total of 3.2 t in the detector. The side walls of the cylindrical volume are made of 24 PTFE reflectors, diamond polished, to enhance the collection efficiency for vacuum ultraviolet (VUV) light. Two arrays of photomultiplier tubes (PMTs) view the active volume, one from the bottom and one from the top with 121 and 127 Hamamatsu R11410-21 3” PMTs, respectively [111]. The PMT model was developed by Hamamatsu and the XENON collaboration with special emphasis on a very low intrinsic radioactivity level, below 13 mBq/PMT for ^{238}U and 0.4 mBq/PMT for ^{228}Th [112].

A grounded electrode, the gate, placed $\sim$2.5 mm below the liquid-gas interface, and a cathode placed at the bottom of the TPC produce a variable electric field to drift electrons produced in the liquid upwards. It was set at 120 V/cm during the first data-taking (science-run0 or SR0) and at 81 V/cm during the following one (science-run1 or SR1). To ensure drift field homogeneity, the TPC is surrounded by 74 field-shaping rings made from low-radioactivity oxygen-free high conductivity (OFHC) copper and connected by two redundant resistor chains. An anode is placed 5 mm above the gate and the 8.1 kV/cm electric field between them extracts electrons into the gaseous xenon with an efficiency of 96% [50]. Two screening electrodes are placed close to the PMT arrays and biased in order to minimise the field in front of the PMT photocathodes. A *diving bell* made of

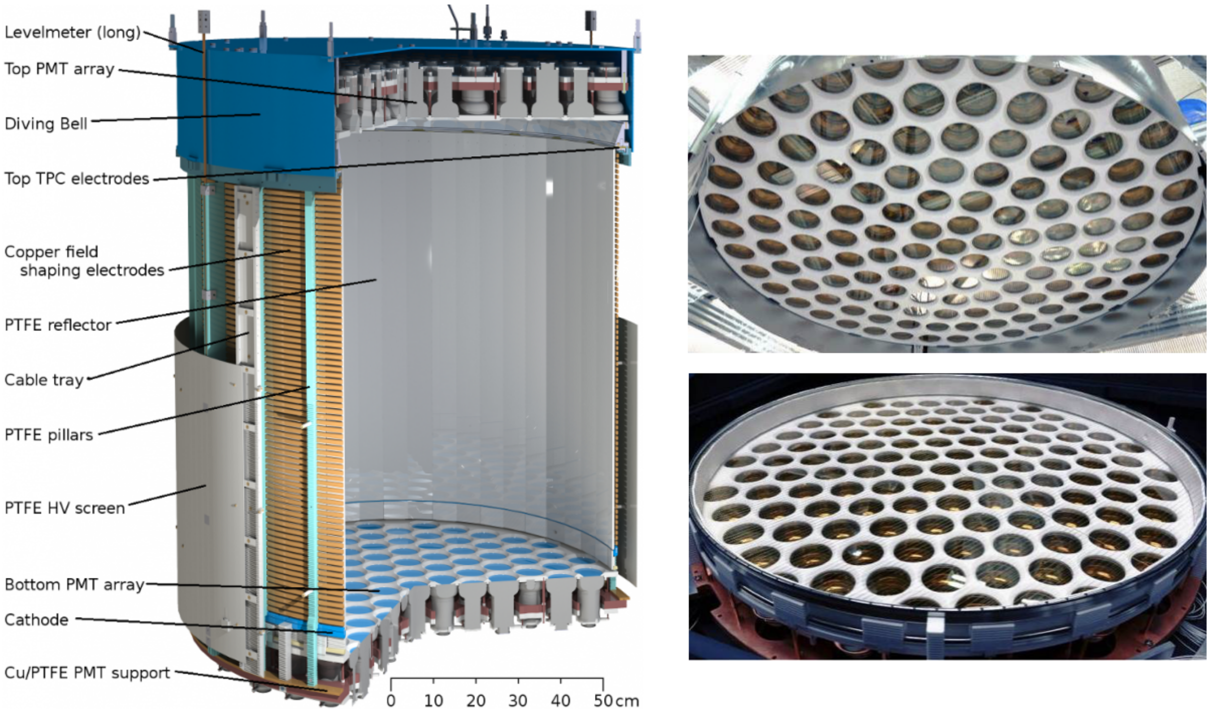

Figure 2.2: Left: drawing of the XENON1T TPC. It is built from materials selected for their low radioactivity, e.g., OFHC copper, stainless steel and PTFE. Right: pictures of the top and bottom PMT arrays, instrumented with 127 and 121 Hamamatsu R11410-21 PMTs, respectively. Figures from [111].

stainless steel is used to maintain a stable liquid-gas interface between the gate and anode electrodes. It encloses the top PMT array and it is directly pressurised by a controlled gas flow, while the height of the liquid level inside the bell is controlled via a gas-exhaust tube. Possible tilts of the TPC are measured, with a precision of $\sim$30 μm, by four parallel-plate capacitive levelmeters installed inside the bell. Two cylindrical levelmeters of 1360 mm length measure the LXe level during filling and recovery from below the cathode to above the bell, with 2 mm precision [111]. A drawing of the TPC and pictures of the PMT arrays are shown in figure 2.2.

The time delay between S1 and S2 is used to reconstruct the interaction depth (z coordinate) with a position resolution down to 0.5 mm. The distribution of the S2 light on the top PMT array is used to reconstruct the x-y position, reaching a resolution of 8 mm for S2 values above 10^3 photo-electrons (PE) [113]. The PMTs have an average quantum efficiency of 34.5% and channel-dependent gains of $(1.0\text{-}5.0)\times10^6$ [114]. The signals are guided to Phillips 776 amplifiers that provide an additional amplification factor of 10. The output of the amplifiers is sent to CAEN V1724 waveform digitiser modules to record the signals at a sampling rate of 100 MHz with a 2.25 V dynamic range, a 40 MHz input bandwidth, and 14-bit resolution [115].

2.2.2 Spin-Independent WIMP-Nucleon Cross Section

XENON1T started to take data in November 2016. The data taking was interrupted by an earthquake located close to LNGS at the end of January 2017. A first analysis of the spin-independent WIMP-nucleon cross section was performed on this short run. The detector was soon operational again and a second, longer, science run was acquired until February 2018. At the end of the data taking both runs were combined to achieve a larger livetime, 278.8 days, and increase the sensitivity of the experiment. The two science runs differ in the cathode voltage of $-12\,\mathrm{kV}$ (SR0) and $-8\,\mathrm{kV}$ (SR1), corresponding to drift fields of $120\,\mathrm{V/cm}$ and $81\,\mathrm{V/cm}$.

With SR0, after 34.1 live-days, XENON1T reached a low energy electronic recoil background of $(1.93 \pm 0.25)\times10^{-4}$ events/(kg·day·keV$_{\mathrm{ee}}$(ER energy)) in the [5, 40] keV$_{\mathrm{nr}}$ (NR energy). The analysis is performed in the inner cylindrical volume of (1042 ± 12) kg. The data are consistent with the background only hypothesis and the exclusion limit for the spin-independent WIMP-nucleon interaction cross section has a minimum of $7.7\times10^{-47}\,\mathrm{cm}^2$ for 35 GeV/c^2 WIMPs at 90% CL [116]. The combined analysis allowed for a one tonne-year exposure in 278.8 days of data taking, reaching, in (1.30 ± 0.01) t of fiducial mass and [4.9, 40.9] keV$_{\mathrm{nr}}$, an ER background of $(82^{+5}_{-3}(\mathrm{syst}) \pm 3(\mathrm{stat}))$ events/(t·yr·keV$_{\mathrm{ee}}$), the lowest achieved in a DM detector. Table 2.2 summarises the expected rate of each background component and their relative contribution to the total XENON1T ER background. The NR background includes contributions from radiogenic neutrons originating from detector materials, coherent elastic neutrino nucleus scattering (CEνNS) mainly from ^{8}B solar neutrinos, and cosmogenic neutrons from secondary particles produced by muon showers outside the TPC (rejected by the muon veto). The detector response to ERs and NRs is modelled using ^{220}Rn and ^{241}AmBe and a D-D neutron generator, respectively. The calibration data from both science runs are simultaneously fitted to account for correlations of model parameters across different sources and runs. The fit posterior is used to predict the ER and NR distributions in the analysis space of the DM search data, achieving an ER rejection of 99.7% in the signal reference region. Fast neutrons can be rejected by the high probability to undergo multi-site depositions in LXe. The detection efficiency after selections is on average 96% for S1 and slightly less than 93% for S2.

The DM search data was blinded[2] in the signal region above the S2 threshold of 200 PE and below the ER -2σ quantile in (cS1, cS2$_b$) space, where cS1 is the S1 signal corrected for relative light collection efficiency, and cS2$_b$ is the S2 signal detected by the bottom array and corrected for relative light collection efficiency and mean electron drift length.

---

[2] SR0 data were re-blinded and included in the analysis after the first publication in [116].

Table 2.2: The XENON1T ER background rates in the low energy region (1,12) $\mathrm{keV_{ee}}$ of the WIMP search and in 1.3 t fiducial volume. The contribution from each component is estimated through MC simulations. Collected XENON1T data provide constraints on the 214Pb and 85Kr abundance in the LXe reservoir.

Background component	**Rate** $[(\mathrm{t \cdot yr \cdot keV_{ee}})^{-1}]$	**Relative contribution** [%]
^{214}Pb	56±6	75
^{85}Kr	7.7±1.3	10
Detector materials	8±1	11
Solar ν	2.5±0.1	3
^{136}Xe $2\nu\beta\beta$	0.8±0.1	1
Total (MC prediction)	75±6	
Total (measured)	82^{+5}_{-3}(syst)±3(stat)	

The reconstructed position is also corrected for field non-uniformities. The blinding was set prior to the tuning and development of event selection criteria and signal and background models. The analysis is performed with an unbinned profile likelihood in (cS1, $\mathrm{cS2}_b$, R^2) parameters space and categorizing events at inner radii based on binned Z, with R the radius of the TPC and Z the vertical dimension [117]. The corners of the fiducial mass are restricted further by requiring that the predicted total background rate in the ROI is flat to <10% in Z across slices of R, such that the contribution from radio-impurities in detector materials to the ER background is subdominant relative to the uniform internal ^{214}Pb contribution. An inner region containing 0.9 t mass is used as reference region with negligible surface background rate while a further 0.65 t core mass is selected to constrain the background as it contains a significantly lower neutron rate. Figures 2.3 and 2.4 show the background and signal model shapes in various 2D projections of the analysis space compared to data. Each background component and the WIMP signal are modelled as a probability density function of all analysis dimensions. The number of events in the NR reference region in table 2.3 is consistent with background expectations. Although the number of events exceed the total background expectation in the reference region, the profile likelihood analysis indicates no significant excesses in the 1.3 t fiducial mass at any WIMP mass. This results in a weaker exclusion limit. The background only hypothesis is preferred and the exclusion limit, shown in figure 2.5, has a minimum of $4.1\times10^{-47}\,\mathrm{cm}^2$ for 30 GeV/c^2 WIMPs at 90% CL [51], the best up to date above 6 GeV/c^2.

Contribution to the Analysis: The SR0 and SR1 analysis campaigns took place during my first year of Ph.D studies. While learning the framework used by the collaboration, I contributed to the analyses within the calibration subgroup.

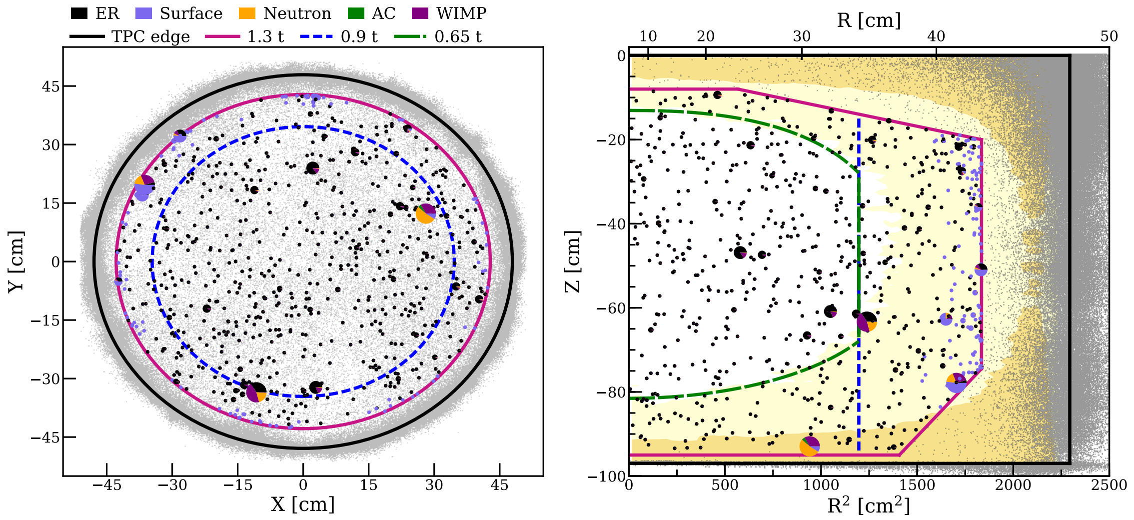

Figure 2.3: Spatial distributions of DM search data. Events that pass all selection criteria and are within the fiducial mass are drawn as pie charts representing the relative probabilities of the background and signal components for each event under the best-fit model (assuming a 200 GeV/c^2 WIMP and resulting best-fit $\sigma_{\mathrm{SI}} = 4.7{\times}10^{-47}$ cm^2) with colour code given in the legend. Small charts (mainly single-coloured) correspond to unambiguously background-like events, while events with larger WIMP probability are drawn progressively larger. Gray points are events reconstructed outside the fiducial mass. The TPC boundary (black line), 1.3 t fiducial mass (magenta), maximum radius of the reference 0.9 t mass (blue dashed), and 0.65 t core mass (green dashed) are shown. Yellow shaded regions display the 1σ (dark), and 2σ (light) probability density percentiles of the radiogenic neutron background component for SR1. Figure and caption from [51].

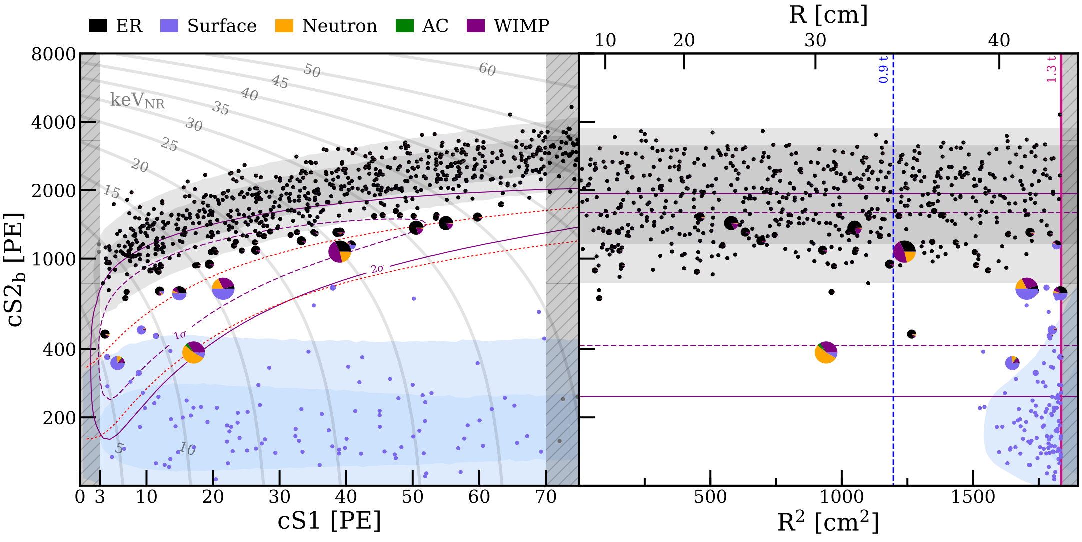

Figure 2.4: DM search data in the 1.3 t fiducial mass distributed in (cS1, cS2$_b$) (left) and (R^2, cS2$_b$) (right) parameter spaces with the same marker descriptions as in figure 2.3. Shaded regions show the projections in each space of the surface (blue) and ER (gray) background components for SR1. The 1σ (purple dashed) and 2σ (purple solid) percentiles of a 200 GeV/c^2 WIMP signal are overlaid for reference. Vertical shaded regions are outside the ROI. The NR signal reference region (left, between the two red dotted lines) and the maximum radii (right) of the 0.9 t (blue dashed) and 1.3 t (magenta solid) masses are shown. Gray lines show iso-energy contours in NR energy. Figure and caption from [51].

Table 2.3: Best fit, including a 200 GeV/c^2 WIMP signal plus background, expected event counts with 278.8 days livetime in the 1.3 t fiducial mass for the full (cS1, cS2$_b$) ROI and in the NR signal reference region. The table lists each background (BG) component separately and in total, as well as the expectation for the WIMP signal assuming the best-fit σ_{SI}=4.7×10^{-47} cm^2. The observed events from data are also shown for comparison. Although the number of events in the reference region indicate an excess compared to the background expectation, the likelihood analysis, which considers both the full parameter space and the event distribution, finds no significant WIMP-like contribution. Values and caption from [51].

Component	**1.3 t Full**	**1.3 t Reference**
ER	627±18	1.62±0.30
Neutron	1.43±0.66	0.77±0.35
CEνNS	0.05±0.01	0.03±0.01
AC	$0.47^{+0.27}_{-0.00}$	$0.10^{+0.06}_{-0.00}$
Surface	106±8	4.84±0.40
Total BG	735±20	7.36±0.61
WIMP$_{\text{best-fit}}$	3.56	1.70
Data	739	14

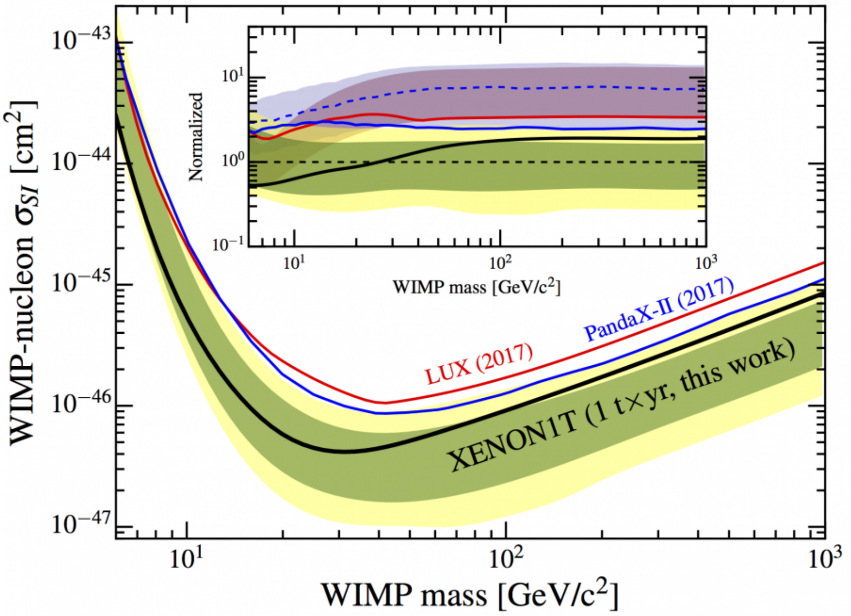

Figure 2.5: XENON1T 90% confidence level upper limit on σ_{SI} (thick black line) with the 1σ (green) and 2σ (yellow) sensitivity bands. Previous results from LUX and PandaX-II are shown for comparison. The inset shows these limits and corresponding ±1σ bands normalised to the median of XENON1T sensitivity band. The normalised median of the PandaX-II sensitivity band is shown as a dotted line. Figure and caption from [51].

Table 2.4: Electron drift velocity in LXe for different cathode voltages.

Cathode Voltage [kV]	**Drift Time [μs]**	**Drift Field [kV/cm]**	**Drift Velocity [mm/μs]**
4	972 ± 14	0.044 ± 0.011	0.997 ± 0.016
5	864 ± 11	0.053 ± 0.012	1.122 ± 0.017
6	796 ± 9	0.063 ± 0.012	1.217 ± 0.017
7	753 ± 9	0.072 ± 0.012	1.287 ± 0.018
8	725 ± 10	0.081 ± 0.012	1.337 ± 0.020

In particular, at the end of the XENON1T commissioning phase I work in determining the electron drift velocity in LXe. This was done using the $^{83\mathrm{m}}$Kr calibration data. The positions of gate and cathode were determined by two peaks at the edges of the smoothed derivative of the drift time distribution. During the commissioning phase the cathode was set to a voltage of $-15\,\mathrm{kV}$ and a nominal target length of $(969 \pm 2)\,\mathrm{mm}$ was used. This resulted in a drift velocity of $(1.488 \pm 0.007)\,\mathrm{mm}/\mu\mathrm{s}$.

During SR0 I contributed to the electron mean free path estimation. Electrons drifting through LXe can be captured by electronegative impurities and thus the size of the S2 signal is underestimated and needs to be corrected based on the depth of the interaction. The electron mean free path was computed from the degradation of the S2 signal using ^{222}Rn and $^{83\mathrm{m}}$Kr calibration data along the drift time. Moreover, the analysis on the electron drift velocity in LXe was updated for different cathode voltages used with calibration data. The results are reported in table 2.4.

During SR1 I worked on the electronic recoil energy calibration and specifically in estimating the time dependence of the g_1 and g_2 parameters needed for the energy reconstruction as shown in equation 2.11. During this period I spent some weeks at LNGS where I performed a study on the ^{220}Rn rate evolution during the calibrations, it is described in appendix B.

Other Analyses: In addition to the spin-independent WIMP-nucleon interaction cross section, the main goal of the experiment, the XENON collaboration is dedicated to explore other detection channels of interest. The spin-dependent WIMP-nucleon cross section for the proton-only and the neutron-only interactions is published [118] with the most stringent constraint to date on the WIMP-neutron cross section. A second order interaction can happen when the spin-independent channel is suppressed and a WIMP couples to a virtual pion exchanged between the nucleons in a nucleus [119]. The search for light dark matter interactions was improved by studying the contributions from inelastic processes such as the Migdal effect or bremsstrahlung [120] and using ionisation only signals that allows to lower the detection threshold [121]. An excess below 7 keV was reported searching for low mass electronic recoil DM [122]. The excess is compatible with solar axion at 3.4σ and with a neutrino magnetic moment at 3.2σ, but both results are excluded by stellar constraints. The excess can also be explained by β decays from tritium at 3.2σ, while the hypothesis of an ^{37}Ar leak is constrained and excluded. A monoenergetic peak due to bosonic dark matter is favoured at 3.0σ global (4.0σ local) significance over background.

A breakthrough was achieved when the experiment reported the first direct observation of the two neutrino double electron capture in ^{124}Xe (2νECEC) with an half-life of $(1.8\pm0.5(\text{stat.})\pm0.1(\text{sys.}))\times10^{22}$ yr and a significance of 4.4σ [123]. This very rare decay was measured for the first time directly with xenon. The result underlines once more the capability of the experiment in exploring multiple physics channels in both dark matter and neutrino fields, thanks to its high precision and resolution and the very low background rate. Several other analyses are still ongoing while this thesis is being written.

2.3 The XENONnT Experiment

XENONnT, the next generation of the xenon dual-phase TPC, is installed and commissioned in the same place as XENON1T, following the upgrade of many subsystems. It exploits 8.4 t of liquid xenon, of which 5.9 t will be used as target. If no signal will be discovered, the experiment will cover a region down to a cross section of $\sim10^{-48}$ cm^2 for the SI WIMP-nucleon interaction. While the WIMP search is the main focus of this upgrade, other analysis channels will be investigated as well. In this section, the main features of the XENONnT detector and the projected sensitivity for the main physics result will be presented.

2.3.1 Overview

The XENON1T detector support structure was built for a heavier TPC to be placed in the same cryostat, replacing only the inner stainless steel vessel. Similarly, the xenon cryogenics and purification systems as well as the recovery system were designed to handle a target mass scale-up to about 8 tonnes. The design of the new detector follows closely that of the previous one, with a scale-up in diameter and drift length. Four new systems were installed to enable the handling and purification of the larger xenon mass and to achieve the required background reduction compared to XENON1T. The first one is an online radon removal system based on the reverse technology used for the cryogenic

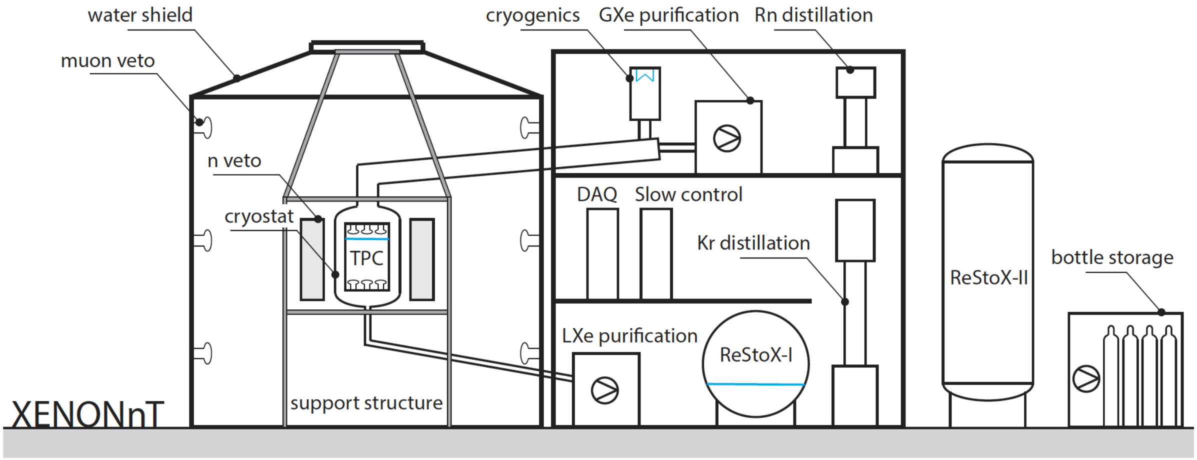

Figure 2.6: Schematic view of XENONnT and its subsystems.

distillation column built for XENON1T to reduce the ^{85}Kr background [124]. A second new system is an additional storage for the large amount of xenon used in XENONnT, with a storage capacity of 10 t in addition to the 7.6 t of the XENON1T system. Compared to XENON1T where the xenon was purified only in the gas phase, XENONnT will also exploit a new liquid xenon purification stage. A final new system is a veto detector to tag neutrons which scatter inside the TPC, leaving a single-scatter nuclear recoil signal like the one expected for a WIMP event. The scintillation light will be detected by an additional array of 120 Hamamatsu R5912-100-10 8” high quantum efficiency (40% on average) PMTs, placed in the water tank outside of the acrylic vessels that will contain 0.2% Gd-loaded water [125].

2.3.2 The Time Projection Chamber

XENONnT exploits a TPC similar to the one already used by XENON1T. The active region, ∼148 cm high and ∼134 cm wide, is enclosed by 24 PTFE reflector panels, held by 24 blocking panels to optically isolate the active volume. The PTFE has a high reflectivity that allows for the collection of the light produced in the interactions, but it is also a source of neutron background due to the high (α,n)-cross section of ^{19}F. For this reason the amount of PTFE is minimised and the panels are only 2 mm thick (5 mm at a few positions) [125]. 494 PMTs 3” Hamamatsu R11410-21 are used to detect the light coming from interactions in LXe, arranged in two hexagonal arrays, 253 in the top and 241 at the bottom, of which 178 are coming from XENON1T and 316 are new sensors. Compared to the PMTs used in the XENON1T experiment, the new model is improved with respect to mechanical leak-tightness and light emission. Their average quantum efficiency is 34.1%

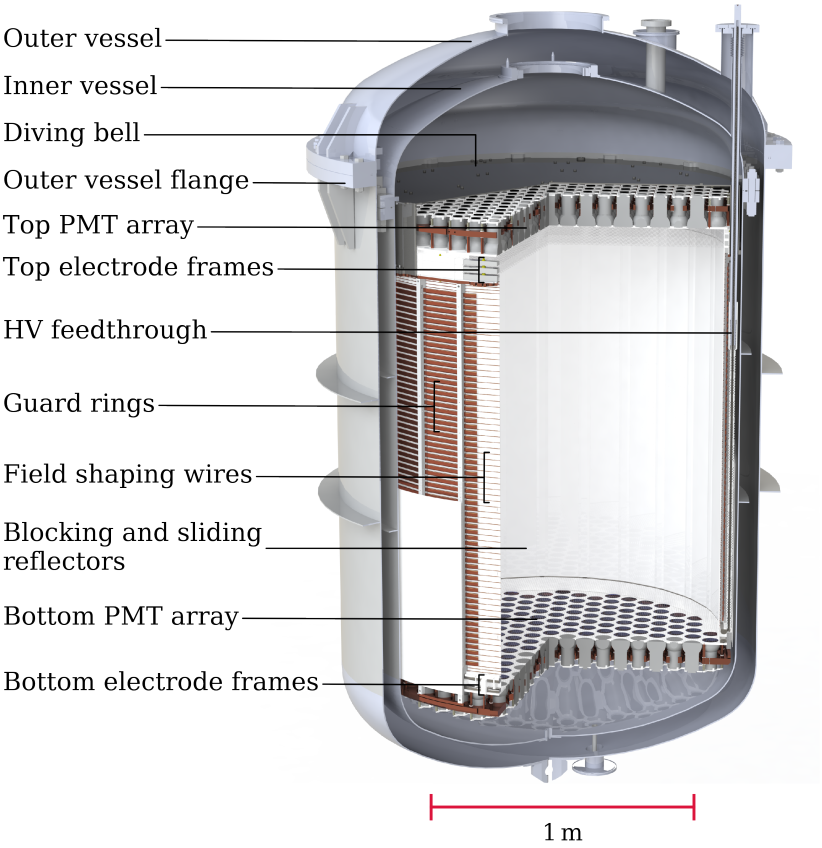

Figure 2.7: CAD rendering of the XENONnT TPC with the PMT arrays in the cryostat. Figure from [126].

at the xenon scintillation wavelength of 178 nm. The light calibration system that allows to calibrate all the PMTs during the commissioning and to routinely monitor them during the data taking was developed in the framework of this thesis and is described in detail in section 5.1. The top PMT array is placed into a diving bell, used to control the LXe level, as in XENON1T, with a precision of $\sim 30\,\mu\text{m}$[3]. Eight capacitive levelmeters, four parallel-plate inside the bell, two medium (365 mm) and two long (1500 mm) ones, are used to monitor the liquid level. Seven PT100 resistors are also installed to measure the temperature, both in the gas xenon phase and in the LXe. A rendering of the XENONnT TPC, together with the PMT arrays and the cryostat, is shown in figure 2.7.

Five electrodes are used to create the electric fields in the TPC. The cathode and gate are placed in LXe at the bottom of the TPC and close to the liquid-gas interface, respectively, and produce the drift field. The cathode is designed to be negatively biased down to -30 kV to operate the TPC at an electric drift field of 200 V/cm. The voltage is

---

[3] This is the precision by design. Additional systematics due to machining and positioning reduce the precision to 0.1 mm.

provided by the Heinzinger PNC 150000-1 negative supply already used for XENON1T. The extraction field of ~8 kV/cm in the gas phase is established between the gate and the anode, located in the xenon gas 8 mm above the gate. Two screening electrodes are installed between the field cage and the top and bottom PMT arrays, respectively. They are kept at the average bias voltage of all PMTs in the respective array to realise a field-free region. For a sketch of the electrode positions refer to figure 2.1. The electrodes are grids made from 216 μm (304 μm for the cathode) thick stainless steel parallel wires. On the gate and anode electrodes two and four perpendicular wires (304 μm) are installed, respectively, to avoid wire sagging due to the electrostatic force. To allow for field uniformity, 71 field shaping wires and 64 guard rings, made of OFHC copper, are installed all around the TPC. Two redundant voltage divider chains (5 GΩ each resistor) are attached to thin copper wires and fixed between the shaping rings, and two to the wires, using M2 stainless steel screws. In order to mitigate possible charge accumulation on the PTFE reflectors, the field shaping electrodes are segmented for XENONnT and follow the polygonal structure of the interlocking TPC reflectors, touching each reflector panel at three points. Moreover, 5 charge draining holes, of 0.50 mm diameter, were added in correspondence of each shaping wire and on each reflector panel [125]. They allow the electrons to flow out of the active volume following the field lines instead of being blocked and accumulate on the walls.

2.3.3 Physics Reach

To increase the sensitivity to the spin-independent WIMP-nucleon cross section, a reduction of the total background and a larger target mass are foreseen in XENONnT, as described in the previous section. To estimate the projected sensitivity, the XENONnT detector, the particle generation and their propagation through the detector volumes are simulated with GEANT4 [127]. The energy released in LXe is characterised and parametrised following the NEST (Noble Element Simulation Technique) approach [128]. The simulation is also taking into account fluctuations, recombination and electric drift field dependence. The S1 and S2 signals are reconstructed to perform the sensitivity study. The propagation of the prompt scintillation photons (S1) in the TPC is also simulated with GEANT4, as described in [129], in order to estimate the light collection efficiency (LCE) of the photocathode of the PMTs. The average LCE in the TPC is 36%, ranging from a maximum of ~50% at the bottom of the TPC to ~25% in the top region, caused by internal reflection at the liquid-gas interface [126]. The S2 signals produced by electrons generated at the interaction vertex are simulated assuming a drift field of 200 V/cm and the target electron mean-free-path of 1000 μs.

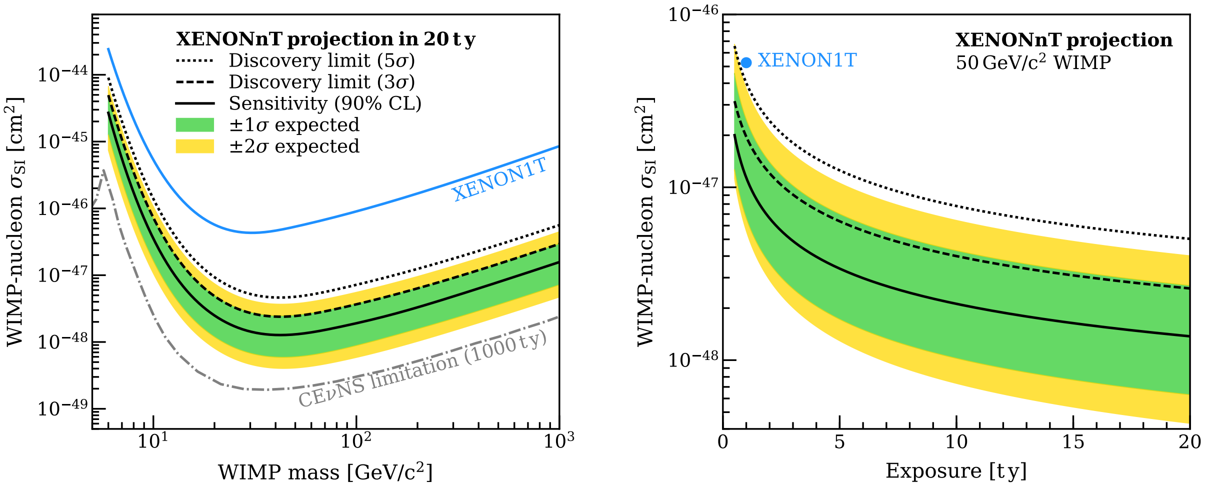

Figure 2.8: Projection of the XENONnT sensitivity and discovery power in the search for spin-independent WIMP-nucleon couplings. Left: median 90% CL exclusion limit (black solid line) for a 20 t·y exposure, with the 1σ (green) and 2σ (yellow) bands. The current strongest exclusion limit, obtained with XENON1T, is shown in blue. The grey dashed-dotted line represents the discovery limit of an idealised LXe-based experiment with CEνNS as the unique background source and a 1000 t·y exposure. Right: sensitivity, for a 50 GeV/c^2 WIMP, as a function of exposure. The dashed (dotted) black lines in both panels indicate the smallest cross section at which the experiment would have a 50% chance of observing a 3σ (5σ) excess. Figure and description from [126].

Background coming from materials, LXe and intrinsic components are estimated by simulating particles that generate electronic and/or nuclear recoils. While sources dissolved into the xenon are uniform in the whole volume, such as ^{214}Pb coming from ^{222}Rn, and ^{85}Kr, the radioactivity coming from detector components is shielded by the LXe itself. Thus the sensitivity projection to SI WIMP-nucleon interaction is computed in an inner cylindrical fiducial volume containing 4 t of LXe. Screening measurements are used to select the materials and constrain the simulated background components in the region of interest of (1,13) keV$_{\text{ee}}$ and (4,50) keV$_{\text{nr}}$. Details on the screening and background rate assumptions are reported in [126]. The total expected ER background rate is $(13.1\pm0.6)\,(\text{t}\cdot\text{yr}\cdot\text{keV}_{\text{ee}})^{-1}$, six times less than the $(82^{+5}_{-3}(\text{syst})\pm3(\text{stat}))\,(\text{t}\cdot\text{yr}\cdot\text{keV}_{\text{ee}})^{-1}$ measured in XENON1T, while the predicted NR rate is $(2.2\pm0.5)\times10^{-3}\,(\text{t}\cdot\text{yr}\cdot\text{keV}_{\text{ee}})^{-1}$. The statistical model is similar to the one used in XENON1T [117] but without the spatial dimensions, thus only in (cS1, cS2$_b$) parameter space. The projected sensitivity, computed using the profile likelihood ratio method, for a 20 t·y exposure and the discovery power are shown in figure 2.8. The median exclusion limit at 90% CL, for a five year livetime with 4 t fiducial mass, reaches the strongest sensitivity of 1.4×10^{-48} cm^2 for a 50 GeV/c^2 WIMP, improving upon the current XENON1T result by more than one order of magnitude. The minimum cross-section for a 50% probability to observe an excess of 3σ significance is estimated to be 2.6×10^{-48} cm^2.

CHAPTER 3

Signal Reconstruction in the MeV Energy Range

The capability to reconstruct the signals at the Q-value of the neutrinoless double beta decay determines, together with other characteristics, the possibility for an experiment to search for this decay. Dual-phase TPCs designed for DM searches are optimised to work in the few keV electron recoil energies. To simultaneously search for DM and ^{136}Xe $0\nu\beta\beta$ with the XENON project, several improvements in the MeV region need to be made. In section 3.1 the existing procedure for the signal reconstruction in the DM region of interest is summarised. Section 3.2 describes the software corrections developed for the MeV[1] electronic recoil region in order to achieve the best signal reconstruction and energy resolution possible. The energy calibration and reconstruction technique is reported in section 3.3, with the results obtained following the corrections for the high-energy region. An outlook of the chapter is given in section 3.4. The work highlighted in this chapter is carried out by the author of this thesis together with other members of the XENON collaboration, and it is published in [109]. In particular, my work was focused on the saturation correction technique and on the electronic recoil energy calibration procedure, resulting in the final energy resolution.

3.1 Signal Reconstruction in XENON1T

Data in the XENON1T experiment are reconstructed by the modular software package Processor for Analyzing XENON (PAX) [130]. The modularity allows to create or modify different parts of the processor chain using *plugins*. In the XENON1T processor a *pulse* is a $\sim 1\,\mu$s block of samples from a single digitiser channel, connected to a single PMT. Several *plugins* are used to compute basic pulse properties and to assign them to a given *event*. An event is a collection of pulses from several channels and within each event the

---

[1] MeV energies are considered high energies compared to the standard DM search.

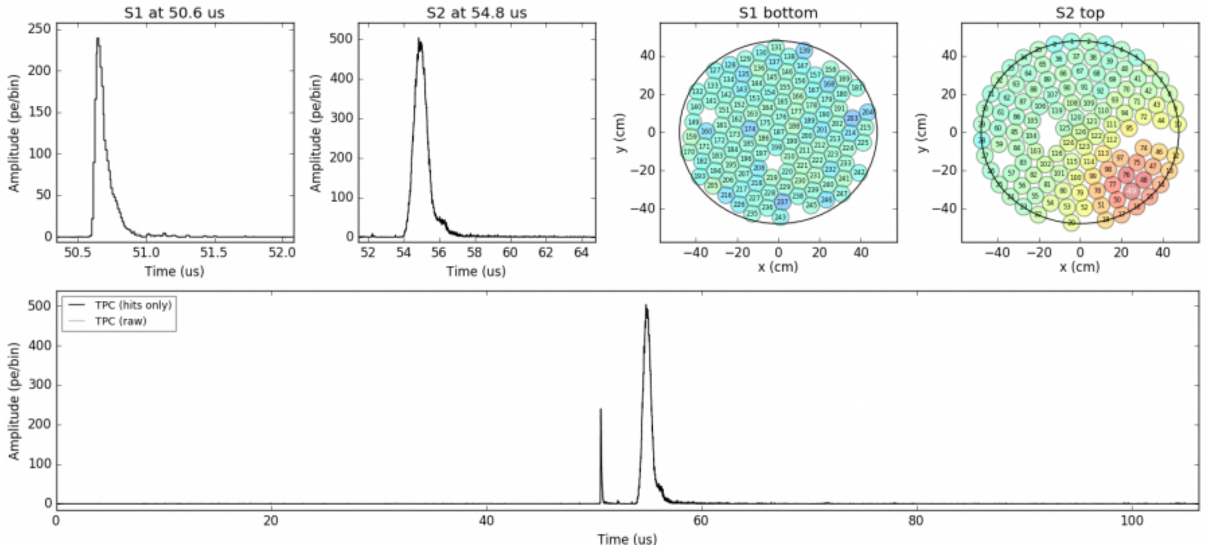

Figure 3.1: One of the first XENON1T events after processing. The bottom panel shows the sum waveform of all the PMTs. In the top panels the largest S1 and S2 coupled as an interaction and the hit pattern in the PMT arrays are shown. As the light is more localised in the top, this PMT array is used for the (x-y) position reconstruction.

pulses are clustered into *peaks* that are recognised as S1s or S2s based on their rise-time. The peaks are then ordered according to the size of their area and the largest S1 and S2 are paired as an interaction. One of the first processed events is shown in the bottom panel of figure 3.1. In the top panels the largest S1 and S2 signals and the hit pattern on the PMT arrays are highlighted.

Challenges in the MeV Region: One of the issues in looking for WIMP interactions with a nucleus is the lower threshold of the photo-detection efficiency, the number of photoelectrons detected for each photon/electron produced. Having a lower threshold allows to explore lower-mass DM candidates that would produce a smaller nuclear recoil. While the S2s are amplified by the multiplication in the gas phase, the smaller S1 signals and the requirement of at least 3 contributing PMTs to define an S1 are the limiting factors on the lower threshold. For this reason in XENON1T all the channels are amplified by a factor 10 to detect light as small as a single PE in each PMT. This means on the other hand that the 2.25 V ADC dynamic range starts to be saturated for more energetic interactions, $\mathcal{O}(100\,\text{GeV})$.

When looking into the possibility to perform the ^{136}Xe $0\nu\beta\beta$ search with XENON1T, the first indication that the signal reconstruction and corrections developed for the DM search were not directly applicable to the high-energy region came from the energy resolution. The main contribution to the resolution comes from the statistical fluctuations of the electron multiplication on the PMT dynodes. This is a Poisson process and thus, for a linear detector response, we expect the average amplitude H to be proportional to the number of charge carriers N, so that $H = kN$ with k as proportionality constant. The standard deviation is $\sigma = k\sqrt{N}$. The resolution R, limited only by the statistical fluctuations, is then [131]:

$$R_{\text{Poisson}} = \frac{\text{FWHM}}{H} = \frac{2.35k\sqrt{N}}{kN} = \frac{2.35}{\sqrt{N}} \tag{3.1}$$

The amplitude H and the number of charge carriers N are also proportional to the energy released in the interaction, E. Thus, in XENON1T the relative energy resolution can be written as:

$$\frac{\sigma(E)}{E} = \frac{a}{\sqrt{E}} + b \tag{3.2}$$

where a and b are parameters to be determined during the calibration process. In particular b takes into account the contribution provided by the recombination fluctuations in LXe. The energy resolution computed during the SR1 WIMP analysis showed a degradation with respect to the trend of equation 3.2 in the MeV region. Looking at a few waveforms it was evident that the ADC saturation was present for S2 signals, and it was causing an incorrect estimation of the S2 properties. The saturation is affecting interactions as low as ∼200 keV. Going to higher energies it becomes more relevant and involves more channels. The saturation of each channel for a given event depends also on the x-y location of the interaction, as closer PMTs receive a larger amount of light. More details on the saturation effects and its correction are described in section 3.2.1.

Experiments dedicated to $0\nu\beta\beta$ detection optimise their electronics and readout for the typical signals and energy region of the decay. Aiming at a simultaneous search for DM and $0\nu\beta\beta$ with the same detector requires the reconstruction of the signals from the single PE to the MeV scale. It is thus necessary to work on hardware implementations, possible for future experiments (see end of section 3.2.1), and the development of software techniques to increase the data quality.

3.2 High Energy Reconstruction

In this section the work performed to reconstruct the signals and allow for a linear response of the detector up to a few MeV is described. In particular, the most relevant correction is the one for saturated pulses. Other corrections are implemented to improve the clustering algorithm to identify and reject the contribution of secondary signals not caused by the particle interactions, but by detector effects (see section 3.2.2).

3.2.1 Saturation Correction

The first correction implemented at processor level is performed to reconstruct, for each event, the waveforms in the channels saturated by the digitisers. The ADC saturation has a distinctive signature, producing truncated waveforms at 2.25 V, as shown by the black line in figure 3.2. For S2 signals of 1 μs width it corresponds to $\sim 10^{11}$ electrons. For PMT gains of about 2×10^6 and an additional factor 10 provided by the amplifiers as in XENON1T, this means that the ADC saturates for interactions producing S2 signals larger than 10^4 PE in a single PMT, corresponding to a total S2 of $\sim 10^5$ PE. The saturation is affecting the top array for signals as low as ~200 keV while the bottom array is affected starting from interactions of ~1500 keV, because the S2s are produced and amplified in the gas phase, at the top of the TPC. This indirectly affects also the x-y position reconstruction of the interactions, determined by the top PMT array due to the larger and more localised signal.

The correction is based on a template of the S2 signal shape defined event-by-event from the non-saturated channels. The dominant contribution to the S2 shape is coming from the electron cloud drifting from the liquid-gas interface to the anode, and thus for a given interaction the shape is the same in each channel. Its size is different from channel to channel. PMTs closer to the x-y position of the interaction will detect more light, while the ones further away see less light. This means that for every event there are some channels that do not saturate the ADC, and they can be used to define the template. For each saturated peak that exceeds the ADC range, the correction is as follow:

1. The pulses in all the channels are split into ADC saturated or unsaturated categories.
2. For each saturated pulse all the saturated samples[2] of the waveform are identified.
3. A *reference region* is defined as 100 samples (1 μs) before the first saturated sample. This region is shown in pink in figure 3.2.
4. All the non-saturated pulses in the other channels that correspond in time to the saturated pulse to correct are selected, and their sum waveform is computed to define the template;
5. The template is scaled according to the ratio between the saturated pulse and the template itself in the reference region. The scaled template used as a model is shown by the red line in figure 3.2.

---

[2] Acquisition sample. 1 sample = 10 ns.

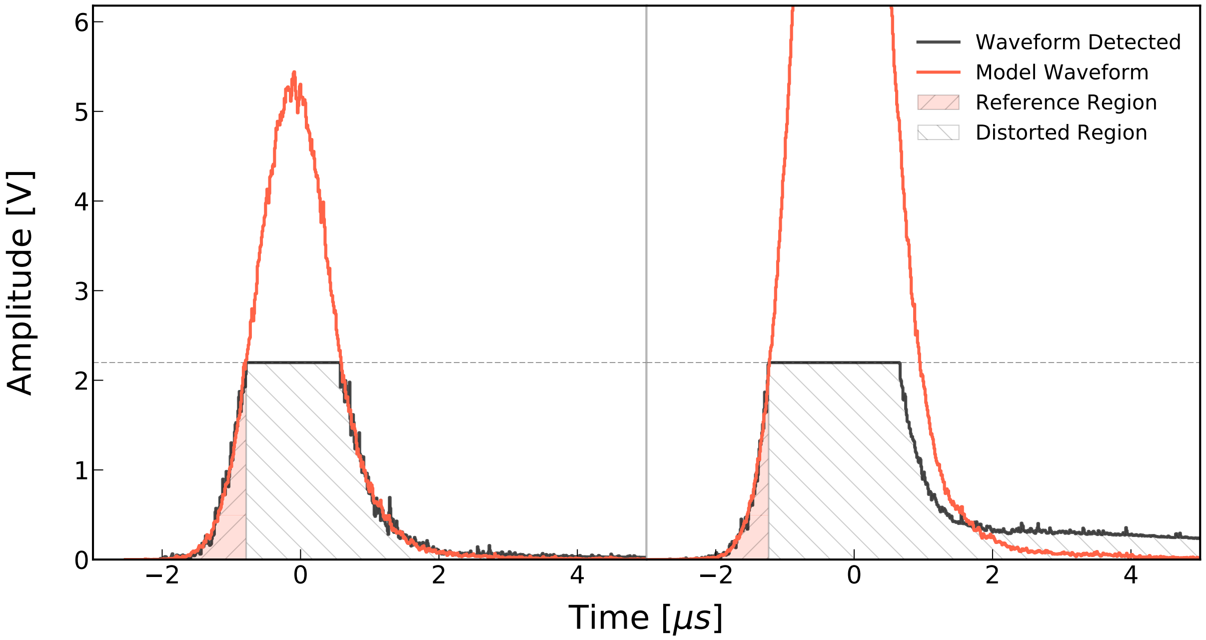

Figure 3.2: Examples of saturated waveforms (black) from two S2s with a size of about 2×10^5 PE (left) and 10^6 PE (right). Each panel shows a single channel centred to time zero. Both waveforms are truncated due to the range of the digitiser. The model, obtained from the sum of non-saturated waveforms, is scaled and overlaid in the plot (red). The pink shaded regions each cover 1 μs before the first truncated sample and are used as a reference region, while the hatched region from the first truncated sample to the end of the pulse covers the range where waveforms are corrected as the scaled model.

6. The saturated pulse is reconstructed using the scaled model in a region defined by the first saturated sample and the end of the window. The region where the correction is applied is indicated by the white hatched region in figure 3.2.

If the difference between two consecutive values of the saturated waveform is larger than 100 samples (the amount needed to define a reference region) it means that more saturated pulses are present in a window. In this case the window is split into two different ones with the second window starting before the beginning of the second reference region. Each peak is then corrected according to the method enumerated above. The correction is not limited to the region where the ADC is saturated, but it extends to the right side of the pulses. If on the right side of the saturated pulse there are other non-saturated pulses, the correction stops when the derivative of the smoothed waveform increases more than 2 PE/ns. This is done because for events with S2 of the order of 10^5 PE in a single PMT and total S2 of $\sim 10^6$ PE, we observed distortions in the right tail of the signal with the baseline not being restored to its original value. An example is shown in the right panel of figure 3.2. The distortions on the decay time of the signals are not due to the ADC saturation but they can be caused by saturation or non-linearity of other components. For example PMT bases are tested to be linear up to the ADC saturation range but, for

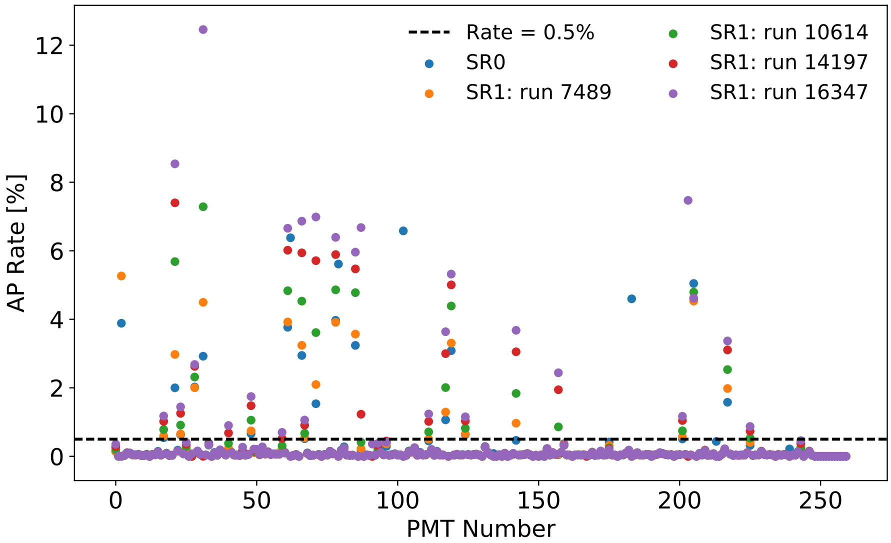

Figure 3.3: Rate of xenon APs in the five LED datasets used to monitor SR0 and SR1. The PMTs with a rate larger than 0.5% are excluded from the S2 template waveform.

signals an order of magnitude larger, space charge effects can be relevant and produce the undershoot visible between 1 and 2 μs on the tail of the event shown in figure 3.2. The following overshoot is instead caused by secondary signals.

Residual gas in the PMTs can create a secondary signal when ionised by the electrons produced by an interaction. These signals are called afterpulses (APs). To reduce the impact of APs on the S2 template, the PMTs with a xenon AP rate larger than 0.5% are excluded when building the model. To monitor the contribution during time, five LED calibration datasets are used, one for SR0 and four for SR1. In the latter case all the PMTs exceeding the threshold in at least one of the dataset are excluded. The result is shown in figure 3.3. A total of 15 PMTs were excluded from the S2 templates during SR0 and 19 during SR1. They are the following:

- SR0: [2, 21, 28, 31, 61, 62, 66, 78, 79, 85, 102, 119, 183, 205, 217]
- SR1: [2, 21, 23, 28, 31, 48, 61, 66, 71, 78, 85, 87, 117, 119, 142, 157, 203, 205, 217]

A further validation of the saturation correction technique will be tested with XENONnT. The amplifiers have been customised with a double gain output, specifically a factor 10 amplification for the DM search and a factor 2 reduction for the high-energy physics channels, meaning a total reduction of a factor 20 compared to the DM amplification. Due to experimental constraints, only the top PMT array reduced output is connected to digitisers and used. This will allow to compare the saturated events reconstructed using the software technique described here with the same events not affected by the digitisers saturation and either to validate or provide further information to improve the reconstruction.

3.2.2 Additional Corrections

As mentioned in the previous section, APs constitutes a source of secondary signals not induced by particle interactions but that can distort the reconstruction and estimation of the main S1 or S2. Single electrons in the LXe produce S2-like signals called photoionisation (PI). These are produced by photo-detachment of electronegative impurities and by the photoelectric effect at metal surfaces like the gate electrode. PI is also contributing to secondary signals. These events follow a particle interaction and affect the signal edges definition and thus its size and properties.

Few algorithms define the procedure to cluster pulses and peaks. These include parameters that are tuned for the WIMP search and they do not take into account effects more relevant at higher energies. In particular we need to consider the higher rate of multi-site (MS) interactions whose S2s overlap and are difficult to identify. Furthermore a higher rate of AP and PI, that do not distribute discretely as it happens after an interaction of a few keV, makes the time thresholds developed for the WIMP search not ideal at higher energy. Thus a further improvement was done on the clustering algorithm of the processor. Two complementary methods were developed to split the signals:

- The waveforms are smoothed and its local minima are used to define peak boundaries. The minima correspond to the end of the S1 and the beginning of the following S2. If MS are present, local minima are found between overlapping S2s.
- A cut-off threshold is defined on the right side of the signals. This is placed at the 3σ of a Gaussian function whose height matches the one of the signal.

When the boundaries defined by the two methods do not coincide, the one closer to the main signal is chosen. An interaction with an S1 and multiple S2s is shown as an example in figure 3.4. Even with the updates on the clustering software, the contribution of secondary signals on S2s cannot be completely rejected. Thus, as done for the saturation correction, PMTs with large AP rates have been excluded from the signal reconstruction. These are the same shown in figure 3.3 and listed in section 3.2.1.

Following the implementation of the corrections for the high energies, two months of data acquired during SR1 were processed and the performance on the signal reconstruction was checked along the whole energy range. No degradation in the WIMP search energy

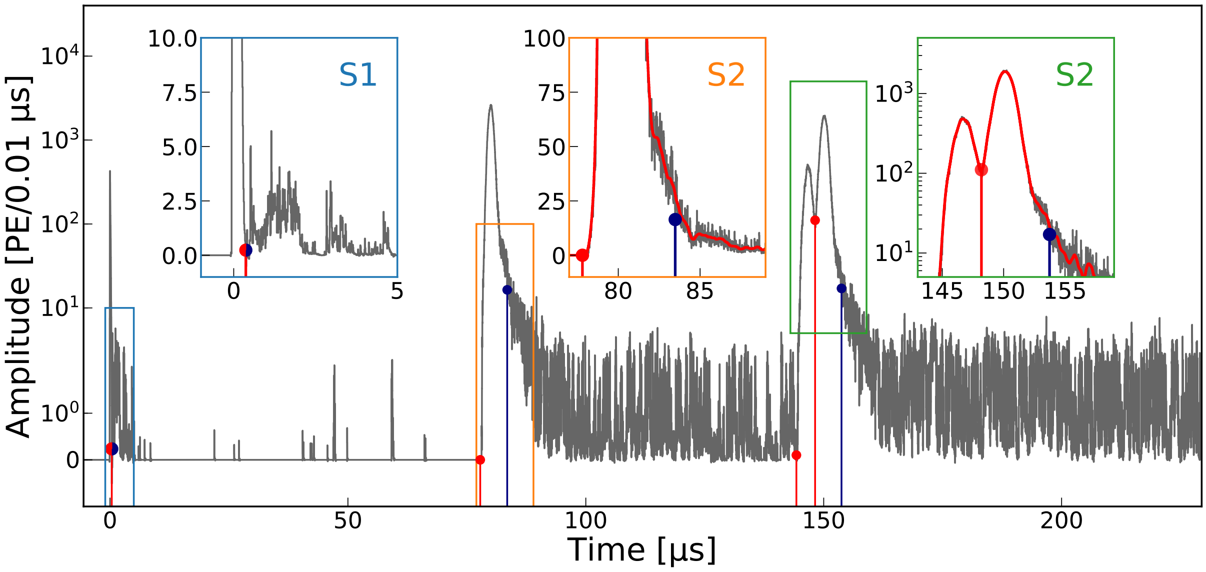

Figure 3.4: Example of a high-energy event induced by a series of Compton scatters in the LXe. The smoothed waveforms are shown as red lines in the insets, overlapped with the original ones in grey. These events typically have a narrow S1 peak and a few S2 peaks, each of which is followed by secondary signals from AP and PI processes. The effect of the algorithms on each peak is highlighted by the insets, with the final peak edges shown by vertical red and blue lines. The red points represent the local minima that define the end of the S1 signal and the start of each S2 signal. The blue points represent the 3σ threshold of the peak size. While secondary signals are clearly separated from the S1 peak, they overlap with S2 peaks.

range and an improvement in the linearity and resolution in the MeV range were observed. A new stable version of the processor was thus released, *pax_v6.10.1*. To understand their impact on the S1 and S2 signals and on the position reconstruction, figure 3.5 shows the relative shift in signal size and x-y reconstructed position using the new version of the processor and the previous stable version used for the dark matter search, *pax_v6.8.0*. The variation on the S2 signal size can be as large as 50%, while the effect on the S1s is much smaller given that it is related to the clustering only. The position reconstruction, here reported using a neural network with TensorFlow [132] backend, varies up to 30%. This confirms, as expected, that the impact of the saturation correction is not only directly related to the S2 signal size but it is also indirectly affecting the position reconstruction, based on the light pattern of the S2 on the top PMT array.

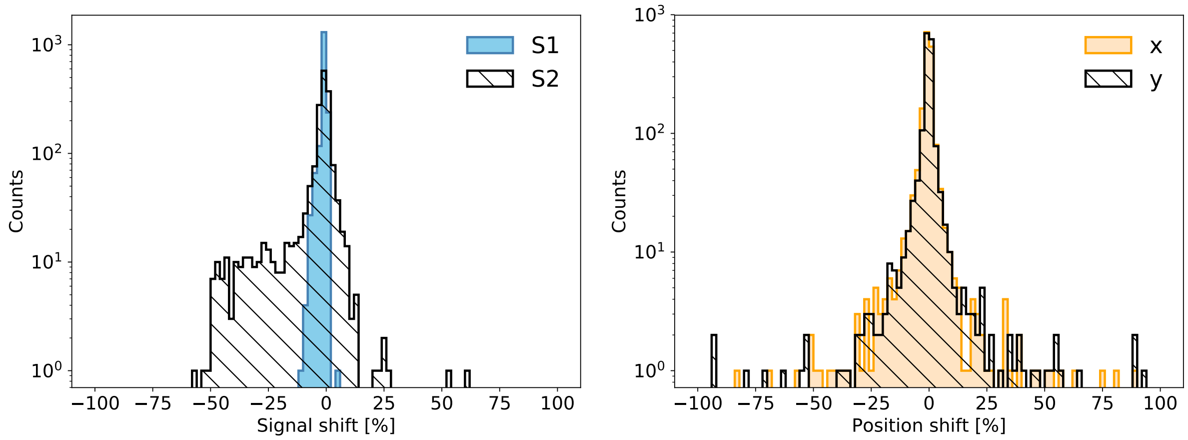

Figure 3.5: Relative differences in S1 and S2 size (left) and reconstructed x and y positions (right) between the same dataset processed after implementing the new corrections, *pax_v6.10.1*, and processed with the previous stable version, *pax_v6.8.0*. Each of the four variables, v=S1, S2, x, y, indicated in the legends is defined as $\frac{v_{6.10.1} - v_{6.8.0}}{v_{6.8.0}}$ where the subscript indicates the version of the processor used.

3.3 Electronic Recoil Energy Calibration

In XENON1T the ^{136}Xe $0\nu\beta\beta$ search looks for single-site (SS) interactions of two unresolved betas. The two betas resulting from the decay are emitted at the same interaction point and their penetration length is less than 3 mm, smaller than the x-y spatial resolution of the detector, i.e. 8 mm for events with S2 larger than 10^3 PE. However, energetic Bremsstrahlung photons emitted during electron thermalisation have a mean free path of $\mathcal{O}(10\,\text{mm})$, resulting in an energy deposition that can be disguised as MS interaction. Thus identifying the MS events is a powerful tool to understand the background and constrain its components. Thus the calibration is performed both for SS and MS events, selected in an inner 1T cylindrical volume. The new clustering algorithms help to split SS from MS interactions. However residual AP and PI can create a second tiny S2 in the SS interactions. The topology of a MS event instead consists of an S1 followed by multiple S2s. To distinguish a population due to MS particle interactions, and reject the ones produced by AP or PI, a few requirements on the size and width of the multiple S2s, on their time difference with the S1 and the event pattern on the top array are applied. The different types of interactions are represented in figure 3.6.

In this section the energy reconstruction and resolution for SS and MS interactions, following the new corrections and updates at high energies, are presented.

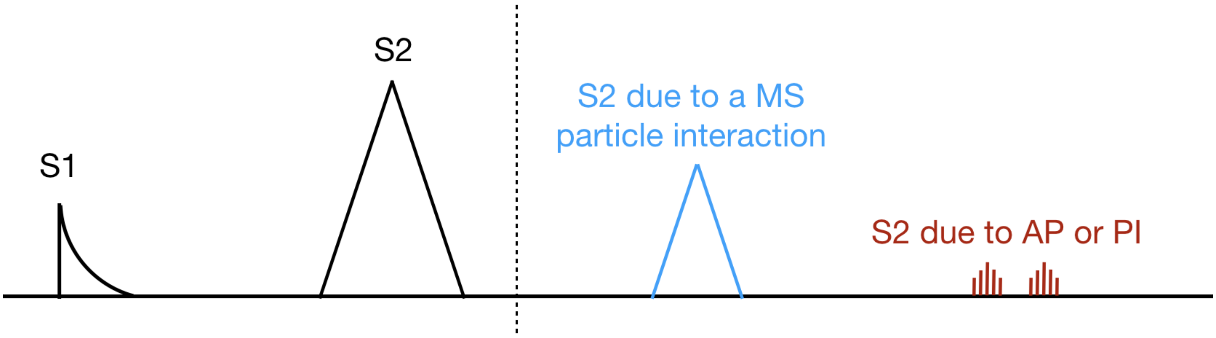

Figure 3.6: Topology of the events detected in XENON1T. On the left of the vertical dashed line, the main S1 and S2 are shown in black. On the right of the dashed line the typical secondary S2s that can be due to a MS particle interaction (blue) or to AP and PI (red).

3.3.1 Energy Reconstruction and Resolution

The particle interaction in LXe is introduced in section 2.1. Experimentally the electronic recoil energy for each event can be estimated from the S1 and S2 size, as shown by equation 2.11, once g_1 and g_2 are known. These are detector-dependent parameters that can be determined using mono-energetic peaks of known nominal energy. We can rewrite this relation as:

$$\mathrm{QY} = -\frac{g_2}{g_1}\mathrm{LY} + \frac{g_2}{W} \ , \tag{3.3}$$

where QY = S2/E and LY = S1/E are the mean charge yields and the mean light yields, respectively, at each energy. In XENON1T the main available mono-energetic lines coming either from calibration sources or radioactive contaminants are $^{83\mathrm{m}}$Kr, $^{129\mathrm{m}}$Xe, $^{131\mathrm{m}}$Xe, ^{60}Co, ^{40}K, ^{214}Bi and ^{208}Tl. These are reported in table 3.1. The SR1 background distribution for SS and MS events are shown in figure 3.7. As for the DM search, the S1 and S2 signals are corrected for the relative light collection efficiency based on the position of the interaction. The correction maps, derived from $^{83\mathrm{m}}$Kr calibration data, were updated excluding the PMTs with high AP rate (listed in section 3.2.1). The combined S1 signal of the MS events is corrected for the weighted average of the multiple S2s collection efficiency. The S2 signal is corrected also for the mean electron drift length, as described in section 2.2.2. In the analysis only the bottom component of the S2 is used because non-operational PMTs affect the uniformity of the LCE at the top.

To determine the LY and QY for the calibration, each mono-energetic line in figure 3.7 was fit with a 2-dimensional rotated Gaussian:

$$f(x, y) = A \exp\left[- \Big(a(x - x_0)^2 + 2b(x - x_0)(y - y_0) + c(y - y_0)^2 \Big) \right] \tag{3.4}$$

Table 3.1: Mono-energetic lines used for the electronic recoil energy calibration. Values from [133].

Energy [keV]	**Isotope**	**Half-life**
41.5	$^{83\mathrm{m}}$Kr	1.83 h
163.9	$^{131\mathrm{m}}$Xe	11.84 d
236.1	$^{129\mathrm{m}}$Xe	8.88 d
609.3	^{214}Bi	19.9 m
1120.3	^{214}Bi	19.9 m
1173.2	^{60}Co	5.2714 y
1332.5	^{60}Co	5.2714 y
1460.8	^{40}K	1.277×10^{9} y
1764.5	^{214}Bi	19.9 m
1847.4	^{214}Bi	19.9 m
2118.6	^{214}Bi	19.9 m
2204.2	^{214}Bi	19.9 m
2614.5	^{208}Tl	3.053 m

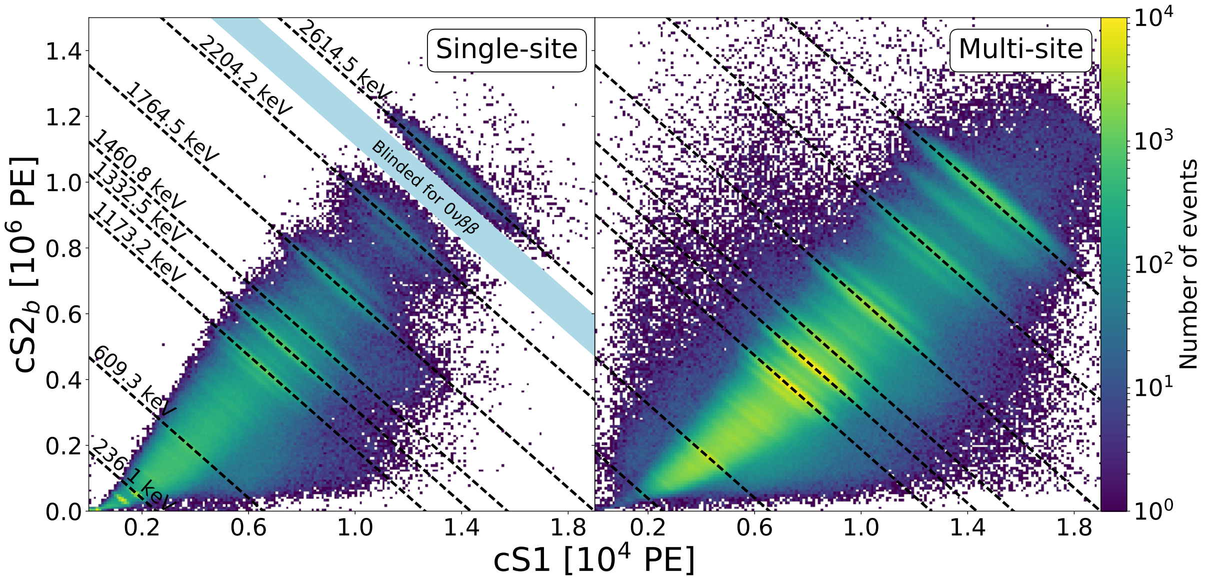

Figure 3.7: Single-site (left) and multi-site (right) background event distributions during SR1, in corrected S1 (cS1) and corrected S2 bottom (cS2$_b$) space. Mono-energetic photo-absorption peaks of gamma-rays are labelled with their energies and corresponding sources. SS events with energies around Q$_{\beta\beta}$ are blinded.

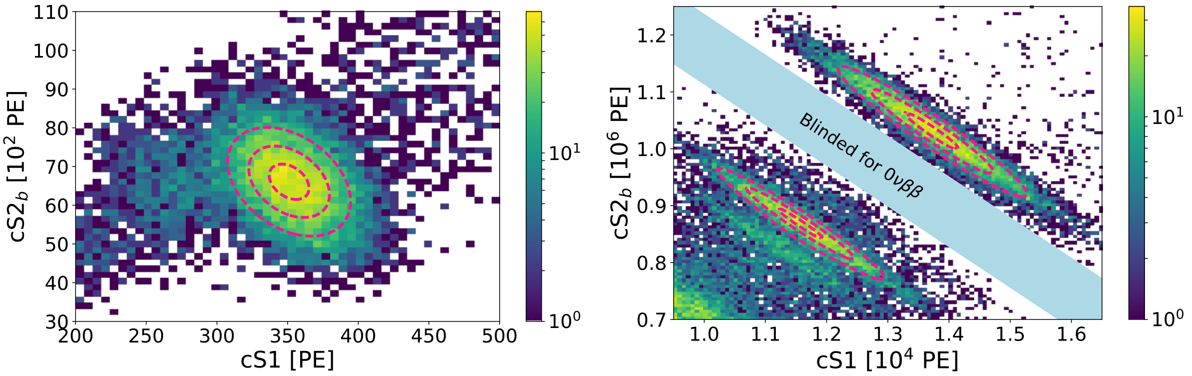

Figure 3.8: Two-dimensional rotated Gaussian fit (magenta lines) for the $^{83\mathrm{m}}$Kr line at 41.5 keV (left). This line originates from the superimposition of the unresolved 9.4 keV and 32.1 keV peaks. Similarly for the ^{214}Bi line at 2204.2 keV and the ^{208}Tl at 2614.5 keV (right) in the sidebands of the blinded region.

with

$$a = \frac{\cos^2\theta}{2\sigma_x^2} + \frac{\sin^2\theta}{2\sigma_y^2}, \qquad b = -\frac{\sin 2\theta}{4\sigma_x^2} + \frac{\sin 2\theta}{4\sigma_y^2}, \qquad c = \frac{\sin^2\theta}{2\sigma_x^2} + \frac{\cos^2\theta}{2\sigma_y^2}. \tag{3.5}$$

A is a normalisation factor, θ is the rotation angle, x and y are the projections on the S1 and S2 planes, respectively, and x_0 and y_0 are the mean S1 and S2 of the mono-energetic line. Examples of the fit for the lowest and highest energy lines used during the calibration are shown in figure 3.8. From the mean S1 and S2 values, the LY and QY are computed using the nominal energy for the given line. The calibration procedure also captures an additional z-position dependence of the detected signals, due to field non-uniformities, by dividing the analysis volume into five slices along the z-axis. The background events in the fiducial volume and the slices used for the z-dependence analysis are shown in figure 3.9 on the left. The calibration is performed independently in each slice. Exploiting the LY and QY anti-correlation at different energies it is possible to extrapolate the g_1 and g_2 parameters relative to the slice considered. Comparing the values obtained in all of them, a linear trend was observed. Because the parameters are detector only dependent, this was an indication of residual field non-uniformities, affecting also the electron mean free path correction[3]. A linear correction along the z-position is thus extrapolated and applied directly to the S1 and S2 definition, normalising the signals size to the value at the top of the TPC, where the electron mean free path correction is negligible. The calibration procedure was then repeated in the whole fiducial volume using the redefined S1 and S2 variables. The LY and QY computed for the different mono-energetic lines in the whole fiducial volume are shown in figure 3.9 on the right, for SS and MS events. Their linear fit

---

[3] Confirmed by studies on the mismatch of the electron mean free path computed with the $^{83\mathrm{m}}$Kr and ^{37}Ar calibration sources.

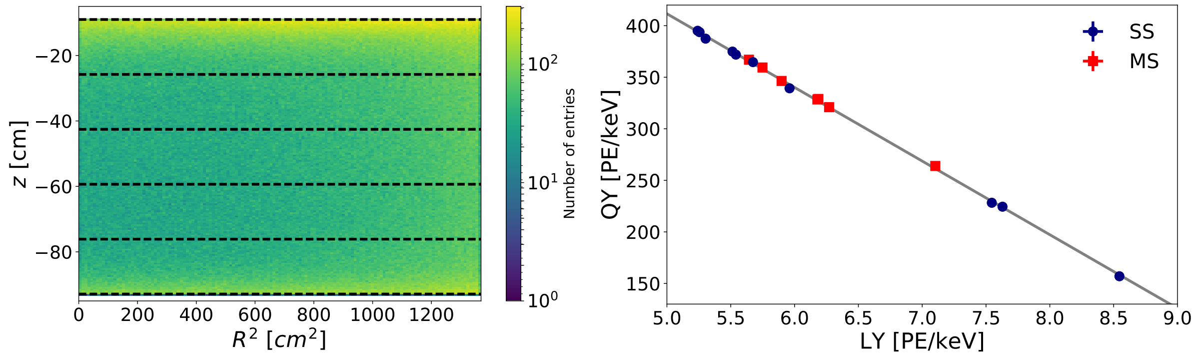

Figure 3.9: Left: background events in the inner cylindrical fiducial volume divided into five slices along the z-axis, delimited by the black dashed lines. Right: anti-correlation between the measured LY and QY using mono-energetic lines for SS (blue) and MS (red) events.

led to global g_1 and g_2 values of:

$$g_1 = (0.147 \pm 0.001)\,\text{PE/photon}\ , \tag{3.6}$$

$$g_2 = (10.53 \pm 0.04)\,\text{PE/electron}\ . \tag{3.7}$$

The excellent linearity of the response ensures that the calibration is applicable to events of a few keV up to a few MeV. For a given energy the MS data point is not at the same value of the SS one. Because of the different ion-electron recombination processes in LXe, the LY and QY produced by a single interaction are different from the sum of the LY and QY produced by multiple interactions detected at the same total energy.

The energy of each event is then reconstructed using equation 2.11. The spectra for SS and MS are shown in figure 3.10. The MS spectrum has a lower rate at low energies due to the inner fiducial volume selection. The region around $Q_{\beta\beta}$ for SS events is blinded for the $0\nu\beta\beta$ decay search. In the same region MS events show a double peak feature due to ^{214}Bi and ^{60}Co gamma lines at 2448 keV and 2505 keV, respectively. To extrapolate the energy resolution, the mono-energetic lines are fit with Gaussian functions above the background. The latter is modelled as a constant or linear function in a narrow energy range around the peaks. when the background is rapidly changing, an exponential function is added to the fit as well. An example is shown in figure 3.11. The energy resolution is then defined, from the fit parameters, as σ/μ where σ is the standard deviation and μ is the peak energy value. The data points are fit with the function in equation 3.2 with a and b

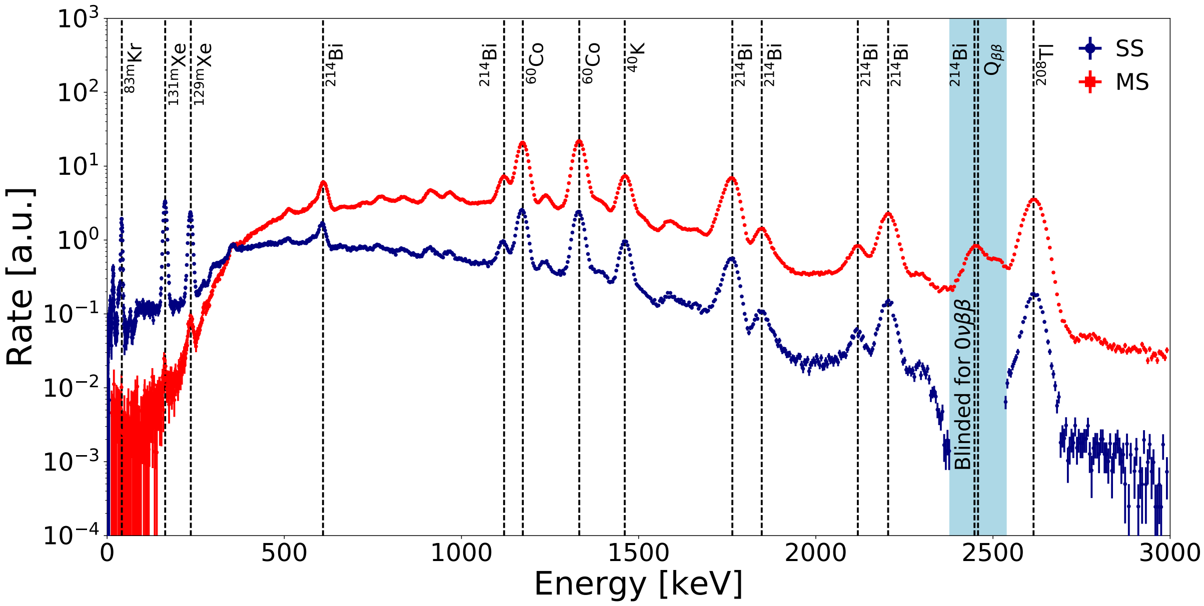

Figure 3.10: Single-site (blue) and multi-site (red) electronic recoil energy spectra of events in SR1, in the central 1 t cylindrical volume. SS events with energies around $Q_{\beta\beta}$ are blinded for the $0\nu\beta\beta$ decay search. The decaying isotopes corresponding to the most visible peaks are labelled with a dashed vertical line.

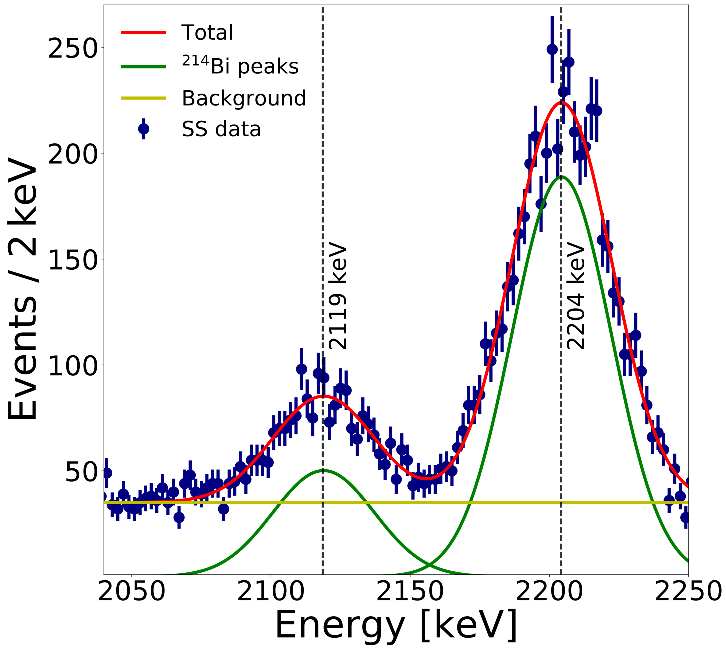

Figure 3.11: Fit on the ^{214}Bi peaks above 2 MeV, $\chi^2/\text{d.o.f} = 113.7/118$. The extracted value and standard deviation for the peak at higher energy are $\mu = 2204.4\,\text{keV}$ and $\sigma = 17.9\,\text{keV}$, respectively. The computed relative energy resolution is then $\sigma/\mu = 0.81\%$.

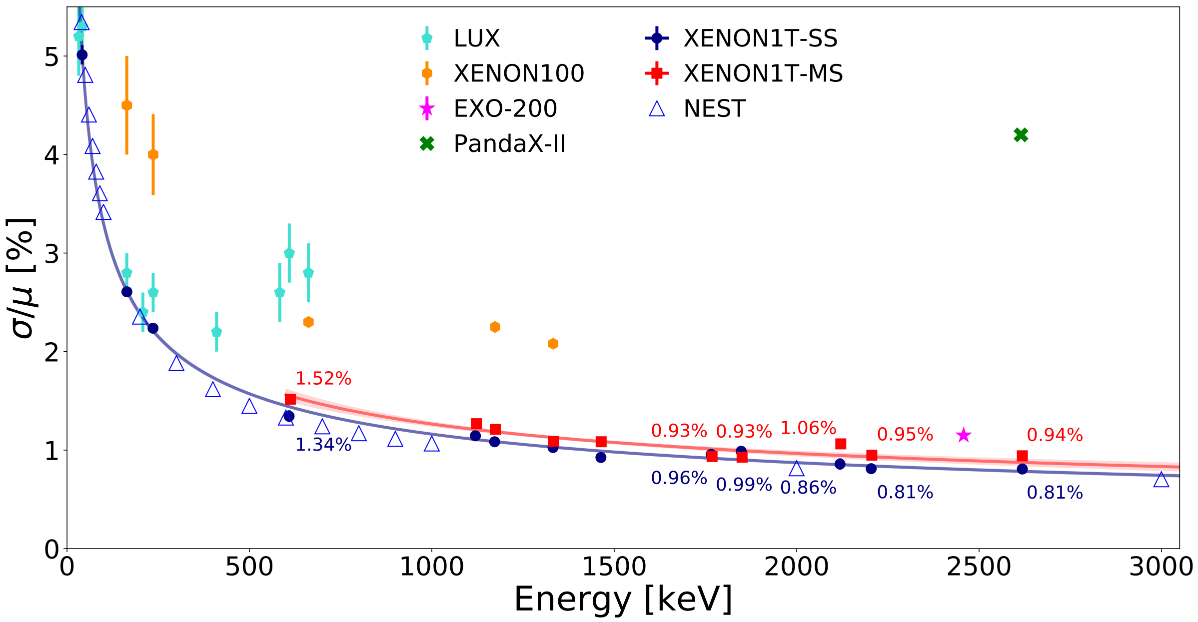

Figure 3.12: Measured relative energy resolution for SS and MS events. The SS and MS resolutions as a function of energy are fit with $a/\sqrt{E}+b$ and shown by the blue and red lines, respectively, while the shaded regions cover 1-σ statistical uncertainty of the fits. The resolution of LUX [134], XENON100 [135], EXO-200 [94] and PandaX-II [136] are also reported. The best energy resolution achievable by the XENON1T detector, computed with the NEST [137] framework, is shown by the empty blue triangles.

as free parameters. The extrapolated resolution functions for SS and MS events are:

$$\frac{\sigma(E)}{E}(\mathrm{SS})\,[\%] = \frac{(31.3 \pm 0.7)\,[\sqrt{\mathrm{keV}}]}{\sqrt{E\,[\mathrm{keV}]}} + (0.17 \pm 0.02) \tag{3.8}$$

$$\frac{\sigma(E)}{E}(\mathrm{MS})\,[\%] = \frac{(32.2 \pm 4.2)\,[\sqrt{\mathrm{keV}}]}{\sqrt{E\,[\mathrm{keV}]}} + (0.24 \pm 0.11) \tag{3.9}$$

The resolution for both SS and MS is shown in figure 3.12. The shaded regions, and the errors reported in equations 3.8 and 3.9, cover 1-σ statistical uncertainty of the fits. The shift of the peaks compared to their nominal value is within 0.4 % along the entire energy range. The relative energy resolution achieved in one-tonne fiducial mass at 2.46 MeV is (0.80±0.02) %. This value is better than the 4.2 % reported for the dual-phase LXe TPC of the PandaX-II experiment [136] and the energy resolution of LXe $0\nu\beta\beta$ dedicated experiments, such as the (1.15±0.02) % achieved in EXO-200 [94]. This value is very close to the best resolution limit of (0.77±0.04) %[4], predicted with the NEST [137] framework for a XENON1T-like detector, given the empirical values of g_1, g_2 from equations 3.6 and 3.7, and the drift field of 81 V/cm. The energy resolution is thus dominated by the

---

[4] The relative energy resolution and its error at 2.46 MeV are extrapolated from fitting the NEST data, in the same way as for the SR1 SS and MS values.

fluctuation in the scintillation and ionisation signals. The achieved relative resolution for MS events at 2.46 MeV is (0.90 ± 0.03)%. The slightly lower resolution from MS data with respect to SS data is due to limitations in the identification, reconstruction and corrections of both the S1 and S2.

3.3.2 Low Gain and Low Anode Tests

To validate the corrections at high energies, a few days of data with lower PMT gains and a few days with lower anode voltage were acquired. These conditions produce a smaller S2 size for a given interaction and allow us to compare the resolution between these datasets and the ones with higher S2 size. The data were acquired after the end of SR1, during the last months before the decommissioning of XENON1T (science-run2 or SR2). This period was used to perform a few tests useful for the upcoming XENONnT experiment and thus the detector was not operated in stable conditions. The results obtained with these data are not to be considered demonstrative of the absolute detector performance but only relative to the values obtained from the data acquired during the same period and with the high-energy reconstruction techniques applied.

The lower gain datasets were acquired biasing the PMTs at a voltage such as to have a factor 10 less gain. The lower anode voltage datasets were acquired at $-2.5\,\mathrm{kV}$ instead of $-4\,\mathrm{kV}$, this reduces the S2 secondary scintillation gain and thus the S2 size. The neutron generator was used for both tests to have more statistics at the 2.2 MeV γ-line from the binding energy of neutrons capture on protons. The resolution of the high-energy 2.2 MeV line for the low gain data is $(1.26 \pm 0.02)\,\%$, worse than the resolution of SR1 at the same energy. Similarly the resolution for data at low anode voltage on this peak is $(1.27 \pm 0.15)\,\%$. However, the resolution computed on $\sim$55 days of background during the same period is $(1.21 \pm 0.09)\,\%$, in agreement with the resolution obtained for the low-gain and low anode voltage data. These results are shown in figure 3.13. This is an indication that there is no degradation in the reconstructed signals compared to the datasets with reduced S2 size, and thus the saturation is properly corrected.

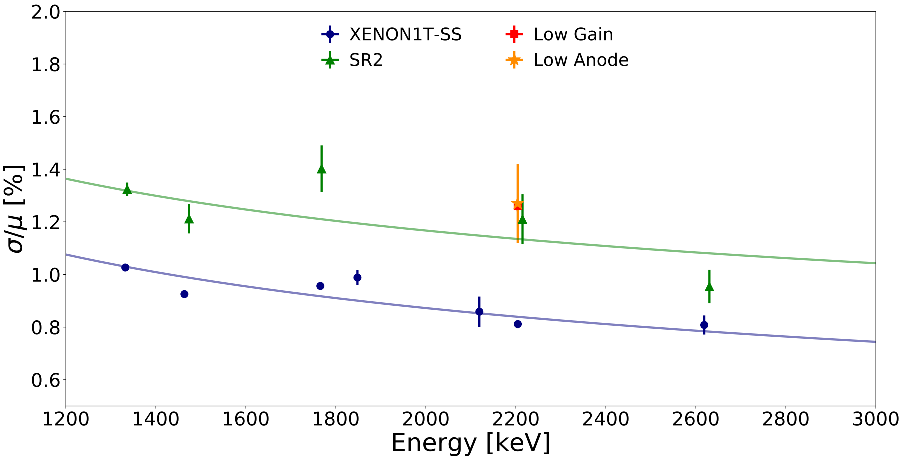

Figure 3.13: Measured relative energy resolution for SS events during SR2 tests. The value obtained at 2.2 MeV for the low gain (red) and low anode (orange) data is in agreement with the overall SR2 energy resolution (green). The result obtained during SR1 (blue) is shown for reference.

3.4 Outlook

The aim of this study is to prove the possibility to perform a simultaneous WIMP and $0\nu\beta\beta$ search with xenon dual-phase TPCs. As shown in sections 1.4 and 1.5 there are many factors that must be considered to achieve this goal. Here the focus is on the detector linearity and signal reconstruction capability.

Starting from the signal reconstruction developed for the WIMP-nucleus scattering analysis with XENON1T, the work was successful in extending the linearity of the detector response to the MeV region in the energy range of the ^{136}Xe neutrinoless double beta decay. The main problems affecting the signal at high energies are the non-linearity and distortions due to saturation. This is mainly caused by the digitisers. Single electrons and afterpulses can also cause artefacts in the tail of the signal. A saturation correction method was implemented to reconstruct the affected signals. The clustering algorithm was refined to recognise more variations in the shape of the waveform, in particular local minima that can occur in case of multi-site events close in time or secondary signals following the main one. The effect of the improvements is observed in the reconstructed energy resolution. A world-record relative energy resolution in liquid xenon of $\sigma/\mu = (0.80\pm0.02)\,\%$ at 2.46 MeV is achieved in XENON1T. This value is in agreement with the NEST prediction of $(0.77\pm0.04)\,\%$ for the fundamental resolution in LXe at the working condition of the detector.

For the XENONnT experiment, currently under commissioning, we installed low amplification channels in the readout specific for the high energy analyses. This will allow us to understand if further improvements are possible on the reconstruction technique. To maintain an excellent resolution the fluctuations in the scintillation and ionisation channels must be reduced as much as possible. A long, mean-drift length of the ionised electrons is fundamental and it can be ensured by a 200 V/cm high drift field and a cryogenic LXe purification system with high circulation speed of 5 L/min, in addition to the 120 SLPM recirculation in gas. A reduction of the fluctuation in the scintillation signals could be achieved by a higher light collection efficiency provided by a larger photosensor coverage and higher quantum efficiency.

CHAPTER 4

Neutrinoless Double Beta Decay Search in XENON1T

XENON1T was designed to be a DM detector but, because of its large mass and excellent relative energy resolution in the MeV range, it can be exploited to search for $0\nu\beta\beta$ decay. However, the materials employed were not selected to minimise the background around the $Q_{\beta\beta}$ of ^{136}Xe. Specifically, a gamma line from ^{214}Bi from materials is expected to contribute significantly to the background in the ROI. Moreover the experiment exploits natural xenon whose ^{136}Xe abundance is an order of magnitude lower than the enriched one of the $0\nu\beta\beta$ decay dedicated experiments. Thus this analysis in XENON1T is not expected to be competitive with dedicated searches. Neither in XENONnT the materials are selected for this search. Thanks to the larger xenon mass and the reduced background, XENONnT can still reach a sensitivity comparable with the current most sensitive detectors, such as EXO-200 [94] and KamLAND-Zen [98]. However, this analysis can serve as proof of concept for the next generation dual-phase TPC experiments. Using as baseline goal the energy resolution achieved with the work described in chapter 3 and improving the selection of some materials, the DARWIN experiment can reach a sensitivity on the order of 10^{27} years on the decay half-life [100] and be competitive with the next generation of dedicated experiments, such as nEXO [96].

In this chapter the high level analysis for the $0\nu\beta\beta$ decay search with XENON1T data is described. The blind analysis is still ongoing and thus in this thesis only the results achieved to date are shown. In particular, the data selection, efficiency estimation and the choice of the analysis fiducial volume are presented in section 4.1. In section 4.2 the main background components affecting the ROI and the result of the Monte Carlo fit to the data are shown. Finally, an outlook on the empirical sensitivity expected for XENON1T and XENONnT is reported in section 4.3. This analysis is performed by several members within the XENON collaboration. In particular, I am one of the conveners of the analysis channel and I worked directly on the data aspects and the data-driven input for the background model fit to the data.

4.1 Data Selection and Efficiency

In building this analysis, data selection criteria were developed with the goal of having high acceptance of potential signal or signal-like interactions and rejecting sources of background. As pointed out in section 3.3, the majority of the expected $0\nu\beta\beta$ signal detected by XENON1T is an electronic recoil single scatter interaction. The event selections developed and applied for this analysis are listed in table 4.1, these consist of three main types of cuts. The first type is placed due to the readout and detector data quality checks, including instability of the DAQ or to reject PMT internal light emissions. Requirements on the number of coincident PMTs detecting light and threshold on the S2 signal size are used to select physical signals with full detection efficiency. A second type of cuts is developed based on the signal reconstruction, for example comparing the reconstructed position using different algorithms or removing events with unusual patterns or distributions on the PMT arrays. Finally, the third type of cuts is based on the properties of the S1 and S2 signals travelling in LXe. Such selections are used to reject multi-site interactions, discriminate between ER and NR events and select S2s whose shapes are compatible with the expected diffusion model of electrons drifting in the TPC [138]. Among these selections I worked on developing two of them, the *PosDiff* and the *S2Width* cuts.

***PosDiff*:** This cut aims at rejecting events that are reconstructed in different x-y positions according to two algorithms, the neural network tensor flow (NN_TF) [132] and the *top pattern fit* (TPF) [113]. The variable on which the selection is built is $D(x, y)$:

$$D(x,y) \equiv \sqrt{(x^{\mathrm{NN\_TF}}_{\mathrm{observed}} - x^{\mathrm{TPF}}_{\mathrm{observed}})^2 + (y^{\mathrm{NN\_TF}}_{\mathrm{observed}} - y^{\mathrm{TPF}}_{\mathrm{observed}})^2} \tag{4.1}$$

where $x(y)^{\mathrm{NN\_TF}}_{\mathrm{observed}}$ is the $x(y)$ observed coordinate reconstructed using the NN_TF algorithm and $x(y)^{\mathrm{TPF}}_{\mathrm{observed}}$ using the TPF. The defined variable is expected to be about zero for well reconstructed events. For low-energy events, $\mathcal{O}$(keV), the position reconstruction has a less defined S2 pattern on the top PMT array and thus the distribution is wider. The cut is defined on the $D(x, y)$ distribution against the S2 signal size. The distribution is binned and the upper 99.5 % quantile of the population in the bin is chosen. The quantiles are then fit with an exponential function. To define the cut in the MeV energy region, lacking available calibration sources at this energy, background data are used, excluding

Table 4.1: List of event selections used for the $0\nu\beta\beta$ decay search with their brief description. The three blocks show the grouping of the main types of cuts: based on the readout or detector data quality checks, on the signal reconstruction and the properties of the S1 and S2 signals travelling in LXe.

Selection	**Description**
DAQVeto	Makes sure no DAQ vetoes happen during an event.
Flash	Removes a time-window around a flash.
MuonVeto	Removes events in coincidence with muon veto triggers or when the muon veto is off.
S1PMT3fold	Rejects events in which, for the main S1, the number of contributing PMTs is lower than 3.
S2Threshold	Lower threshold on the S2 size at which the trigger is perfectly efficient.
PosDiff	Removes events with large position reconstruction difference between *TensorFlow* and *TopPatternFit* algorithms.
CS2AreaFractionTop	Removes events with an unusual fraction of the cS2 area on the top PMT array, primarily gas events.
S1AreaFractionTop	Check the dependence of the S1 area fraction on the top PMT array along the depth of the interaction.
S2PatternLikelihood	remove poorly reconstructed S2 and multiple scatter by using the likelihood of the S2 pattern.
S2SingleScatter	Remove events with a second S2 real scatter.
S1SingleScatter	Remove events with a second S1 real scatter between the main S1 and the main S2.
S2Width	Remove events that do not follow the S2 diffusion model.
ERband	Remove events whose S2/S1 ratio is not compatible with the one of ER interactions.

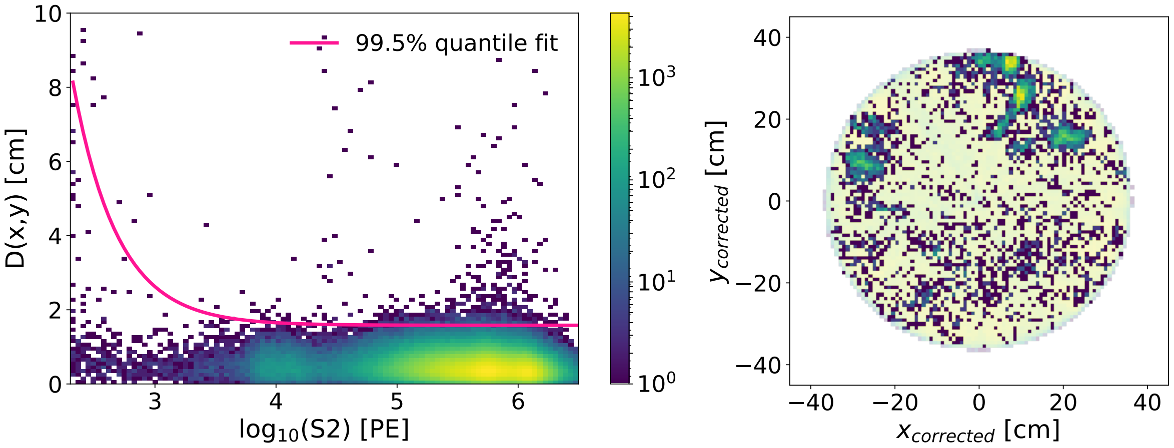

Figure 4.1: Left: background events in the *PosDiff* cut parameter space with the definition on the 99.5% quantiles fit (magenta line). Right: events removed by the *PosDiff* cut (bright) and total SR1 background events (shaded) for SS interactions. The events removed by the cut are localised where malfunctioning PMTs were off during the data taking.

the blinded analysis region. The latter is defined as $\pm4\sigma$ around the $Q_{\beta\beta}$, between 2379 keV and 2537 keV, with the relative energy resolution σ/E=0.8% as found in 3.3. The resulting cut is shown on the left of figure 4.1, and it is defined as:

$$D(x,y) < 3569.674 \times \exp\left(-\frac{\log_{10}(S2)}{0.369}\right) + 1.582 \tag{4.2}$$

On the right of figure 4.1 the events removed by the cut in the x-y plane are shown. Two populations are visible, corresponding to the regions where most of the malfunctioning PMTs excluded from the analysis during SR1 were located[1]. As the reconstruction is performed with the top PMT array, it is expected that where the PMTs in this array are off, the reconstruction performance is worse. In these regions the rejected events are around 3% or 4% of the total, while in the fiducial volume described in section 4.1.1 an average of 0.52% events are removed.

***S2Width*:** This cut rejects events whose S2 signal width is not compatible with the expectation from the simulated signal model. The latter can predict the width of an S2 signal based on the depth of the interaction inside the detector. Three components contribute to the total S2 signal width, the single electron waveform, σ_{e}, the diffusion of electron clouds along the drift region, σ_{D}, and the track length effects, σ_{T}. The total S2

---

[1] PMTs turned off: 1, 2, 12, 26, 34, 62, 65, 79, 86, 88, 102, 118 in the top array and 130, 134, 135, 139, 148, 150, 152, 162, 178, 183, 190, 198, 206, 213, 214, 234, 239, 244 in the bottom array.
PMTs with low SPE: 27, 73, 91 in the top array and 137, 167, 203 in the bottom array.

width σ is then defined as:

$$\sigma^2 = \sigma_{\mathrm{e}}^2 + \sigma_{\mathrm{D}}^2 + \sigma_{\mathrm{T}}^2 \tag{4.3}$$

This spread of the electron cloud determines the intrinsic limit to the position resolution of a LXe detector. Moreover, the shape of the S2 signal is affected by the longitudinal diffusion. For electron clouds travelling in LXe this is given by [138]:

$$\sigma_D = \frac{\sqrt{2Dt}}{v_d} \tag{4.4}$$

where D is the longitudinal diffusion constant, t is the mean drift time and v_d is the electron drift velocity. In XENON1T the S2 width is defined at the 50% of the signal area (r_{50}), between the 25% and 75% of its collected charge. This is related to the Gaussian standard deviation as $r_{50} = 1.349\,\sigma$. Thus the terms from the single electron width and the electron clouds diffusion can be rewritten as:

$$r_{50} = \sqrt{\frac{3.64Dt}{v_d^2} + w^2} \tag{4.5}$$

where $w^2 = 1.82\,\sigma_{\mathrm{e}}^2$. For SR1, at a drift field of 81 V/cm, the electron drift velocity was estimated, from the maximum electron drift time and the measured drift length, to be $v_d = (1.335 \pm 0.002)\,\mu\mathrm{m/ns}$. The r_{50} distribution was fit along the interaction depth and the extrapolated value for the longitudinal diffusion constant was $D = (29.35 \pm 0.05)\,\mathrm{cm^2/s}$. The S2 width ranges from the single electron width of $\sigma_{\mathrm{e}} \approx 230\,\mathrm{ns}$ to about $2\,\mu\mathrm{s}$ at the bottom of the active volume. Thus, for interactions deeper than ~10 cm, the electron cloud diffusion is the dominant component of the S2 signal width.

During the WIMP analysis, the track length contribution was considered negligible and not taken into account in the S2 width model but, for interactions of order an MeV, this effect cannot be neglected. In figure 4.2 on the left the stopping power computed with the ESTAR program [139] is shown. It is possible to define a new element, *LiquidXenon*, with a density of $2.86\,\mathrm{g/cm^3}$ at a temperature of −96 °C and a pressure of 1.935 bar. The track length, x, is then calculated from the stopping power, $S(E)$, as:

$$x = \int_0^{E_0} \frac{1}{S(E)} dE \tag{4.6}$$

where E_0 is the initial energy of the interacting particle. The computed track length is shown on the right side of figure 4.2. For energies $\mathcal{O}\,(1\,\mathrm{MeV})$, the track length is indeed comparable with the S2 model from the diffusion of the electron clouds. However, only

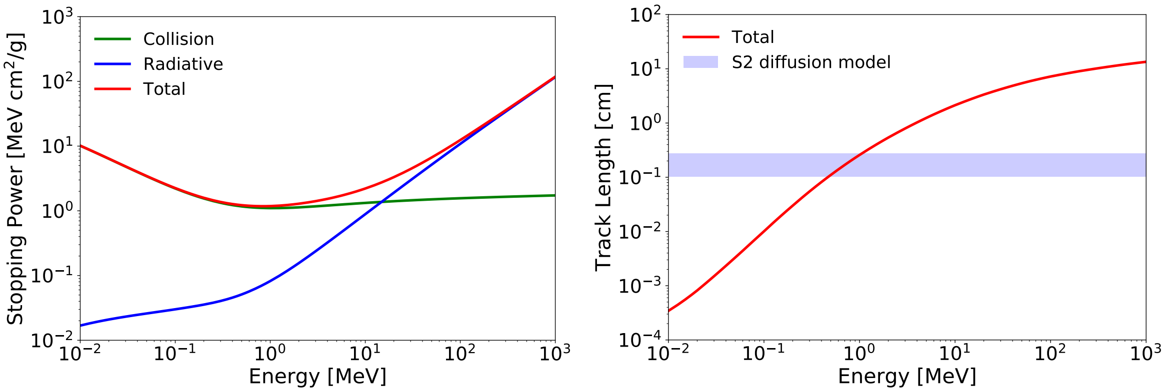

Figure 4.2: Left: stopping power for electrons in LXe. The radiative and collision components are also shown. Data from ESTAR [139]. Right: track length computed from the total stopping power showed on the left. The range of S2 width from the diffusion model computed in XENON1T during SR1 is shown for comparison.

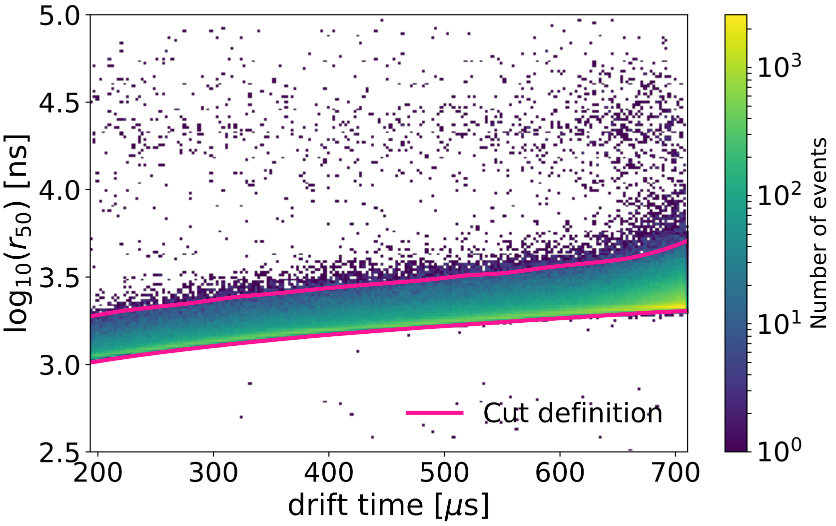

Figure 4.3: *S2Width* cut definition (magenta) extended to high energies. SR1 background data in the fiducial volume for the $0\nu\beta\beta$ decay search are overlapped for reference.

the longitudinal component of the track length affects the S2 width. Because this latter cannot be modelled for every interaction, the cut at high energies cannot be defined in the same way as done at a few keV. The cut was then defined, from background data, by the 1% and 99% quantiles of the r_{50} distribution along the drift time. A cubic spline[2] was used to interpolate the quantiles. The cut definition is shown in figure 4.3, along with SR1 data in the defined fiducial volume for the $0\nu\beta\beta$ decay search (see section 4.1.1). To have a unique definition in the whole energy range, the final *S2Width* cut is designed to follow the diffusion model below 250 keV, as defined during the DM analysis campaign, and to be delimited by the quantiles above it.

---

[2] Function defined piece-wise by cubic polynomials.

4.1.1 Fiducial Volume

The selection of a fiducial volume has a considerable effect on the expected sensitivity. As shown in equation 1.42, it affects the source mass and the background rate within it. To optimise the choice of the fiducial volume, a figure of merit (FoM) proportional to the experimental sensitivity is used:

$$\mathrm{FoM} = \frac{m}{\sqrt{N}} \tag{4.7}$$

where m is the total LXe mass and N the number of background events within a volume. SR1 background data are used for this study. The selections listed in table 4.1 are applied. An additional energy selection to restrict the optimisation close to the $Q_{\beta\beta}$ is applied. Because the analysis is blinded, sideband regions are used. The energy range consists of $\pm 4\sigma$ around the ^{214}Bi peak at 2204 keV and $\pm 4\sigma$ around the ^{208}Tl at 2614 keV, with the relative energy resolution σ/E=0.8% as found in 3.3. These regions are shown in figure 4.4 in orange. ^{214}Bi is the dominant background expected in the blinded region due to a peak at 2447.9 keV, which is only ∼10 keV from the $Q_{\beta\beta}$. To define a volume without using a predefined shape, the following procedure is adopted:

1. Bin the TPC active volume in the (R^2, z) parameter space, where $R^2 = x^2 + y^2$, as shown on the left of figure 4.5.
2. In each bin, compute the FoM as defined in equation 4.7.
3. From the FoM distribution obtained, select contours of equivalent FoM and fit them with similar shape functions. The FoM distribution with some contours as an example are shown in figure 4.5 on the right.

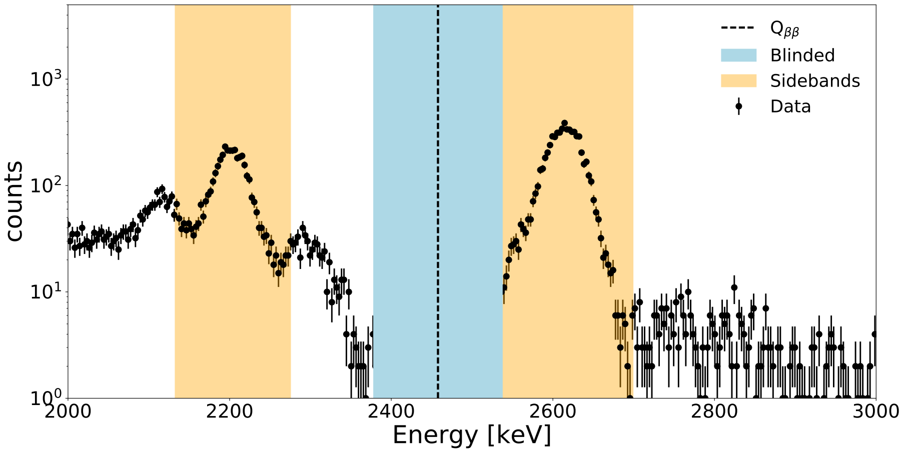

Figure 4.4: Blinded (light-blue) and sidebands (orange) regions overlapped to SR1 data prior fiducial volume selection (black datapoints). The $Q_{\beta\beta}$ is also shown.

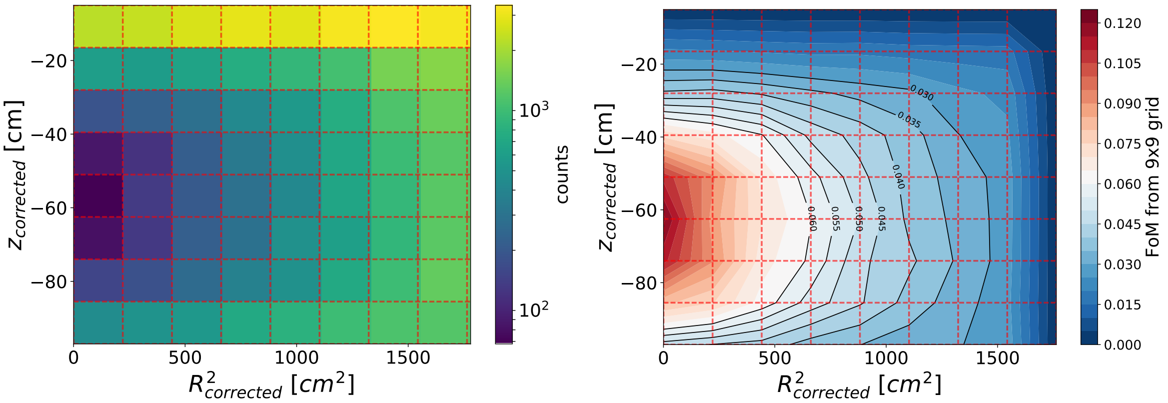

Figure 4.5: Left: Background distribution, from the ^{214}Bi peak at 2204 keV and the ^{208}Tl at 2614 keV, in the TPC active volume on the (R^2, z) parameter space, binned in a 9×9 grid. Right: FoM distribution with the grid (dashed red) and some contours (black) overlaid.

4. In each volume defined by the fit on the equivalent FoM in the bin, compute a new FoM over the whole volume.

5. Select as optimum fiducial volume the one that maximises the new FoM computed on the entire volumes.

The TPC active volume was binned in a 9×9 grid to have at least 50 events on average in each bin. Increasing the number of bins would reduce the statistics in each of them and increase statistical fluctuations. As shown in 4.5 on the right, the FoM distribution is not symmetric but it is shifted towards the bottom due to a higher material background contribution. To select a shape that can be used as fiducial volume the contours of equal FoM have been fit with:

- A semi-superellipsoid from the top;
- A semi-superellipsoid from the bottom, with the constraint to flatten if the curve goes below -94 cm. Below this value the field distortion is not properly corrected and therefore it is excluded from the analysis.

Having two different functions allows one to define an asymmetric volume and optimise the two halves independently to expand the volume as much as possible.

The fiducial mass of the shape selected between the two semi-superellipsoids is computed with different methods. The volume can be estimated numerically by integrating between the functions that define it while the mass can be calculated using the LXe density, ρ=2.86 g/cm^3:

$$M = \rho\pi\int_0^{R^2_{max}}[f_{up}(x) - f_{low}(x)]\mathrm{d}x \tag{4.8}$$

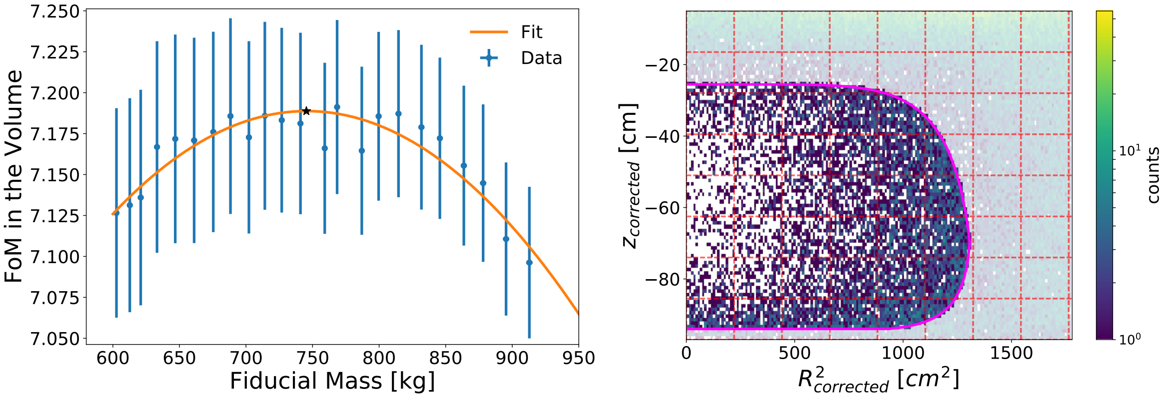

Figure 4.6: Left: trend of the FoM within the volumes defined by the semi-superellipsoids (blue datapoints) and their fit with a parabolic function (orange). The error on each datapoint is propagated considering the error on the fiducial mass and the statistical error on the number of events in the volume. The maximum of the parabola is indicated by a black star. Right: distribution of the background in the sideband regions within (bright) and outside (shaded) the fiducial volume (magenta line).

where $f_{up}(x)$ and $f_{low}(x)$ are the two fit functions from the top and bottom, respectively. Another method exploits events uniformly distributed in the TPC. The fiducial mass can be computed as the ratio between the events inside the selected volume and the total number of events. A total of 10^7 events were simulated randomly distributed and the ratio of events was scaled according to the total LXe target mass, $M_{tot} = (2003.8 \pm 5.2)$ kg. The difference found between the two methods is used as systematic error in the evaluation of the final fiducial mass.

In figure 4.6 the FoM computed in the volumes defined by the fit functions are shown with the respective masses. The fiducial mass increases linearly enlarging the volume while the background increases exponentially towards the walls of the TPC, due to the self-shielding property of LXe. For this reason the datapoints follow a parabolic trend where the maximum is the point when the background starts to be dominant in the FoM. Thus the distribution is fit with a parabolic function. The maximum of the parabola is at 745 kg. The fiducial volume is chosen to be the corresponding volume of the datapoint before the maximum, as a more conservative approach on the background level. The final fiducial mass is $(741.0 \pm 1.0 \pm 1.2 \pm 7.1)$ kg. The error is computed considering three main contributions: the propagation of the errors on the two methods used to compute the mass, the error given by the semi-difference of the two methods and the average semi-interval between the datapoints considered for the study. For a measured ^{136}Xe abundance of $(8.49 \pm 0.04(stat) \pm 0.13(sys))\%$ in XENON1T, the fiducial mass of ^{136}Xe is (62.9 ± 2.0) kg.

With this study the fiducial volume of the analysis is fixed. Having a position dependent likelihood would be optimal but it would require a wider effort to study the position distributions of the background components in the MeV energy region and their uncertainties. Given that this study is a proof of concept and that we do not expect XENON1T to be competitive with the current leading experiments, we opted for this conservative choice. However, it can be taken into consideration for XENONnT and the next-generation experiments.

4.1.2 Total Acceptance

To estimate the overall signal acceptance due to the data selection criteria, different methods are used:

- Analytic: the acceptance is known analytically from the cut definition or through simulations. It is set to unity when it can be treated as a livetime correction.
- Iterative: the acceptance is computed from the number of events before and after applying the selection. It partly accounts for correlations between cuts by closely following a cut list and applying iteratively all the cuts listed before the cut being analysed.

All cuts based on the detector quality checks are considered with unity acceptance because they reduce the livetime of the data. The fiducial volume is a geometrical cut, it reduces the exposure but does not select or reject specific events and is considered with unity acceptance. The *S2SingleScatter* is defined with a machine learning approach and is tuned to have unity acceptance in the MeV energy region. The *S1SingleScatter* is defined analytically with an acceptance of 97.5% using simulated signal events. The *ERband* is defined between the 1 and 99% quantiles of the $\log_{10}(cS2_b/cS1)$ along the reconstructed energy. The cut is defined iteratively using data from the top half part of the TPC as the bottom part is affected by *gamma-X* (events which also produced a scatter below the cathode) that distort the shape of the band. Its acceptance is then applied analytically to the whole fiducial volume. For the remaining cuts, the acceptance is computed with the iterative method. To consider the correlation between the cuts, an order is established and at each step all the previous selections are applied, so that an event is not rejected twice and the acceptance is not underestimated. This method provides a lower limit on the acceptance because all the rejected events are considered in the iterative method and not only the signal-like ones. Therefore the final acceptance of the signal stands between this lower limit and the overall analytic acceptance, fixed at 97.5%. The total acceptance along the reconstructed energy is shown in figure 4.7. In the ROI it is between 87% and 91%.

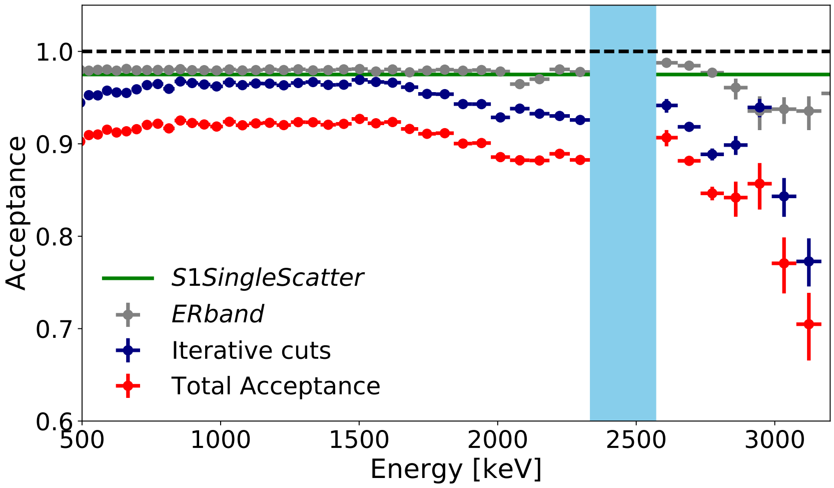

Figure 4.7: Total acceptance (red) for the $0\nu\beta\beta$ decay selections. The *S1SingleScatter* (green) and the *ERband* (grey) acceptances are also shown, together with the combined acceptance from the cuts for which the iterative method was used.

4.2 Background Model

The background model for the $0\nu\beta\beta$ decay search is estimated by fitting the energy spectrum of the measured and selected data with the sum of all the Monte Carlo simulated background components. The procedure is the following:

1. Data are selected through quality checks, cuts and fiducial volume, as described in section 4.1.

2. The energy calibration and reconstruction of the spectrum is applied, as shown in section 3.3. The selected energy spectrum is the first input for the fitting procedure.

3. The relevant background sources are simulated with GEANT4[3]. The desired variables are then processed through *nSort*, a tool developed by the collaboration to cluster the energy depositions according to the detector position resolution.

4. To match the data, single scatter and fiducial volume selections are applied to the simulations. The energy spectra of each component are also smeared according to the same resolution function derived from the data calibration.

5. The data selection acceptance as computed in section 4.1.2 is used as input during the fitting to scale the simulated total spectrum accordingly.

---

[3] The simulations are performed with GEANT4 version 4.9. Some isotopes were updated with version 4.10 if the upgrade fixed some specific *bugs*, as the case for ^{214}Pb.

6. A likelihood fit is performed to match the data energy spectrum with the background model. Constraints from the material screening and concentration, half-lives and abundances of radioactive isotopes and uncertainties are used to reduce the free parameters in the fit to 12.

The *MoMa* framework, developed for XENON1T [140], is used to collect all the inputs and perform the likelihood fit to obtain the background model.

Intrinsic Background: The background sources can be classified as intrinsic, decaying directly in the LXe, and external, coming from materials. In the region of interest for the ^{136}Xe $0\nu\beta\beta$ decay there are two dominant intrinsic components, the $2\nu\beta\beta$ of ^{136}Xe itself and the ^{214}Bi-decay from the ^{222}Rn chain.

The ^{136}Xe spectrum was simulated based on the theoretical calculations from Kotila and Iachello [77]. Shape uncertainties arising from the single-state dominance (SSD) or higher-state dominance (HSD) decay mechanisms are not considered because its impact is lower for the summed spectrum of the two electrons compared to the single electron spectra and this background is more than 4 orders of magnitude lower than the material background in the ROI. The spectrum is normalised according to the expected decay rate:

$$-\frac{\mathrm{d}N}{\mathrm{d}t} = \lambda N = \frac{\ln(2)}{T^{2\nu}_{1/2}} \frac{N_A \alpha}{M} \tag{4.9}$$

with $T^{2\nu}_{1/2} = (2.165 \pm 0.016(stat) \pm 0.056(sys)) \times 10^{21}$ yr from EX0-200 [141] and $\alpha = (8.49 \pm 0.04(stat) \pm 0.13(sys)) \times 10^{-2}$ isotopic abundance of ^{136}Xe measured in XENON1T. N_A and M are the Avogadro's number and the xenon molar mass, respectively.

^{214}Bi β-decays into ^{214}Po with a half-life of 19.8 minutes and then ^{214}Po decays through an α emission into ^{210}Pb with a half-life of 162.3 μs. Thanks to the short half-life of these decays, the ^{214}Bi decaying into the active volume of the TPC can be tagged and rejected. This component is left free to vary and fixed during the fitting procedure. The resulting rate of ~1.5 μBq/kg suggests a tagging efficiency of ~85%. The decays happening in the shell, or outer region, cannot be tagged and the activity of ^{214}Bi in this region is about 10 μBq/kg. This component produces several γ-peaks, among which the already mentioned peak at 2447.9 keV in the ROI. Two additional backgrounds stem from ^{137}Xe, produced through muon induced neutron capture on ^{136}Xe, and ^{8}B solar neutrinos which can produce background due to elastic scattering on electrons. Both sources are estimated to be negligible compared to the material background and thus not considered. The spectra of the simulated, normalised, intrinsic components are shown in figure 4.8.

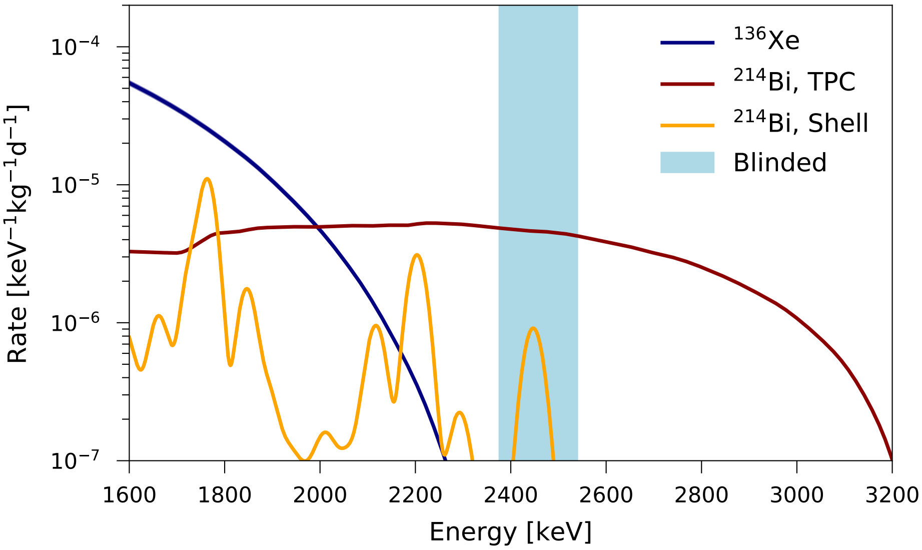

Figure 4.8: Simulated intrinsic background components between 1600 keV and 3200 keV.

Background from Materials: The materials background comes from the detector components. The main contributions come from the stainless steel of the cryostat, copper and PTFE of the field cage and the PMT arrays, and the PMTs and bases themselves. The ^{238}U chain was split at the ^{226}Ra-decay and the two parts were simulated separately to account for disequilibrium. It was not possible to do the same for the ^{232}Th decay chain because this caused the underestimation of ^{228}Ac, so this chain was fully simulated. The chain was simulated also starting from ^{228}Th and then part of it was added or subtracted to the ^{232}Th to adjust for the disequilibrium. ^{60}Co was also simulated, with a peak in the ROI at 2505.7 keV originating from the sum of the 1173.2 keV and 1332.5 keV peaks. The number of free parameters in the background model was constrained for each isotope using their relative abundance in different materials as measured from screening results. In this way each isotope contributes a single free parameter.

To normalise the spectra of each isotope, the counts in each bin, n_i, are scaled according to the number of simulated events, N_S, the component mass, M_C and for the number of steps in the simulated decay chain, n_s.

$$R_i = \frac{n_i \cdot M_C \cdot n_s}{N_S} \cdot \frac{t}{\Delta E \cdot M_{\mathrm{FV}}} \tag{4.10}$$

where R_i is the rate computed in each bin i, for a livetime t in a fiducial mass M_{FV} and for an energy resolution ΔE in units of energy. The spectra from the material background are shown in figure 4.9.

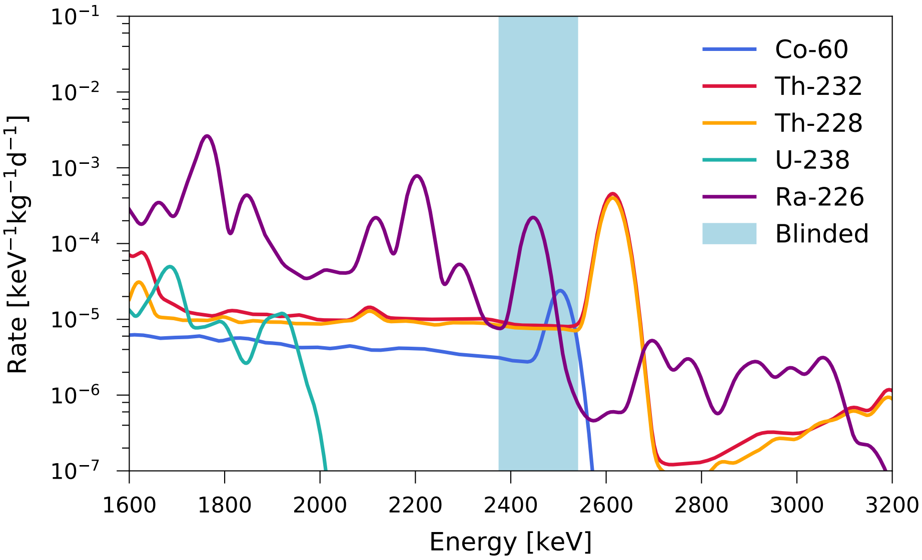

Figure 4.9: Simulated material background by isotopes, summed and normalised over the different materials, between 1600 keV and 3200 keV.

Following the first fitting attempts, it was noticed that at the beginning of the SR1, after neutron calibrations, the neutron generator (NG) was left in the water tank. Even if it was turned off, the radioactive background coming from the NG materials themselves caused an increase in rate within the FV. Because there are no screening measurements, it is not possible to model this background. Thus 44.5 days of SR1, corresponding to the period in which the NG was in the water tank, needed to be removed from the analysis. A total of 202.7 days are then used for the analysis.

During the fitting procedure the selections' acceptance is used as a scaling factor. The file with the computed acceptance in each energy bin provides a lower limit, so the fit is free to scale between this lower limit and the maximum analytic acceptance. The uncertainty on the fiducial volume is also added as a scaling parameter. Following the energy reconstruction and calibration in chapter 3, the energy shift of the peaks is within 0.4%. To correct for this uncertainty, during the fitting a further energy dependent peak shift plus constant parameters are added. A binned negative log-likelihood minimisation is used for the fit, with the MIGRAD minimiser as implemented in the iMinuit Python package. The fit is performed on a 2 keV binning between 1600 keV and 3200 keV. The region between 2300 keV and 2600 keV was excluded, slightly larger than the blinded region, to avoid eventual mismatch caused by the edges of the blinded region. The result is shown in figure 4.10. The acceptance is set to the lower limit and the added energy dependent peak shift parameters push the energy resolution from 0.8% to 0.9% at $Q_{\beta\beta}$. All parameters, i.e the isotopes normalisation, the scaling of the acceptance and the energy

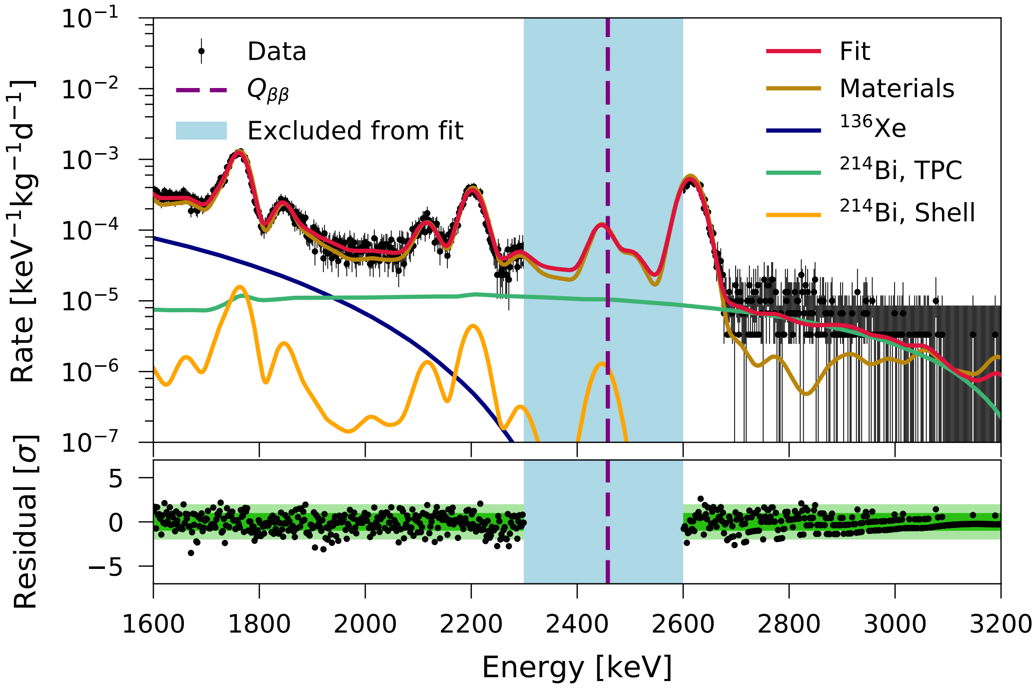

Figure 4.10: Data (black) and matching fit (red) between 1600 keV and 3200 keV. The background from materials (gold) and the intrinsics from ^{136}Xe (blue) and ^{214}Bi inside the active volume of the TPC (green) and in the shell (orange) are also displayed. In the bottom panel the residuals with the 1σ and 2σ bands are shown.

shift, match expectations within 2σ.

4.3 Preliminary Results and Outlook

This analysis is performed as a proof of concept for dual-phase TPCs. It opens the path for the next generation experiments, XENONnT and DARWIN, to be competitive with $0\nu\beta\beta$-search dedicated detectors. This is possible thanks to the extensive work conducted on the high energy signal reconstruction, that covers also the region of interest of the decay.

At the time this thesis is being written, the analysis is still ongoing. In particular, the results are preliminary and the framework for the statistical inference is under construction. The unblinding and final results will follow. Up to date an extensive work has been conducted on the data quality and selection in the MeV energy range, as well as on the background model. The expected sensitivity can be computed empirically using equation

Table 4.2: Values used to compute the empirical sensitivity to the $0\nu\beta\beta$ decay in XENON1T, XENONnT and DARWIN [100].

Experiment	**Fiducial Mass** [kg]	**livetime** [yr]	**Background Rate** [$\mathbf{keV^{-1}\ t^{-1}\ yr^{-1}}$]	$\mathbf{S^{0\nu}}$ [yr]
XENON1T	741	0.56	35	2.3×10^{24}
XENONnT	1136.5	5	3	3.0×10^{25}
DARWIN	5000	10	3.96×10^{-3}	2.4×10^{27}

1.42, reported here for completeness of the section:

$$S^{0\nu} = \ln(2)\varepsilon\frac{\alpha N_{\mathrm{A}}}{A}\sqrt{\frac{M\cdot t}{\Delta E\cdot b}} \tag{1.42}$$

In particular, an efficiency $\varepsilon = 0.9$ is considered. For the isotopic abundance, the measured value of $\alpha = 8.49\times10^{-2}$ is used (see section 4.2). The ROI is defined as one full width at half maximum (FWHM):

$$\Delta E = \mathrm{FWHM} = 2.355\times\sigma = 2.355\times0.008\times2457.83\,\mathrm{keV} = 46.3\,\mathrm{keV} \tag{4.11}$$

Considering an average background rate in 1 FWHM, the values obtained for XENON1T during this work, and for XENONnT within an ongoing study[4], are reported in table 4.2. The values from the DARWIN projections described in [100] are also reported in the table. In figure 4.11 the 90% CL empirical sensitivity is shown. The latest results on the sensitivity from EXO-200 [94] and KamLAND-Zen [98] are also shown for comparison. The inverted neutrino mass ordering region is computed using equation 1.37. The range account for the maximum excursion provided by effective Majorana masses between 10 meV and 50 meV, with $G^{0\nu}$ from [77] and $M^{0\nu}$ from [81] and [142]. The sensitivity of XENON1T and XENONnT can be increased with the log-likelihood ratio test statistics that takes into account the shape and uncertainties of the background model. This allows XENONnT to be on the leading edge of the currently $0\nu\beta\beta$-decay dedicated experiments and places DARWIN in the landscape of the next generation ones.

---

[4] Not described in this thesis.

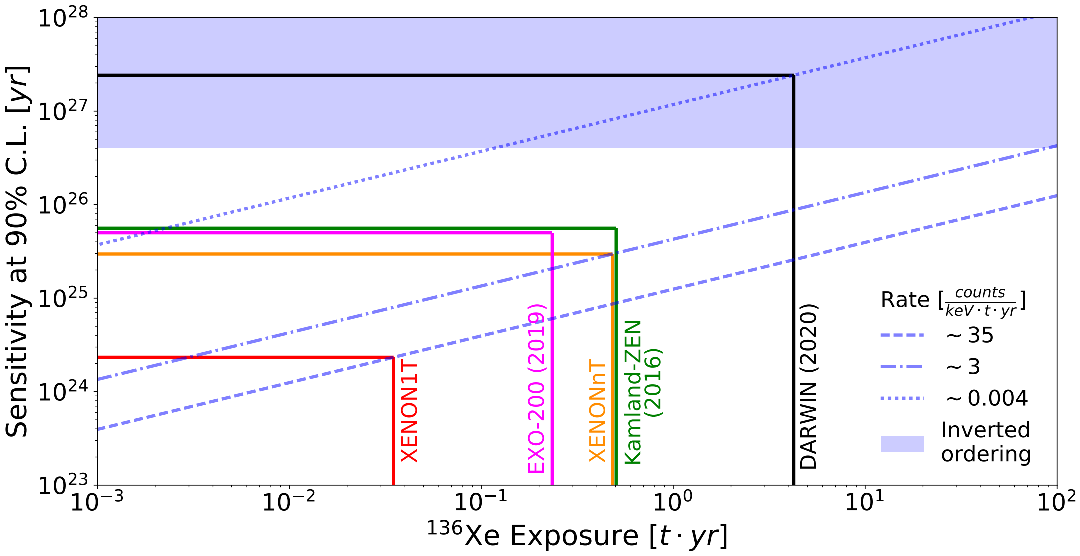

Figure 4.11: Empirical sensitivity to the $0\nu\beta\beta$ decay for XENON1T (red) and XENONnT(orange). The projections for Darwin ([100], black) and the results from EXO-200 ([94], magenta) and KamLAND-Zen ([98], green) are also shown. The dashed/dotted lines indicate background levels while the shaded purple region indicated the half-life corresponding to the inverted order.

CHAPTER 5

Building XENONnT [1]

The XENONnT experiment is the latest in a series of detectors built by the collaboration with the goal to look for WIMPs. It encompasses all the knowledge and experience gained in the previous 15 years of leading experiments in the field. A general introduction on the detector and the main physics reach is reported in section 2.3. In this chapter the focus is on the subsystems to which I contributed during my Ph.D. years. In particular, section 5.1 describes the light calibration system for the PMTs, of which I am responsible for, and the optical simulations I performed to finalise the design for the position of the fibres and their preparation for the installation. Section 5.2 describes the assembly of the XENONnT TPC at LNGS, of which I took part together with a dedicated team in the collaboration, followed by the first commissioning of the PMTs. Section 5.3 describes the method and the software developed to calibrate the gain of the PMTs. An outlook of the chapter is given in section 5.4.

5.1 The Light Calibration System

The calibration of the PMTs is a crucial aspect of the experiment. It allows us to estimate parameters such as the gain, single photoelectron acceptance, light emission and afterpulses rate, fundamental to reconstruct the detected signals. This system will be continuously used during the commissioning but also during the science data taking, to monitor the performance of each PMT and to model the time dependency. It is thus of primary importance to provide a homogeneous and stable light calibration system and to provide precise information for the data processing and consequently all the analysis.

The light calibration system of XENONnT, shown in figure 5.1, was partly developed

---

[1] The title of this chapter is the slogan used by the collaboration social media to show the incredible effort of the assembly and installation of the detector.

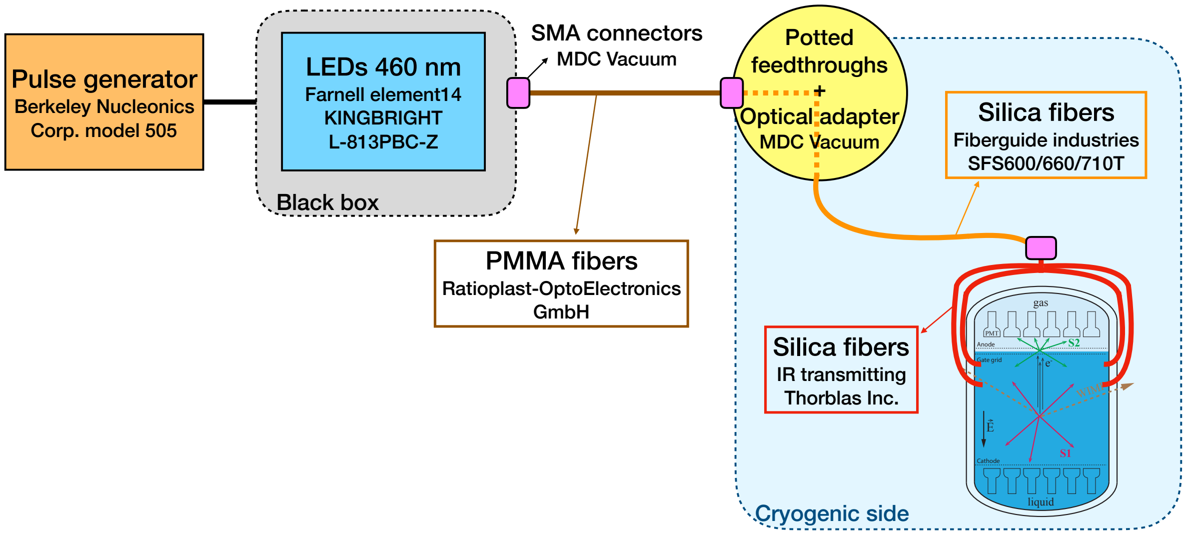

Figure 5.1: Light calibration system of XENONnT. The LEDs are located in a black-box in the DAQ and control-room and three types of optical fibers bring the light inside the TPC.

and tested for XENON1T at the University of Zurich. It consists of four blue light emitting diodes (LEDs ∼460 nm, Farnell element14 KINGBRIGHT L-813PBC-Z), placed in black-boxes, connected to optical fibres that bring the light inside the cryogenic system and the TPC through three different types of fibres. The fibres, described in table 5.1, have to satisfy the various conditions of temperature and cleanliness required at each stage. In particular, type-1 are four polymethyl methacrylate (PMMA or acrylic) fibres, covered by a black protection to optically isolate the fibres from ambient light (Ratioplast-OptoElectronics GmbH). In order to reach the feed-throughs from the DAQ room, these fibres are 7 m long and have SMA connectors (MDC Vacuum) on both sides. Two feedthroughs (MDC Vacuum) connect the PMMA fibres at room temperature to the cryogenic side. Type-2 are four silica fibres (Fiberguide industries SFS600/660/710T) that can work through a wide range of temperatures. This is essential because being placed into the cryogenic pipe they need to resist to high temperatures, for the radon emanation treatment done at 120°C, as well as cryogenic temperatures into the cold gas xenon at −70°C. These fibres are connected to the feedthroughs inside the cryogenic piping, and they have a stainless steel sheeting for 1.5 m while afterward they are naked, to reduce the amount of material close to the TPC. Type-3 are naked plastic fibres (Ratioplast-OptoElectronics GmbH) placed into the LXe, thus the material needs to be reduced as much as possible to avoid external radioactivity. These fibres have been substituted, during the installation, by silica fibres with a transmission band between 400 nm and 2400 nm (see sections 5.1.2 and 5.2). Each of the type-3 fibres is split into 7 strands to allow the light to be brought homogeneously into the TPC. As this type of fibre is very fragile and easy to break during

Table 5.1: Characteristics of the three different types of optical fibres sketched also in figure 5.1 in brown (type-1), orange (type-2) and red (type-3).

Fibre	Position	Material
Type-1	from LEDs to feed-through	1.0 mm PMMA core + 1.2 mm black plastic
Type-2	inside the cryo-pipe	660 μm silica fibres + 110 μm polyimide coating
Type-3	around and inside the TPC	250 μm PMMA fibres, 1to7 splitting

the heavy works of the installation, off the 7 terminations of each fibre, 6 will be installed to bring light, while one is an extra to substitute a broken one in case of an accident. A pulse generator (Berkeley Nucleonics Corp. model 505) is used to power the LEDs when the DAQ sends the trigger. All the channels are synchronised by the internal clock of the generator.

While type-1 and type-2 fibres are recycled from XENON1T, type-3 were purchased for XENONnT. They are connected through SMA connectors to the silica fibres and bring the light from the end of the cryogenic pipe into the active volume through holes in the sliding reflector panels, passing along the top of the diving bell (see the TPC description in section 2.3.2) and going down to its side. The final position of the endings of these fibres was fixed to allow for a homogeneous light collection efficiency on the PMT arrays and it was studied with GEANT4 optical simulations, described in the next section.

5.1.1 Optical Simulations

To finalise the design for the position of the fibres inside the TPC, I performed optical simulations with different configurations using GEANT4 version 9.5.1 and the framework developed by the XENON collaboration Monte Carlo group. The components of the TPC with their vertical positions, relevant for this study, are shown in table 5.2. The fibres are simulated as point sources at different z-coordinates to check the homogeneity of the collected light. The configurations taken into account consist of 24 photon point sources divided in two rings of 12 points each placed symmetrically around the TPC at a radius of 667 mm, placed respectively:

a. one ring at -1/3 and one at -2/3 of the Gate-Cathode distance;

b. biased towards the top with one ring at -1/3 and one at -20 cm;

c. biased towards the top with one ring at -20 cm and one at -25 cm.

Table 5.2: Vertical position and transparency of the main components of the XENONnT TPC.

Component	**z-position [mm]**	**Transparency [%]**
Top PMT windows	62.6375	
Top screening electrode	10.4	96
Anode	5.19	96
Gate	0.075	98
Cathode	-1477.55	97.2
Bottom screening electrode	-1527.65	97.2
Bottom PMT windows	-1541.06	
TPC radius	670	
Top-Bottom PMT windows	1603.6975	
Gate-Cathode	1477.625	

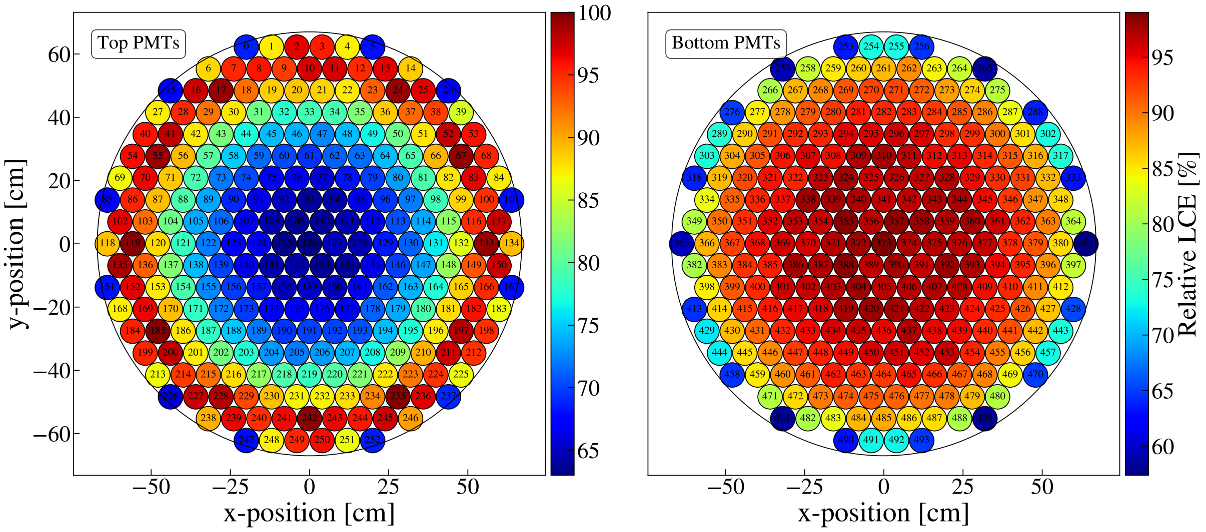

Figure 5.2: Relative LCE from optical simulations for the final configuration of the fibres in XENONnT, with two rings placed one at -20 cm and one at -25 cm.

Configuration a. was adopted in XENON1T. This resulted in a uniform LCE on the single PMT arrays but with a large discrepancy between the top and bottom arrays. This happens because the configuration is symmetric along z but the LCE is different between top and bottom. The light loss on the top array is due to the reflection at the interface of liquid-gas xenon caused by the different refraction indexes of 1.69 and ~1 for liquid and gas xenon, respectively. Thus I chose to investigate also a few positions with the fibres placed more towards the top of the TPC, namely configurations b. and c., to correct for the lower LCE of the top array.

For each position shown in figure 5.3 (A to L on the first ring and M to X on the second), 10^6 events are simulated for a total of 2.4×10^7 events. The average LCE are 30.36%, 27.33% and 26.65% for the configurations a., b. and c., respectively. A summary

Table 5.3: Comparison of the LCE on the PMT arrays, for the bulk and the external ring of PMTs, and estimation of the number of light levels needed for the calibration.

Position	**LCE bottom bulk [%]**	**LCE bottom outer [%]**	**LCE top bulk [%]**	**LCE top outer [%]**	**Light levels**
-1/3 and -2/3	95-100	70-80	32-37	25-30	3
-1/3 and -20 cm	90-100	65-75	55-65	70-80	2-3
-25 and -20 cm	85-100	65-75	65-75	85-100	2

of the relative LCE, normalised to the maximum PMT, for each configuration is reported in table 5.3. Despite the slightly lower average LCE, the chosen design is the configuration c.. A visualisation of its relative LCE is shown in figure 5.2. This is the one that shows the best uniformity in the light collection efficiency not only within the arrays but also between top and bottom PMTs. Having a similar LCE in the two arrays also allows us to reduce the light levels needed during the routine light calibrations, and thus increases the live-time for the science measurement.

The final choice of the fibre positions was selected also considering how the LCE would be in the case of some failures. While for a single broken fibre around the TPC (type-3) a spare one to be replaced is present in each set, if a connector is damaged or a silica fibre (type-2) breaks a whole set of fibres would not work, this means having 6 strands of type-3 not working. Optical MonteCarlo simulations were again used to study how the homogeneity would be in case of one or two full-set failures. Given the radial symmetry of the fibres in the TPC, when all of them are working their relative position in the two rings is irrelevant. However in the case of failures this is very important to know, and thus study, in order to avoid non uniformities or even not illuminated PMTs. To optimise the uniformity, the fibres coming from each connector are placed alternated in both rings. To not overlap two fibres in the same panel coming from the same connector, two configurations were tested:

- relative rotation of 30° between the two rings, left and middle sketches in figure 5.3;
- relative rotation of 60° between the two rings, left and right sketches in figure 5.3.

For the scenario in which one set of fibres breaks, nine fibres per ring are left. Which set, indicated by colours in figure 5.3, breaks is not relevant in this case as the result would be the same. The results from both configurations are also similar. The bottom array is still uniform. In the case of 30° rotation the top array shows a structure with 3 regions showing more light and corresponding to the place where the fibres are working in both rings, and 3 where they are on in just one ring. The same happens for the 60° rotation, in

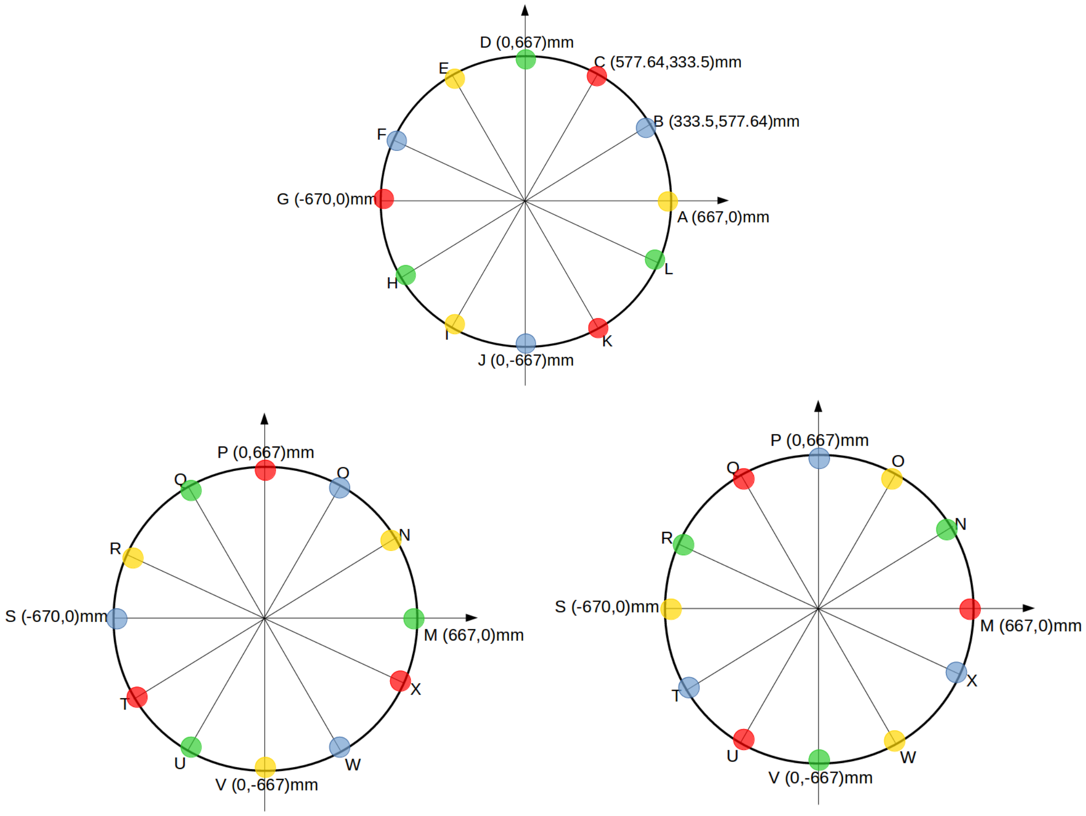

Figure 5.3: Radial position of the fibres, each colour represents fibres coming from the same connector. Top: ring at -20 cm with positions from A to L. Bottom left: ring at -25 cm with positions from M to X and rotation of 30° with respect to the ring at -20 cm. Bottom right: ring at -25 cm with positions from M to X and rotation of 60° with respect to the ring at -20 cm. This latter configuration is used for the installation.

6 and 6 smaller regions. In both cases the variation in the top array is still within the 20% excursion. Some PMTs in the outer ring fall in the lower light level, but it is still compatible with the light in the inner bulk of the top array. If two sets break we are left with six fibres per ring. While the bottom PMT array is always uniform, which set of fibres are working and which are not is relevant for the relative LCE pattern on the top PMT array. There are six possible combinations of not working couples of fibre sets for each configuration. For the 30° rotation there are two cases in which all the (x-y) positions have one fibre on and one off in one of the rings, so the light is homogeneous varying from 90% to 100% of the relative LCE and four positions with a repeated pattern of a central point with both fibres on, the nearest ones with one on and one off, with a relative LCE of 80%, and a position with both fibres off and a relative LCE of 60%. This latter result is shown in figure 5.4. For the 60° rotation there are two cases in which half of the (x-y) positions have two fibres on and half of them with two off and a relative LCE of 70% while four cases have all the positions with one fibre on and one off, so the light is quite homogeneous with a relative LCE between 90% and 100%. Following these considerations

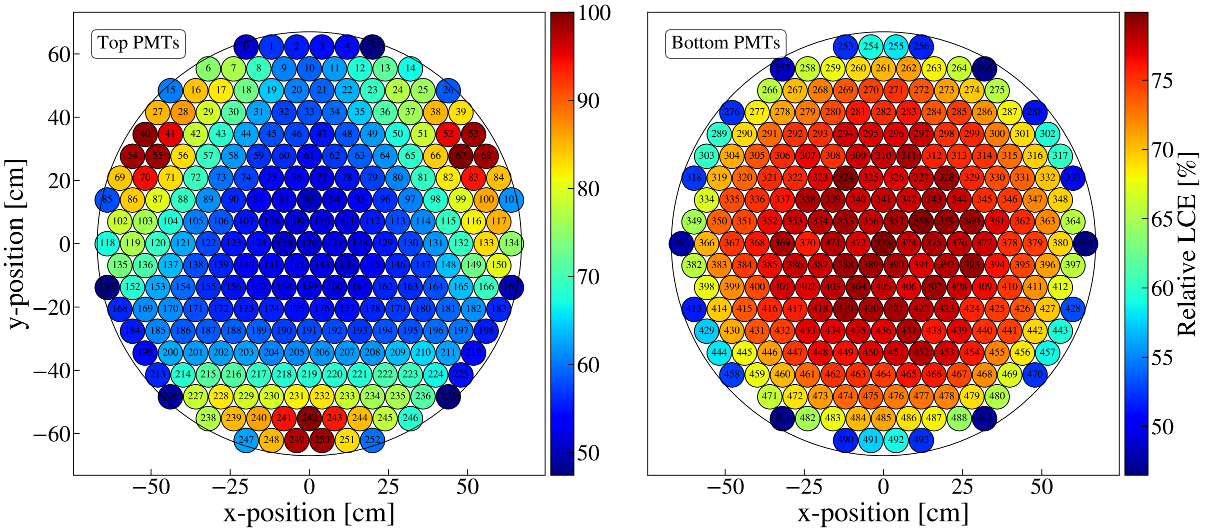

Figure 5.4: Relative LCE from optical simulations for the case with a rotation of 30° between the two rings and with two sets of fibres broken. In particular, referring to figure 5.3, the red and green sets are missing.

the configuration with a relative rotation of 60° between the two rings is chosen.

5.1.2 Optical Fibres

The type-3 fibres were prepared for the installation at the University of Zurich. Each set of fibres was unwound into 7 straight, single naked fibres with one common connector; this is shown on the left of figure 5.5. To facilitate the installation around the TPC, each fibre has been rolled on a plastic spool, of 15 cm diameter, while being cleaned with a wipe soaked with ethanol. The spools have been piled one on the top of each other into four towers of seven spools each, held together by two long M2 screws with knots, and the connector fixed on the top. An assembled tower of spools packed into a plastic bag is shown in figure 5.5 on the right. The spools have been previously cleaned in an ultrasonic bath (US-bath) with concentrated acid soap (Elma Clean EC60) for 15 minutes at 30°C, rinsed with deionised water and cleaned again in the US-bath with ethanol. Kapton tape was used to fix the fibres on the spools. Each tower was closed into a plastic bag and shipped to LNGS where it was cleaned once more in the US-bath with ethanol before being brought into the cleanroom for the installation.

To estimate the total background all the material of the TPC components have been screened for traces of natural radioactivity. A sample of the type-3 fibres was also sent to LNGS, prior the cleaning, to allow for inductively coupled plasma-mass spectrometry analysis (ICP-MS) measurements. The sample was cut and rinsed in purified water. 35 mg of PMMA fibres were baked in an oven at 650°C, rinsed with 10 mL of 10% HNO3 (nitric

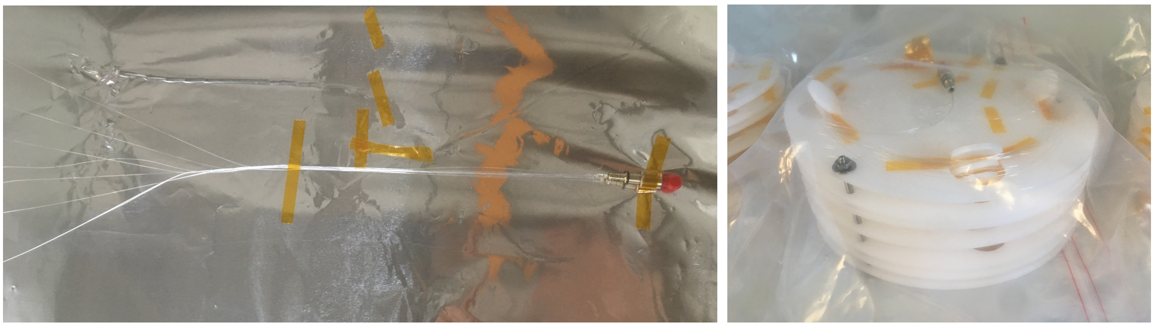

Figure 5.5: Left: SMA connector splitting into 7 naked fibres type-3 fixed with kapton tape during the preparation for the installation. Right: spools stacked into a tower for a set of fibres and packed into a plastic bag to be shipped to LNGS. The connector is visible on the top.

Table 5.4: Contamination measured with the ICP-MS in the sample of PMMA fibre.

Element	Unit	Sample
Th	ppt	1700±500
U	ppt	600±200
K	ppb	11000±3000

acid), then collected and measured. The results are reported in table 5.4. Given the total mass of fibre type-3 in the detector is <15 g, the activities are negligible compared to the total material background expected for XENONnT.

To install the fibres and provide a strain relief point, a clamp has been designed to hold the fibres on already assigned holes on the top of the bell. The clamps are made of two PTFE parts with M4 silver plated and vented screws fixing them to the bell and M2 PEEK screws holding the two parts together. The fibres go down on the side of the bell and reach the top of the PTFE pillars that hold the structure of the field cage. Here two holes of 2 mm diameters have been added on the top of each pillar to make the fibres run around the perimeter of the field cage. Half of the fibres run in the clockwise direction to reach their respective position situated on the closer half of the cage and the other half of the fibres run anticlockwise on the other half of the cage. In this way a maximum of 6 fibres can pass through each hole in the pillars. Once a fibre reaches the assigned reflector panel it goes down to the z-position where a 250 μm hole has been previously drilled during the machining of the panels. The insertion of the fibres into the panels was tested in advance with a mock-up provided by the Freiburg group. More details about the installation of the fibres during the XENONnT TPC assembly and the outcome of it is described in section 5.2.

Shortly before the installation of XENONnT, an R&D programme has been proposed by the Purdue group to try to remove or decrease the single electron background [143, 144].

Table 5.5: Comparison of the properties between the type-3 fibre similar to the one used in XENON1T (standard) and the type-3 fibre selected to transmit also IR light (new).

Property	**Type-3 Standard**	**Type-3 New**
Company	Ratioplast-OptoElectronics GmbH from Toray Industries	Thorlabs Inc.
Core Material	Polymethyl Methacrylate	Pure Silica
Cladding Material	Fluorinated Polymer	Fluorine-Doped Silica
Transmission		400-2400 nm
Maximum Attenuation	0.35 dB/m (at 650 nm)	8 dB/km (at 808 nm)
Operating Temperature	-55 to 70 °C	-40 to 85 °C

This is due to thermalisation and trapping of electrons just below the liquid-gas xenon interface. To be extracted into the gas phase, the electrons needs to win the potential barrier imposed by the dielectric interface. This background affects the tail of the S2 signals and it is thus particular relevant for analyses using the ionisation channel. The proposal consists in shining infrared (IR) light into the LXe, at a wavelength not visible by the PMTs, to provide energy to the trapped electrons to overcome the potential barrier. As the design of the various parts of the detector was already fixed, the IR source would eventually exploit the same optical fibre system and connections of the light calibration one. This requires to use fibres that can transmit IR light. Type-1 fibres can be substituted at a later stage while the fibres within the cryogenic system needed to be adapted before the installation. The silica fibres (type-2) in the cryogenic pipe transmit between 190 nm and 1250 nm. We thus decided to replace two of the four sets of fibres type-3 with glass-clad fibres with a silica core and a fluorine-doped silica cladding (Thorlabs Inc.). The replaced sets are indicated in red and blue in figure 5.3. The transmission band rated for these fibres is 400-2400 nm thus it can be also used for the LEDs blue light of ~460 nm. The properties of this fibre are reported in table 5.5 compared to the standard type-3 fibre used previously. Two sets of the IR transmitting fibres have been cleaned and prepared by the Purdue group following the procedure detailed above and then shipped to LNGS where they were further cleaned with an additional US-bath with ethanol.

5.2 TPC Assembly and Installation

The assembly of the TPC was carried out at LNGS from February 24th to March 5th, during 10 intense days. All the materials had been prepared, shipped and cleaned in advance with ethanol, soap or acids according to the specific recipe for that material. The assembly was performed in an ISO-5[2] cleanroom in the Hall di Montaggio at the external laboratories. A second, smaller cleanroom, also located in the Hall di Montaggio, was used to parallelise some preparative work. On March 5th a truck for special transportations brought the TPC underground where it was lifted into the watertank. The entrance of the watertank was protected by a greyroom (a separate area whose air purity is better than that of the surrounding spaces, but which does not necessarily offer clean room quality) and another ISO-6 cleanroom was installed inside, around the final place of the TPC to allow for the installation, connection and test of all the systems before the cryostat could be closed. The procedure to enter the cleanrooms requires a few steps to minimise as much as possible the amount of dust and human contamination (floating hair, dead cells, skin grease). An additional greyroom is standing before the entry where one can dress up properly. Shoes and extra clothes have to be removed before entering the greyroom as well as wearing gloves, cover shoes and hair nets while stepping in. In the greyroom a new pair of gloves, a face mask, a full body suit and plastic boots must be worn in a precise order. Right before entering the cleanroom a second pair of gloves is put above the other and one stands for a minute below a flux of air directed toward the bottom. The main steps followed during the assembly and the installation underground of the XENONnT TPC will be described in the next subsections.

5.2.1 Assembly Above Ground

The two PMT arrays have been assembled in advance with 253 PMTs on the top and 241 in the bottom array. They have hexagonal patterns to maximise the active surface[3] viewed by the arrays. The PMTs are fixed, in both arrays, by 21 mm thick copper plates while a PTFE reflector holds them at the photocathode. Each of the 494 PMT bases is connected to three cables, a kapton cable for the ground, another kapton cable carrying the high voltage (HV) to power the PMT and a coaxial cable to bring the signal to the DAQ. The top array has been inserted into the bell while the bottom has been rotated, with a customised tool, by 180° to have the photocathode orientated toward the top. A picture of the assembled bottom array is shown in picture 5.6, with the bottom screening electrode overlaid. To shape and support the field cage, PTFE pillars have been mounted

---

[2] According to the International Organization for Standardization (ISO) the maximum concentration of particles such as dust and airborne organisms for a ISO-5 cleanroom is 100,000 per m^3. For an ISO-6 it is 1,000,000.

[3] Surface on the x-y plane directly monitored by the PMT photocathodes. It is $1.154\,\mathrm{m}^2$ for the top and $1.099\,\mathrm{m}^2$ for the bottom PMT array.

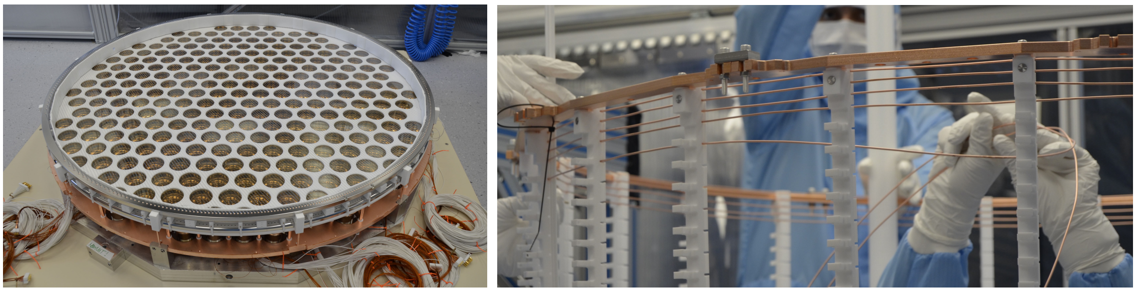

Figure 5.6: Left: bottom PMT array with the bottom screening electrode. The cables are soldered to the PMT voltage dividers and arranged in bundles according to the relative cabling plan. Right: installation of the copper wires on the PTFE pillars structure. The supporting points for the wires, on the inside, and the rings, on the outside, are visible.

and fixed by a top copper ring and bottom copper segments. The 71 field shaping wires have been fit into holding points on the inside of the pillars, as shown on the right side of figure 5.6, and then the 48 reflector panels have been fixed to the wires. This results in a smooth white and reflective inner surface of the field cage. The two resistor chains are used to ensure the right resistance to the wires. Each resistor was connected one by one using stainless steel M2 screws and Teflon pieces to hold them, and all the wires have been tested after the connection. A picture of the assembled wires with one of the resistor chains and the panels is shown in figure 5.7 on the left. The 64 copper rings have been assembled starting from the bottom to provide more stability. Each ring is split in two halves to facilitate the procedure. They are supported by the external side of the pillars where a holding structure is present. At the junction of the two half-rings, another two resistor chains have been installed. In this case the operation is not trivial as the chain must stay between the reflector panels and the rings. The wires of the resistors need to be rolled around the M2 screws and fixed by tightening the knots. In figure 5.7, in the centre, part of one of the assembled resistor chains of the field shaping rings is shown. In correspondence of the pillars, external PTFE columns and cable trays are installed using PEEK screws to keep the rings pushed inside and to provide space to drive the cables coming from the bottom PMT array to the top of the bell once they are connected underground. Before placing the last 9 rings, the optical fibres must be installed following the scheme presented in section 5.1.2. The uppermost copper rings will serve as protection for the path of the fibres from the top PTFE pillars to the holes they are going through the panels. To localise the 250 μm holes in the panels, a person was standing inside the field cage shining light through the corresponding hole and pulling gently the fibre once passed through. Some friction was developing between the fibres when passing in the holes on the top of the pillars. During the assembly aboveground, all the 24 fibres were installed successfully one by one unrolling the spools on the piles. One spool for each

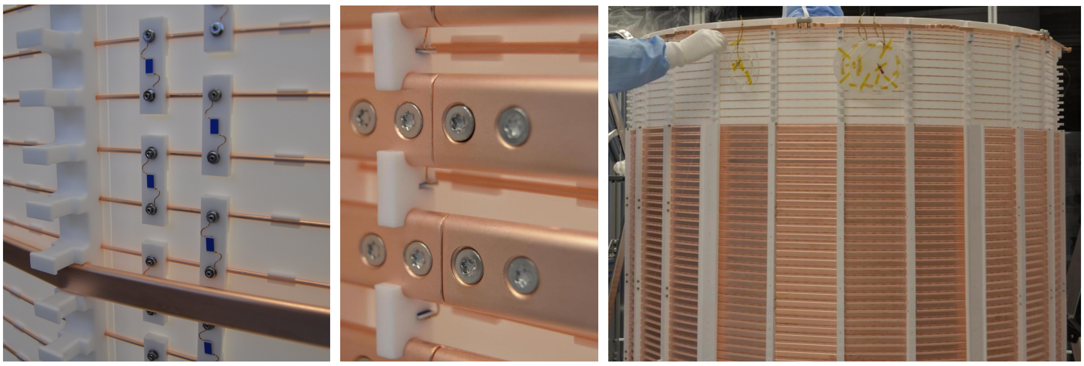

Figure 5.7: Left: resistor chain connecting the field shaping wires. The reflector panels fixed to the wires and the external side of a pillar with the supporting structure for the rings are also visible. Middle: junctions between the two halves of the shaping rings. The resistors connecting the rings are held by small PTFE pieces and connected on the inner side of the rings. Right: section of the field cage with the assembled shaping rings, excluded the uppermost ones to allow the installation of the optical fibres. Four spools were left attached to the top ring to protect the connector and the last portion of the fibres for the transportation underground.

pile, with the spare fibre and the connector, was attached to the top guard ring to keep them secured for the transportation underground where they have been connected at the end of the cryogenic pipe. This is shown in the photo on the right of figure 5.7. The last uppermost rings have then been installed and the fibres have been tested shining light at the connector side with a flashlight and verifying the correspondence of light inside the field cage. All the fibres were transmitting light inside the cage and thus they were cut at a distance of about 4 cm from the inner surface of the reflector panels inside the field cage.

The five electrodes have already been assembled and prepared in advance by a dedicated team. The gate, anode and top screening electrode have been fixed on the top of the field cage and then the assembled cage was lifted to be attached to the bell and the top PMT array. Three winches and a solid frame, that will serve also for the transportation, have been used to lift the field cage up to the bell and the top array. A turn of the winches corresponds to 1 mm in height and for most of the time the lifting was done in a quarter of turn, thus 250 μm at a time. At this stage, a load test was performed, using lead bricks to simulate the weight of the missing bottom PMT array and electrode, to ensure the supporting frame was stable. The lead bricks had been wrapped in clean plastic foils to enter into the cleanroom. Before proceeding to connect the bottom array, the pillars were measured again. Due to the weight of the whole structure they were compressed and their final length was between 1591 mm and 1593 mm. To correct for this discrepancy, PTFE washers have been added on the bottom part of the pillars. Finally, after having placed the bottom screening electrode and the cathode on the bottom array, it was attached to the field cage. A photo of the assembled TPC attached to the frame for the transportation

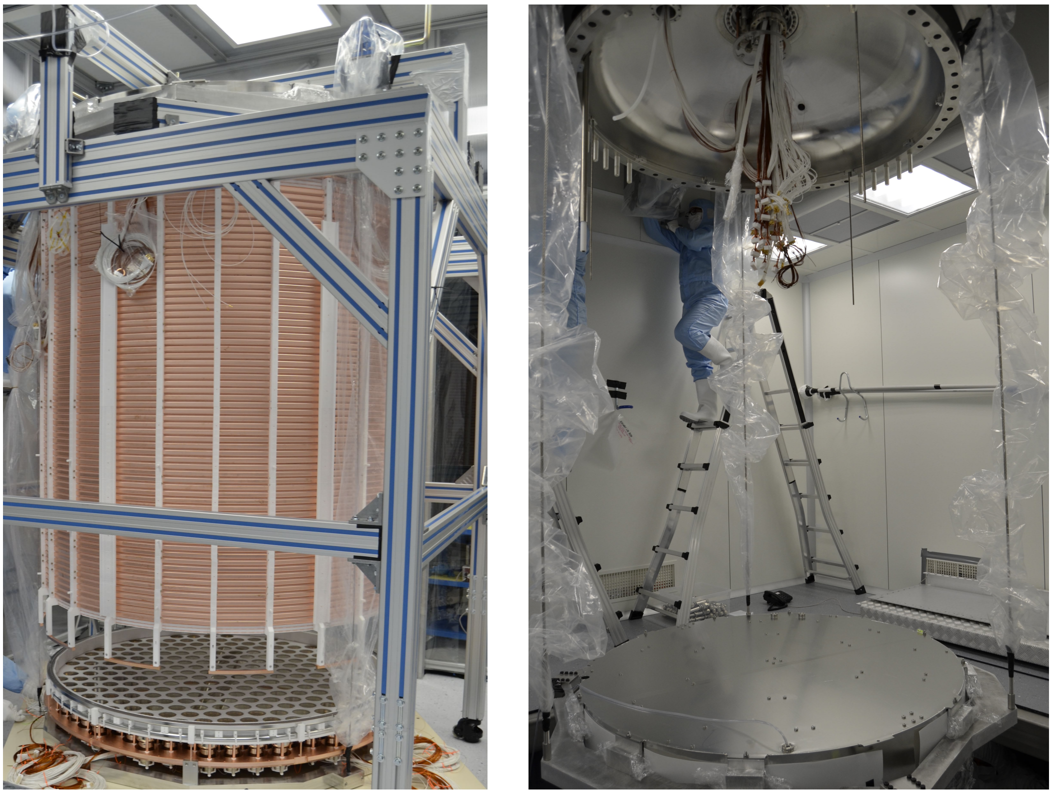

Figure 5.8: Left: the assembled TPC, in the aboveground cleanroom, attached to the bell and top PMT array, right before fixing the bottom PMT array. Cables and spools have been arranged with cable ties. All around is visible the support structure. Right: the TPC being lifted into the cleanroom inside the watertank. Cables and fibres are hanging from the top of the cryostat where the pipe is connected.

is shown in figure 5.8 on the left. The assembled TPC was enclosed in a Mylar bag to protect it from the external environment and then the frame structure was wrapped in plastic foils.

5.2.2 Installation Underground

Before the TPC arrived underground, we tested the connections between the two ends of the cryogenic pipes, one already used in XENON1T and a new one. The SMA connector of a silica fibre was missing[4] and not possible to repair on-site due to the delicate procedure to cut the silica fibre and glue the connector while suspended from the pipe in the cleanroom. The other three silica fibres were tested by shining light into them from the ending outside the watertank. The HV and signal cables used in the XENON1T pipe were reused together with some spare ones present in that pipe, while new cables have been purchased and prepared in advance for the new pipe. Unexpectedly the spare cables, making up to six connectors, were bent and stuck into the pipe. It was not possible to open the pipe at

---

[4] It was broken/detached either during the XENON1T assembly or disassembly.

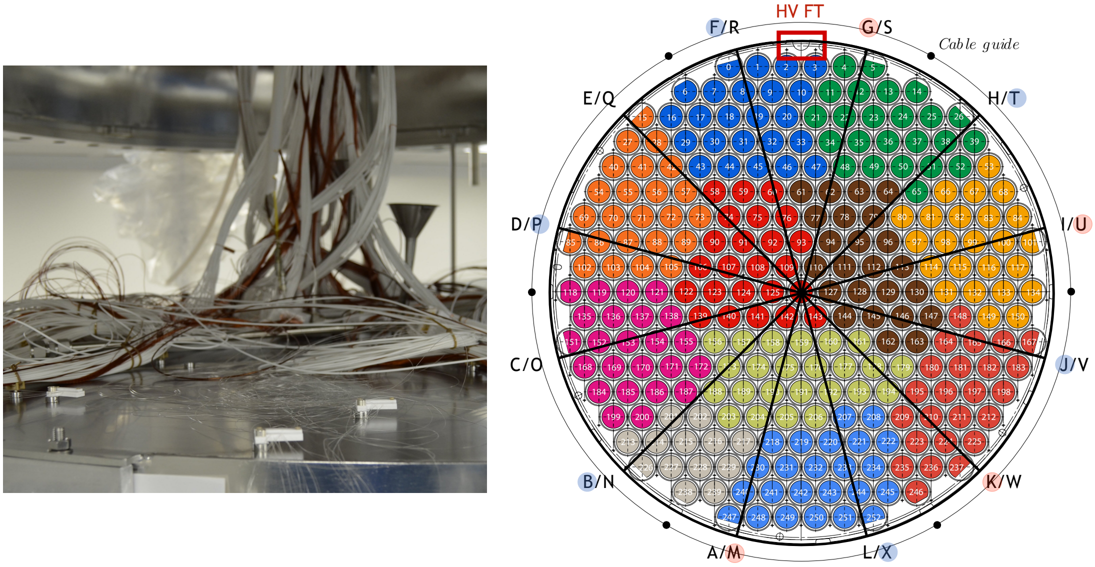

Figure 5.9: Left: top of the bell with PMT cables and fibres connected. In the foreground is the part of the bell where the fibres are placed and fixed with the clamps. Right: final scheme of the working fibres inside the TPC overlaid with the top PMT array map. The double letters indicate the position of the fibres in the two rings. The letters in the coloured circles are the installed and working ones belonging to the two IR sets.

that time and the cables were pulled out by force. The operation caused the damage of a working silica fibre which broke inside the pipe and came out. This left the pipe with only two working silica fibres that allowed the connection of two of the four sets of fibres, meaning 12 fibres going into the field cage. All the HV kapton cables and signal coaxial cables were tested with a multimeter. An extra connector was present in the pipe and the few not working cables were substituted.

Once underground the TPC was brought into the watertank and lifted, using again the winches, into the cleanroom and close to the top of the cryostat. In figure 5.8 on the right a picture taken during the lifting is shown. Cables and fibres are hanging from the opening of the cryogenic pipes. All the cables have been routed to the top of the bell. The ones coming from the bottom PMT array were guided along the six PTFE cable trays and arranged with eleven PTFE holders and correspondent PEEK screws. On the top of the bell the connectors were matched with the ones coming from the pipes according to a pre-designed cabling plan. Then the cables were fixed using PEEK clamps and cable ties. A quarter of the surface on the bell was left free for the fibres. The top of the bell during the cable and fibre connection is shown in figure 5.9 on the left.

During the procedure one HV cable was cut but it was repaired using a spare HV connector made for the electrodes. The remaining spools were removed, together with the spare fibres, and two sets were connected to the silica fibres. During the connection of cables, electrodes and resistors, a few fibres were also pulled out from their final position. Among the remaining fibres, the more homogeneously distributed were the IR transmitting ones. Given that previous tests showed they also transmit the ∼460 nm light of the LED, we decided to connect these two sets. Two fibres of the IR sets were pulled out, leaving 10 out of 12 final working fibres going into the cage. A scheme of the working fibres installed in the TPC is shown in figure 5.9 on the right. The fibres were then fixed to the top of the bell using the PTFE clamps described in section 5.1.2 and visible on the left part of figure 5.9. A removable PTFE tube was placed over the silica fibres and SMA connectors to protect them for the following lifting of the TPC. Eight capacitive level meters were installed around the field cage, two long and two medium to monitor the liquid xenon level during the filling and four short ones to constantly monitor the stability during the data taking. Seven resistance temperature sensors, PT100, were also placed around the TPC to monitor the temperature. All the remaining cable ties were removed, the connections of the electrodes tested and the piping for the xenon lines were fixed. The TPC was lifted using the winches. During the lifting a coaxial cable of a short level meter was pinched, but the cable was repaired. Finally, PTFE panels were placed all around the bottom part of the shaping rings as further protection when closing the cryostat. A picture of the TPC lifted in the final position is shown in figure 5.10. The protection panels are installed, except for the last one in the front of the picture. Two of the cable trays and the PTFE tube for the cathode connection are also visible.

Figure 5.10: The TPC in its final place. The last PTFE protection panel is not yet installed and two of the cable trays and the PTFE insulator for the cathode connection are visible.

Notes on the Optical Fibres Installation: Following the XENONnT TPC assembly and installation I want to summarise a few lessons that should be considered in future experiments:

- Rolling and unrolling the fibres on the spools requires a few days and it is a very delicate procedure where fibres can easily break or be kinked.
- The fibres were affected by some friction when passing through the holes on the top of the pillars. Not having any anchoring points would result in having transparent naked fibres around and thus very easy to break. However having a dedicated route would require some modifications at TPC design level.
- To localise the 250 μm holes in the PTFE reflector panels was quite easy with the help of a flashlight. Additional anchoring points right before the holes would reduce the probability to have them pulled out by other works around the TPC.
- To reduce the accidents it is suggested to not parallelise the work on the fibres with other TPC works. This would avoid having fibres not safely secured in a position that can be easily pulled while working around the TPC.
- Having a quarter of the bell free of cables was helpful and reduced the risk of damage.

The installation procedure would be much easier when using more resistant coated fibres. This increases the amount of material coming from the light calibration system. Given the low mass and thus background contribution of the fibres it would be a good compromise in terms of handling and risks.

5.2.3 First PMT Commissioning

Once the inner vessel of the cryostat was closed around the TPC, the commissioning phase of XENONnT started. Among the several systems to test during this phase, I contributed to the commissioning of the PMTs and the light calibration on-site.

The first step was to route and connect all the signal and HV cables of the PMTs from the feedthroughs of the cryogenic system to the amplifiers in the DAQ chain and the power supply boards, respectively. A scheme of the air-side connection of the PMTs is shown in figure 5.11. The signal cables were routed using a metal rack and cable ties from the cryogenic floor to the DAQ floor and connected to the Phillips 776 amplifiers according to their own label and channels map. The amplified signal is sent to CAEN V1724 digitisers. The HV cables were routed similarly and connected to CAEN A1535N

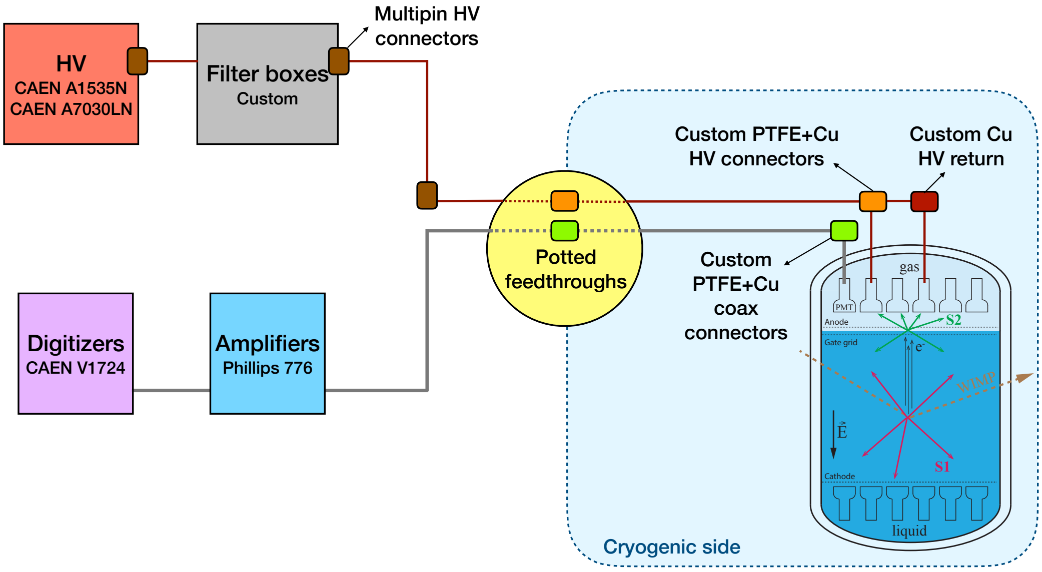

Figure 5.11: Simplified scheme showing the connections between the PMTs, the HV and the DAQ.

and A7030LN boards into two HV crates.

Once the TPC was light tight the PMTs were ramped up one by one to 1300 V and the dark count (DC) signals checked with an oscilloscope (to 1500 V in case no signal was present). During the first test 9 PMTs showed no signals, 5 on the top and 4 on the bottom. PMT numbers 7, 137, 207, 247, 248 on the top had no current flowing while on the bottom PMTs 415 had no current flowing, 354 and 386 had current but still no signals and 427 tripped at 1200 V. While ramping up the PMTs we realised that 2 of the 21 sectors in which they are grouped, and thus placed into the same connector, have been switched or mirrored. The cables are made of several parts connected together according to the path they have to follow from the TPC to the air-side, so it is impossible to know where this switch happened. Moreover, without the presence of a localised S2 signal it is not possible to distinguish if it happened on the HV or the signal cables. A new map was provided for the slow control to account for it.

To commission the light calibration system, the pulser for the LED was temporarily adjusted on manual operation following the setting used in XENON1T and the LEDs powered in continuous mode at 4 V with 200 ns width. The four available LEDs were all working. A picture of the power generator and the blue light coming from the LEDs is shown in figure 5.12 on the left. The optical fibres have been connected with the two working sets attached to channels T2 and T4 (input 1a and 2b on the cryogenic flange). 16 PMTs were selected to check the light signals, four located in the inner top part, four in the outer top, four in the inner bottom and four in the outer bottom part. The light

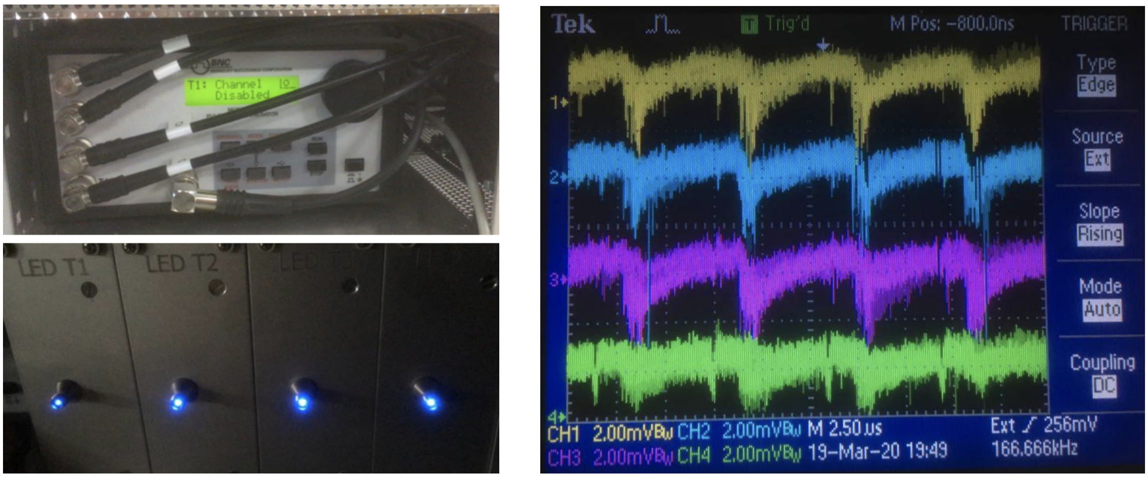

Figure 5.12: Left: pulse generator (top) and blue light coming from the four LEDs (bottom) during the manual operation test. Left: LED signals detected by four PMTs during the first light calibration.

coming from the two sets was checked first separately and then together with all the selected PMTs. All of them were seeing light. A photo of the signals in the outer bottom PMTs is shown in figure 5.12 on the right. The pulse generator was switched to remote mode to finalise the setting for the data acquisition.

Once the slow control was configured the two PMT arrays were ramped up for stability tests at 1300 V and to acquire noise runs in self-trigger mode to study the working condition in vacuum. During these tests, boards 5 and 6 on the older HV crate, to which the bottom array is connected, had a glitch and the whole bottom array shut down twice. The HV crate was consequently replaced with a new one and the following stability tests at 1300 V, 1400 V and 1500 V were successful.

During the commissioning phase of XENON1T it was discovered that one of the main sources of noise in the PMTs was produced by their HV power supply. To reduce this noise, three customised filter boxes were produced and installed in the HV chain right after the power supply. The circuit in the filter boxes is a simple low-pass passive filter for each channel, with a 2.8 MHz cut-off frequency. Inside a box, four boards are present, each carrying the circuits for 24 channels (1 connector). In XENONnT the filter boxes were reused for the channels in the top array and three new similar filter boxes were installed for the bottom array. The noise RMS (root mean square) in the bottom array was reduced by an average of 35%, while the noise in its innermost part only was reduced by an average of 50%.

After replacing the HV crate and installing the filter boxes, a few other PMTs showed current problems. We noticed that several pins in the HV connectors (Radiall high voltage multipin) were pushed inside them, losing mechanical contact between the male and female

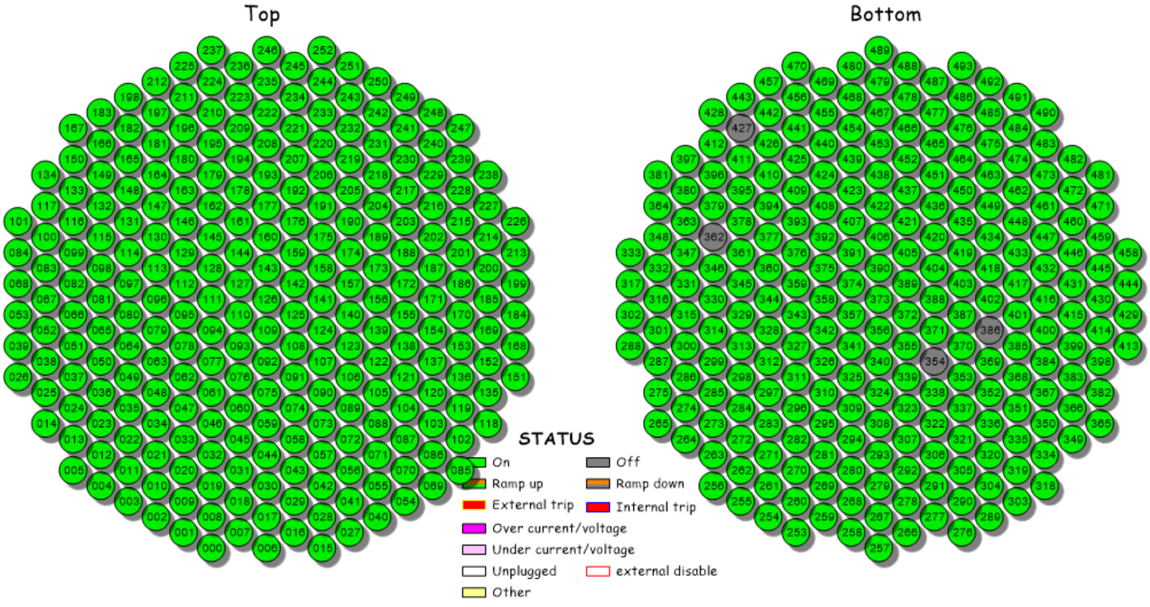

Figure 5.13: Screen of the PMT map on the slow control interface at the end of the first commissioning phase. In green the working PMTs with status ON while in grey the four problematic PMTs turned off.

pins. This was the case for all the non working PMTs that showed no current. The respective connectors were thus disassembled and the pins pushed out and glued to the pins plastic holder. All the PMTs with current-related problems but one were fixed and they were functioning afterward. PMT 185 in the top array still had a HV pin problem due to the loosening of the female pin at the connection after the filter box. This problem was later solved by replacing the relative cable on the air side between the filterbox and the cryogenic flange.

At the end of the first commissioning stage only four PMTs were still problematic, all on the bottom array. Two of them, PMTs 354 and 386, have current flowing but no signal is present, and this can be an indication that the signal cables detached from their bases. PMT 427 trips at 1200 V, and PMT 362 started to trip around 1400 V but could be used at lower voltages. A map of the PMT status at this stage is shown in figure 5.13. Several LED datasets were acquired to adjust the setting of the DAQ and find the optimal working point for the PMTs. A few discrepancies between the setting of the DAQ and what was seen in the data pointed out some problems with the DAQ chain. In particular the light was detected by the PMTs once every three triggers. This was due to a missing NIM/TTL converter and NIM timer modules. Thus the light calibration was temporarily performed applying a software threshold requiring to select only the triggers in which a minimum amount of light is recorded. The modules were installed in a later stage by DAQ experts from the collaboration and now the detected light and the DAQ trigger are synchronised.

5.3 PMT Gain Calibration

One of the first possible measurements with the installed TPC is the calibration of the PMTs, that was performed already in a vacuum and nitrogen controlled environment before starting filling with xenon gas. Furthermore this is fundamental to fix the operation setting of each single PMT in terms of HV, gain, single photoelectron (SPE) acceptance and afterpulse rates. The software framework was developed before and during the commissioning of XENONnT by the DAQ, PMTs and analysis groups. In particular I worked on developing the software to process and analyse the LED data for the gain estimation. For the science data it is ideal to have the PMTs set as much as possible to similar gains to ensure a uniform response of the signals. This requires to set the HV of each PMT to a different value to be determined with the first calibrations. The gain is a parameter that has to be routinely monitored during all the science data taking, as its time evolution affects the reconstruction of the signals. In the following I will describe the methods for the gain determination.

5.3.1 Model Independent Method

Usually the gain calculation relies on fitting the SPE peak, with a Gaussian [145] or more complicated functions, in the integrated signals spectrum. To avoid systematics coming from the higher order photoelectron peaks a requirement to adopt this method is to have 0.5-2 PE per trigger, that means shining low-intensity light. Besides the difficulty in finding the right setting, a few other issues contribute to the uncertainties in the fitting method. A non-negligible probability of an under-amplified signal can occur when the incident photons produce photoelectric effect on the first dynode instead on the photocathode [146] or the photoelectrons skip one or more dynode amplification stages [147]. Under-amplified electrons can contribute up to 20% to the SPE spectrum, and their distribution overlaps with the noise one. For these reasons it is also difficult to model the shape of the SPE to fit. An alternative method was implemented during the XENON1T data taking and is referred to as the model-independent single photoelectron calibration [148]. This is a statistical method to calibrate the mean and variance of the SPE, making no assumptions on the shape of the peak or the underlying distribution of the fully-amplified photoelectron spectrum and including the latter in the calculation. Furthermore it is very easy to implement as it allows for a higher and wide range of light intensity and does not need fine tuning of the parameters as it does not involve any fit. Thus it is also easily applicable to a large number of PMTs. To perform this calibration it is necessary to acquire two types of datasets:

1. Noise or *LED-off* run: the LEDs are set to a small value, 1 V in case of XENONnT, that is lower than the level required by the LEDs to shine light.
2. Signal or *LED-on* run: the LEDs are set to the intensity such as the PMTs detects around 2-3 PE per trigger, around 6 V for XENONnT (see section 5.3.2).

In both cases the trigger is sent by the DAQ to the pulser. From these runs two integrated signal spectra can be obtained. For the acquisition (1) the spectrum, B, consists in electronic and background noise, while for (2) the spectrum, T, is made up of electronic and background noise in addition to the LED pulse signal. An example of these spectra is shown in figure 5.16 in the specific case of a XENONnT PMT. For independent random variables, the first two momenta, $M_{1,2}$, are additive:

$$M_{1,2}[T] = M_{1,2}[B] + M_{1,2}[S] \tag{5.1}$$

where $S = \sum_{p=0}^{\inf} S_p L(p)$ is the distribution of the LED signals only, without the noise, p the number of photoelectrons produced and $L(p)$ the distribution of the number of photoelectrons produced in a single pulse. The SPE distribution is then given by $S_1 \equiv \psi$ and, assuming a Poisson distribution for the LED light emission, its mean and variance are, respectively:

$$E[\psi] = \frac{E[T] - E[B]}{\lambda} \tag{5.2}$$

$$V[\psi] = \frac{V[T] - V[B]}{\lambda} - E^2[\psi] \tag{5.3}$$

where the occupancy $\lambda = -\ln(L(0))$ is linked to the probability to produce zero photoelectrons. This parameter can be estimated from the number of zero LED-induced photoelectrons in the LED-on run, N_0, and the total number of events, N.

$$\lambda = -\ln\left(\frac{N_0}{N}\right) = -\ln\left(\frac{A_S}{A_B}\right) \tag{5.4}$$

where A_S is the number of events which fall below a threshold in the LED-on dataset. The choice of the threshold is done such as to minimise the number of non-zero photoelectrons falling below it. A_B is the number of events which fall below the threshold in the LED-off dataset.

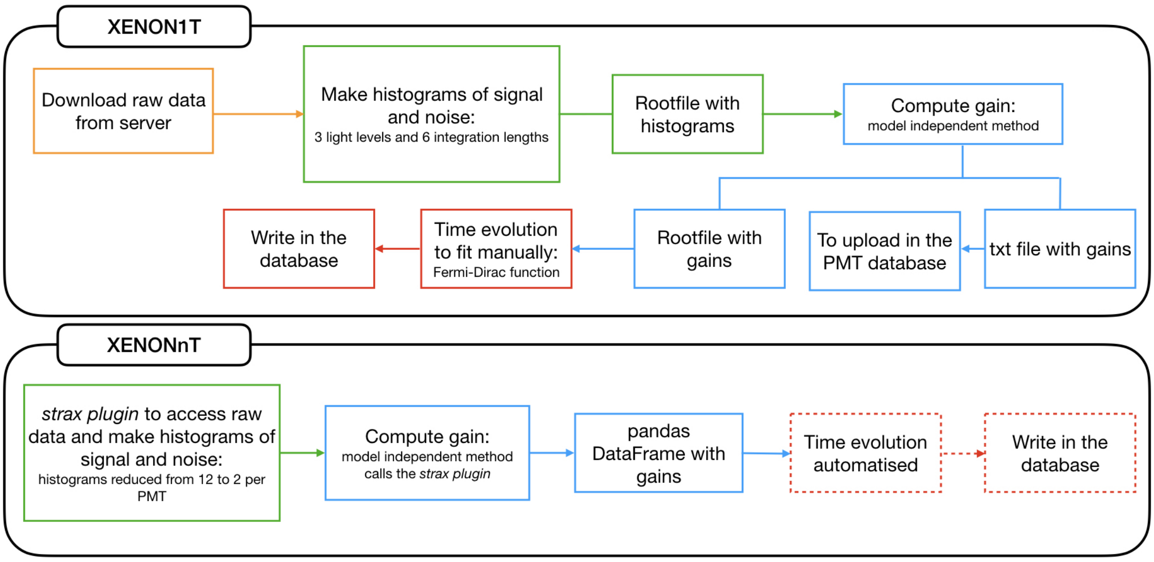

Figure 5.14: Scheme of the steps required to compute the gain in XENON1T (top) and in XENONnT (bottom). The new software does not require manual access to the raw data and less steps are needed for the calculation. The dashed boxes indicate the steps still under development.

5.3.2 Software and First Results

The model independent method was implemented for the gain calibration during the XENON1T operation. However it required several manual steps as it was not integrated into the processing chain. For XENONnT the main work consisted in developing and automatising the software into the new processor, based on *strax* (STReam Analysis for Xenon TPCs) [149]. The new processor is ×100 faster than the XENON1T one, and it allows for direct access and managing of the raw data through customised *plugins* and communication with the MongoDB database. The software schemes for the LED calibration in XENON1T and XENONnT are shown in figure 5.14. A customised *plugin* (*led_calibration.py*) is integrated into the processor and it accesses directly the raw data, without requiring the user to download the datasets manually. The *plugin* gives as output the variables needed for the gain and SPE acceptance calculations. In particular, two functions are implemented:

- *get_area*: used for the gain computation, sums the data in a defined time window to get the distribution of the integrated charge. This is repeated in 6 different integration windows to account for systematics in choosing the right sample at the end of the signal window, and it returns the average area. In XENON1T the gain was computed on the different windows and only at the end the gain values were averaged. The new implementation yields the same result with less computation time.

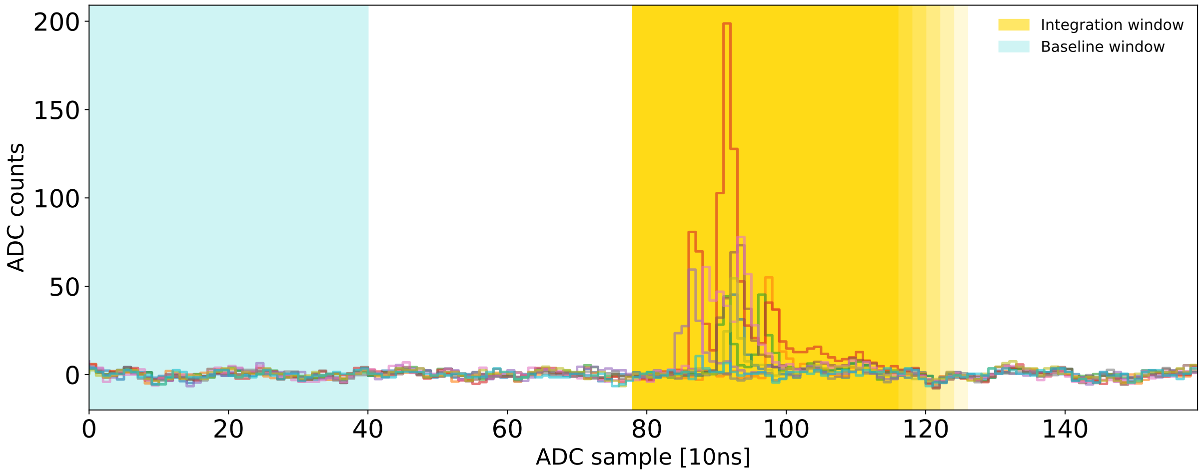

Figure 5.15: LED calibration acquisition window. The baseline is computed in the first 40 samples (light-blue region), while the signal is collected in 6 integration windows starting at sample 78 and with a different ending sample (yellow shaded overlapping regions).

- *get_amplitude*, used for the SPE acceptance, takes the maximum signal amplitude in a defined window.

The *plugin* takes some configuration parameters that can be modified without being hard-coded. These are the windows for the baseline calculation and for the signal collection. A channels list with the number of PMTs that the user wants to analyse is also given as configuration parameter. The latter is useful to eventually check problematic PMTs. By default all the 494 PMTs are selected. During the XENONnT commissioning, the acquisition window is selected to allow for the baseline computation before collecting the whole integrated charge, for a total of 160 samples[5]. An example is shown in figure 5.15. The first 40 samples are used for the baseline calculation. The signal window starts at sample 78 before the beginning of the rise time. The first integration endpoint is at sample 116, while the following windows increase by 2 samples from the previous one, with the last ending at sample 126. The average baseline is subtracted before computing the variables needed for the analyses. An example of the integrated charge spectra produced for the LED-off and LED-on runs of PMT 300 is shown in figure 5.16. The runs are selected to have the same number of triggers, so the noise peak in the LED-off spectrum is higher than the one in the LED-on.

For the first commissioning phase in vacuum and nitrogen, the LEDs were set to a 100 ns width with the external trigger sent by the DAQ after a delay of ~800 ns. To find the optimum light level, several datasets have been acquired ranging from 3 V to 8 V. The setting was then chosen so that the occupancy of all the PMTs was around 2-3

---

[5] 1 ADC sample = 10 ns

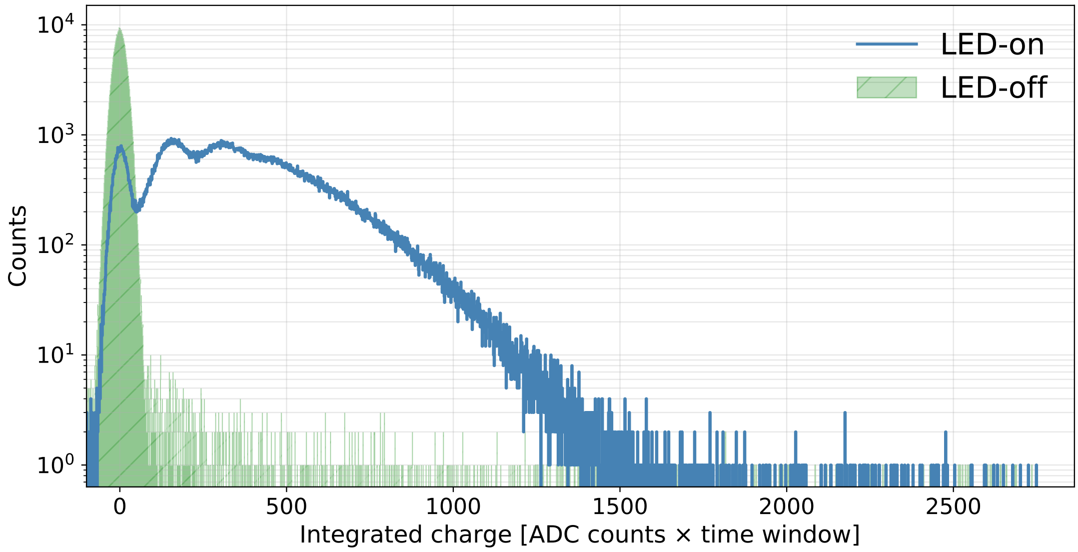

Figure 5.16: Integrated spectra with LED at 1 V (LED-off, green) and 5.9 V (LED-on, blue) for the PMT 300 biased at 1300 V.

PE per trigger to minimise the statistical uncertainties [148]. The light levels in vacuum and nitrogen are thus selected to be 6.5 V for the bottom PMT array and 6 V for the top PMT array, with the exception of a few PMTs[6] that see more light, probably due a fibre bent towards the top. An example of the occupancy and gain calculated during this commissioning stage for all the PMTs is shown in figure 5.17. For the SPE the light levels were set to minimise the presence of double electron peaks, with an occupancy between 0.1 and 0.4 PE per trigger and of 0.2 PE per trigger on average. This corresponds to light levels of around 4.2 V, 4 V and 3.8 V depending on the light distribution and PMT collection, as performed for the gain. Following this study, a HV scan is necessary to study the relation between gain and bias voltage. In this way it is possible to extrapolate the voltage to bias each PMT in such a way to optimise the gain in order to have an SPE acceptance higher than ∼90%. Typically this corresponds to gain values higher than $\sim 2\times 10^6$. These tests need to be repeated once the TPC is filled with xenon. In particular, due to the reflection at the liquid-gas interface, and the value of the light levels is going to change.

The time evolution of the gain in most of the PMTs is expected to be constant or slightly decreasing. In XENON1T it was observed that in some PMTs the gain featured a sharp step-like decrease. This was due to a change in operating condition, such as in PMT HV or an unexpected trip, or during the first radon calibration, due to the high radioactive source injected near some of the PMTs without turning them off (see appendix B). These features were modelled with a Fermi-Dirac function and fit manually. In XENONnT more

---

[6] PMTs 0, 6, 7, 8, 165, 166, 167, 182, 183, 198

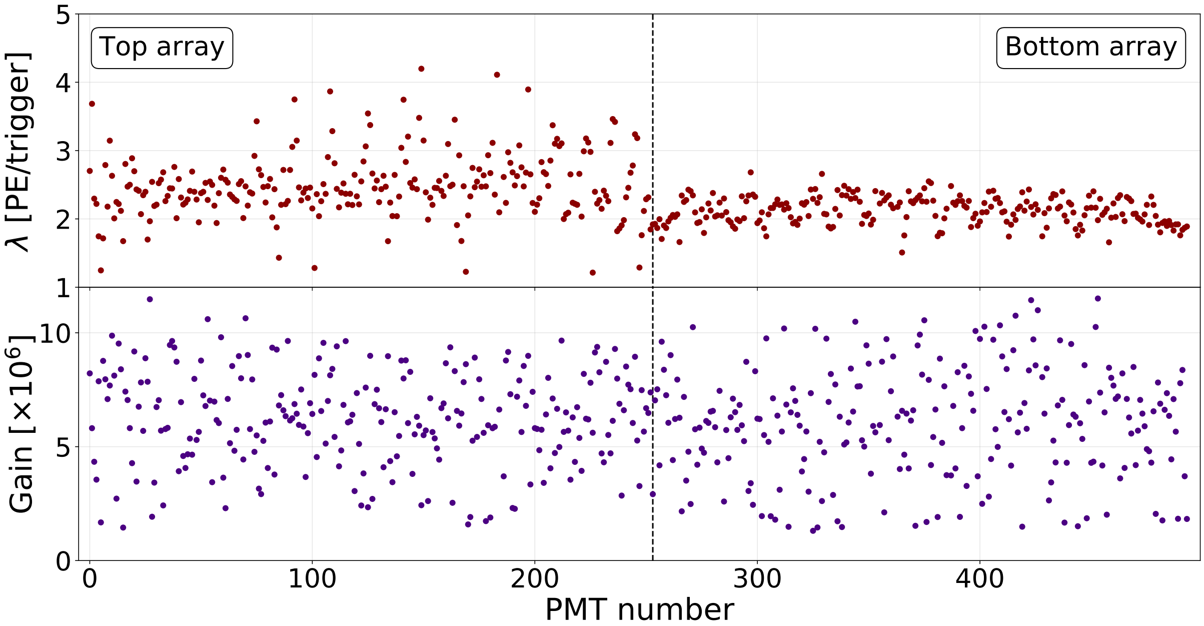

Figure 5.17: Occupancy (top panel) and gain (bottom panel) calculated for the 494 XENONnT PMTs. The PMTs are biased at 1500 V, the light levels used are 6 V for the top PMT array excluding a few PMTs at 4.8 V, and 6.5 V for the bottom PMT array. The vertical dashed line indicates the separation between PMTs in the top and bottom arrays.

communication with the slow control will allow to provide the Unix-time of such events causing the gain drop to improve modelling of the gain time evolution for each PMT.

5.4 Outlook

The XENONnT experiment is currently under commissioning at LNGS. The new TPC is installed in the same place as the previous XENON1T one and several subsystems have been upgraded. The calibration of the photosensors is done similarly to the XENON1T one and reuses part of it. The optical fibres going around and within the TPC are new. Their position was optimised for a homogeneous light collection efficiency, performing optical simulation with GEANT4. The ends of the fibres are stuck into the reflector panels and are located symmetrically with respect to the main axis of the TPC, at two heights, 20 cm and 25 cm below the gate electrode. The fibres were cleaned, prepared for the installation and shipped to LNGS. Here the TPC was assembled in a cleanroom above ground and then it was transported underground to finalise the installation and connections. The first PMT and light calibration commissioning was also done on-site. The 494 PMTs were tested and the DAQ, slow control and LED settings adjusted to allow for remote control operations. The software for the PMT gain calibration was developed using the model independent method. A new *plugin* integrated into the processor allows for more automated data handling and analysis. The working parameters for the PMT and their calibration are being adjusted by the PMT group as the commissioning phase in LXe is still ongoing.

CHAPTER 6

Conclusions

The composition of the Universe in the form of dark matter (DM) and the neutrino nature are two of the main challenges in the panorama of particle physics today. The XENON experiments use dual-phase xenon time projection chambers (TPCs) in order to search for WIMP scatters off xenon nuclei. With the latest XENON1T result, in 278.8 days of data taking, one tonne-year exposure, an electronic recoil background as low as $(82^{+5}_{-3}(\mathrm{syst})\pm3(\mathrm{stat}))\,\mathrm{events}/(\mathrm{t}\cdot\mathrm{yr}\cdot\mathrm{keV_{ee}})$ was achieved in the region $[4.9,\ 40.9]\,\mathrm{keV_{nr}}$. The background-only hypothesis was preferred, and the exclusion limit has a minimum of $4.1\times10^{-47}\,\mathrm{cm}^2$ for $30\,\mathrm{GeV/c^2}$ WIMPs at 90% C.L., the best to date above $6\,\mathrm{GeV/c^2}$. Its successor, the XENONnT experiment, was installed at the beginning of 2020 and is currently under commissioning. It exploits 8.4 t of liquid xenon, of which 5.9 t will be used as target. If no signal will be discovered, the experiment will cover a region down to a cross section of $\sim10^{-48}\,\mathrm{cm}^2$ for the spin-independent (SI) WIMP-nucleon interaction.

At the beginning of my Ph.D. work I was involved with the DM data analysis for the XENON1T SI-WIMP search. Moreover, liquid xenon properties were studied using a small dual-phase TPC at the University of Zurich. The results are published in [150] and additional characterisations are shown in appendix A. However, the main topic of this thesis is the investigation into the possibility to add another fundamental physics channel into the XENON program, and more generally for dual-phase TPCs: the search for $0\nu\beta\beta$ of ^{136}Xe. In parallel, hardware and software work on the photosensors' calibration for the XENONnT detector was also performed, allowing for the first data acquisition with the new detector.

Dual-phase TPCs designed for DM searches are optimised to work in the few keV electron recoil energies. To simultaneously search for DM and ^{136}Xe $0\nu\beta\beta$, several improvements in the MeV energy region need to be made. In XENON1T the main problem affecting the signal at high energies is the non-linearity and distortion due to saturation of the digitisers. A software saturation correction method was implemented into the processor to reconstruct the affected signals. The algorithm to split or cluster different peaks was also refined. The effect of the improvements is observed in the reconstructed energy resolution: a world-record energy resolution in liquid xenon of $\sigma/\mu = (0.80 \pm 0.02)\,\%$ at 2.46 MeV was achieved in XENON1T. The content of this work is published in [109]. The experiment is not competitive with the dedicated double beta experiments due to the background not optimised at the $Q_{\beta\beta}$ of the decay. However, the higher-level analysis for the $0\nu\beta\beta$ search is also performed as a proof of concept for dual-phase TPCs. This opens the path for the next generation experiments, XENONnT and DARWIN, to be competitive with the $0\nu\beta\beta$ dedicated detectors. It is possible thanks to the extensive work conducted on the high-energy signal reconstruction, that covers also the region of interest of the decay. Data selections specifically for the interested energy region were developed and the data Monte Carlo matching was performed between 1600 keV and 3200 keV. The analysis is at the final stage and a sensitivity on the order of $\sim 2\times 10^{24}$ yr is expected for XENON1T, while an order of magnitude more can be achieved by XENONnT. The unblinding will follow in late 2020.

The XENONnT experiment uses 494 PMTs to look for interactions in the TPC. The light calibration for these photosensors is thus crucial. The system is composed of three types of optical fibres to carry the light through the cryogenic system and inside the TPC. Optical simulations were performed to finalise the design of the fibre positions. The fibres were then prepared for the installation. They were installed, together with the field cage, during the assembly and installation campaign at the Laboratori Nazionali del Gran Sasso, Italy, in February/March 2020. The connection of fibres and all the PMTs were made and tested during the first phase of the detector commissioning. To establish the working point of each PMT and monitor its performance, the software framework to process and analyse the LED data for the gain estimation was developed and it is already used for the first XENONnT calibrations. The detector is now filled with liquid xenon and both the calibration system and the software will be routinely used, weekly, throughout the lifetime of the experiment.

Neutrinos and DM are very vibrant research topics. In the next few years, thanks to multi-tonne detectors it will be possible to explore the entire WIMP allowed parameter space down to the neutrino coherent scattering background. The upcoming $0\nu\beta\beta$ decay experiments are going to probe an effective Majorana mass down to 10 meV, covering the parameter space predicted by the inverted ordering. While the development of new reliable technologies will be fundamental to continue investigating the Universe, dual-phase TPCs can expand our understanding in both fields, along with exciting challenges and results.

APPENDIX A

The Xurich-II Dual-Phase TPC

This appendix summarises the work done, at the beginning of my Ph.D. studies, to characterise a small dual-phase TPC and study the liquid xenon properties. The instrumentation and part of the characterisation are reported in [150].

A.1 Detector Characterisation

The Xurich-II experiment, located at the University of Zurich, was built in the context of dark matter search experiments, to study the properties of liquid xenon at low energies and under the effect of different electric fields. It consists of a small dual-phase TPC, 3.1 cm in diameter and 3.1 cm in height, filled with 68 g of xenon and instrumented with two 2-inch, Hamamatsu Photonics R9869 PMTs, one placed at the bottom and one on top to detect the light signals. They have a synthetic silica window and 12 stages amplification to allow for a quantum efficiency of ∼35% at 178 nm. The fields are defined by three electrodes: a grounded gate, a cathode that allows to reach a drift field up to 2 kV/cm and an anode that is able to delimit an extraction field of ∼10 kV/cm. The structure of the cylindrical field cage is made by PTFE and seven copper field shaping rings to maintain the field uniformity. In figure A.1 a picture of the TPC connected to the top flange of the cryostat and a picture of one of the two PMTs are shown. The xenon gas is constantly purified by circulation through a hot metal getter, reaching an electron lifetime of ∼200 μs, ten times larger than the maximum drift time of ∼20 μs. Three capacitive level meters are used to determine the liquid level.

Before the data taking few studies to characterise the detector needs to be carried out. After filling the TPC with liquid xenon, it is necessary to calibrate the level meters to adjust the TPC horizontally and to set the liquid level. To do this the TPC is filled up to the lower common capacitor plate. The level is regulated with a motion feedthrough and

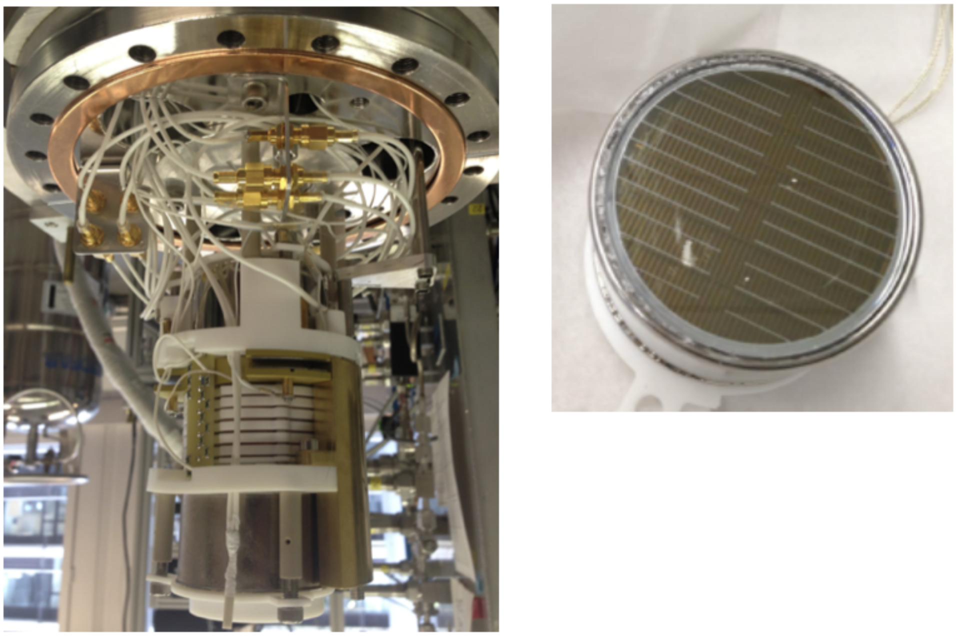

Figure A.1: Left: picture of the Xurich-II TPC connected to the top flange. The PTFE structure of the field cage with the copper rings and the voltage divider are well visible. Right: one of the R9869 PMTs.

increased in step of 125 μm until reaching the saturation point, when the liquid touches the upper plates. On the left of figure A.2, it is shown a plot with the calibration curves of the three level meters after the subtraction of the lower plate value. Once the calibration is done, the liquid level is set at 2 mm above the gate, where the width of the charge signal is minimised. The deadtime of the DAQ is the time the system is unavailable after an event is acquired. It is computed comparing the rate of the acquisition with the frequency of triggered events. Different datasets are acquired using a pulse generator at increasing frequencies. When the rate reaches a plateau it indicates the maximum rate at which the DAQ can work before being saturated. This corresponds to a deadtime of (2.29 ± 0.03) ms.

During the data taking, the stability of the PMTs was monitored using two plastic fibres to shine blue light ($\sim$470 nm). The gain was computed using the model independent method as described in section 5.3.1. In figure A.2 on the right is shown the time evolution of the gain for one of the PMTs with the 5% band computed on the stable period. After a warming up and cooling down cycle the gain showed higher values that stabilised again after about a month. Thus, the evolution is fit with a constant function during detector operations and with an additional third grade polynomial afterward.

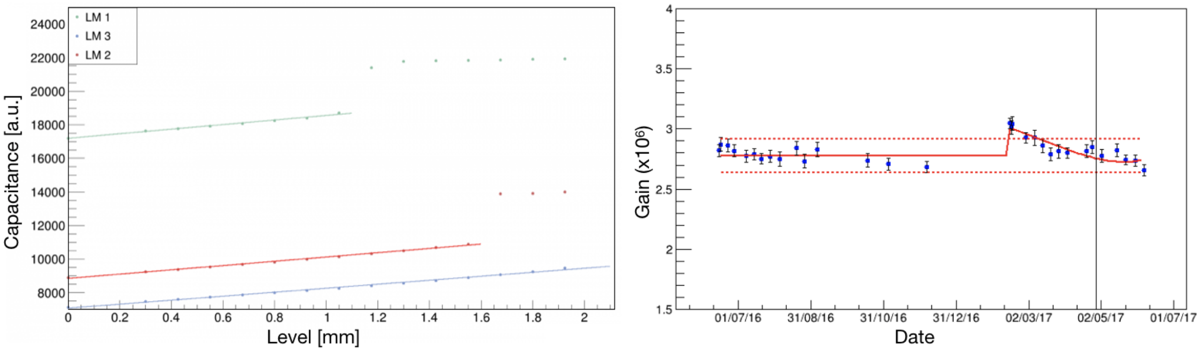

Figure A.2: Left: calibration curves for the three level meters after subtraction of the common plate. Right: time evolution of the gain for the top PMT. The gain of the PMTs was stable during the data taking, the increased values around March 2017 are due to a stabilisation after a warming up and cooling down cycle.

A.2 Measurements with Electronic Recoil Sources

The detector performance (light and charge yield, reconstructed energy, electron drift velocity and electronic recoil band width) is measured at different fields. For this purpose various sources were used. A source of ^{83}Rb is installed into the recirculation gas system and it decays with a half-life of 86.2 days into $^{83\mathrm{m}}$Kr that is used for the calibration. The $^{83\mathrm{m}}$Kr is then uniformly distributed in the TPC and it produces two monoenergetic peaks at 9.4 and 32.1 keV, in the region of interest for our measurements. Thanks to the topology of the signal, the $^{83\mathrm{m}}$Kr population can be easily selected requiring the presence of two S1s and two S2s within a time interval in agreement with the measured half-life of (155±1) ns. An event is shown as an example in figure A.3. The detected signals are corrected taking into account the light distribution along the TPC depth and, for the S2,

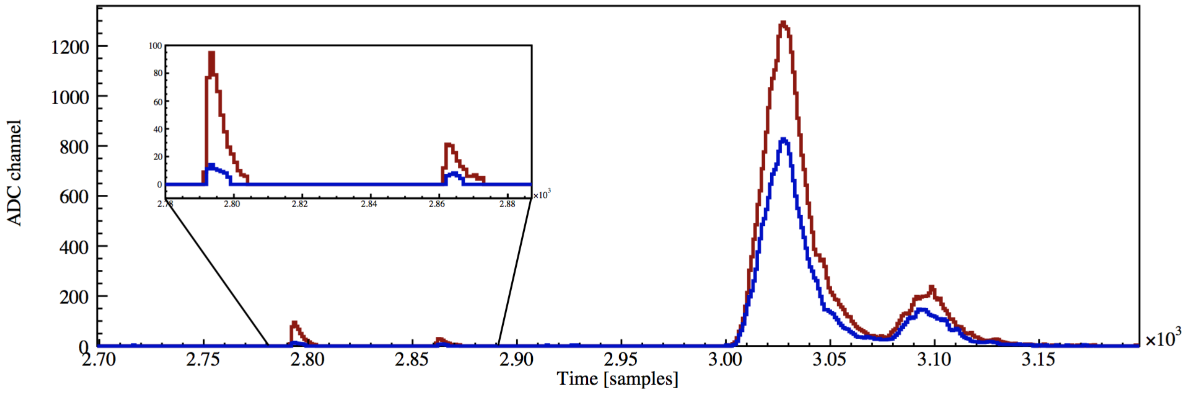

Figure A.3: A $^{83\mathrm{m}}$Kr event detected by Xurich-II, in the bottom (red) and top (blue) PMTs. A zoom on the S1s is shown in the inset on the top left while the S2s are well visible. Figure adapted from [151].

also the electron drift time. The position reconstruction is possible only along the depth of the TPC, so a fiducialisation is applied to exclude the gas region on the top and the bottom edge close to the cathode. This allows us to estimate light and charge yields for the $^{83\mathrm{m}}$Kr monoenergetic peaks. From the light and charge yield anticorrelation in LXe the photon detection efficiency, $g_1 = (0.191 \pm 0.006)$ PE/photon, and the charge amplification gain, $g_2 = (24.4 \pm 0.4)$ PE/electron, can be extracted [150]. With these parameters it is possible to reconstruct the electronic recoil energy of any interaction in the detector. The calibration procedure is similar to what described in sections 2.1 and 3.3, but using a defined monoenergetic line at different fields, as done in [152], instead of several known peaks at different energies and at the same drift field. In particular the light and charge yields for the 32.1 keV $^{83\mathrm{m}}$Kr line and at a drift field of ∼1 kV/cm are 41.4 photons/keV and 28 electrons/keV, respectively. A tail toward low values in the S2 signal distribution was observed due to the missing (x-y) position reconstruction that does not allow to remove the events close to the wall of the TPC where charge accumulation on the PTFE panels can reduce the size of the S2s. Few cuts based on the S2 signal shape (FWHM and its relation with the maximum) were developed to get a cleaner population. From the maximum and minimum of the time delay distribution between S1 and S2 signals it is possible to identify the drift time between gate and cathode. Comparing this with the size of the field cage we can compute the electron drift velocity at different fields. The results obtained with Xurich-II are in agreement with other literature values [150].

The electronic band width has been characterised using an external ^{137}Cs source that provides a continuous spectrum in the low energy region. The band, shown in figure A.4 on the left, is defined by the ratio between the S2 and S1 signals of each interaction. The width is computed binning the distribution along the size of the S1 and computing the 1% and 99% quantiles for each bin. The data were acquired for different drift fields. The

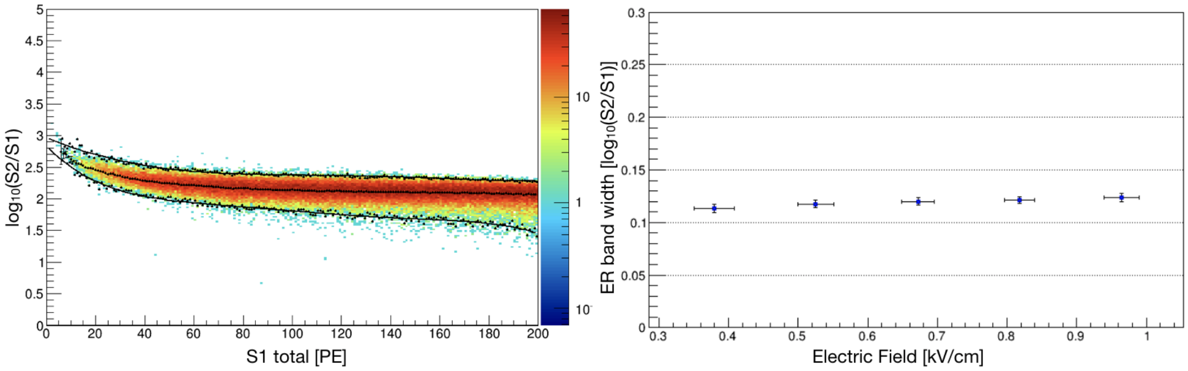

Figure A.4: Right: electronic recoil band from ^{137}Cs with the 1% and 99% quantiles. Right: average electronic recoil width for different drift fields.

Figure A.5: The design of the Xurich-II TPC with the SiPM array on the top.

average electronic recoil band width shows no field dependence as shown on the right of figure A.4. The nuclear recoil characterisation, originally planned to conclude this work, was not possible due to a malfunctioning problem in the D-D neutron generator at the Zurich University.

The characterisation of a stable setup with well known technologies is fundamental to study and compare the performance of a new configuration. Xurich-II has indeed been upgraded with an array of Silicon Photomultipliers (SiPM) replacing the PMT on the top, but keeping the one at the bottom for further comparison. The new design is reported in figure A.5. The upgrade of the Xurich-II detector is included within an R&D program for the DARWIN experiment, and it is the first test of these light detectors in a dual-phase xenon TPC. The upgrade was carried out by other members of the group and it is published in [153].

APPENDIX B

^{220}Rn Calibration: Detector Operation

This appendix describes the study performed to check if a better procedure to acquire ^{220}Rn data was possible, in order to reduce the dead time and thus decrease the time spent for the calibration and increase the exposure. The data used were acquired between August and December 2017, during the SR1. The ^{220}Rn decay chain is shown in figure B.1.

The ^{220}Rn data taking procedure in XENON1T was:

- turn off the PMTs;
- open the valve to inject the source. Beside the main valve there is also a needle valve to adjust the flux injected into the TPC, this latter is hand regulated and thus the ^{220}Rn amount entering in the TPC is not known;
- do not take any data for ∼9 hours due to the high rate of the alpha decays;
- close the valve of the source and take data;
- the procedure of source opening and closing is repeated a few times in order to acquire enough statistics.

After 10.6 hours, the half-life of ^{212}Pb in the chain, the background in the TPC is dominated by the following β-decay with an half-life of 60.5 minutes and the immediate α-decay with an half-life of 300 ns:

$$^{212}\text{Bi} \rightarrow^{212} \text{Po} + \beta^- + \bar{\nu_e} \rightarrow^{208} \text{Pb} + \alpha \tag{B.1}$$

We expect that one event of this type has two S1s, one from the β and one from the α decay. To select this population we can use a timing cut between the first and the second S1 in the event, between 30 ns and 2000 ns. To validate the selection the time

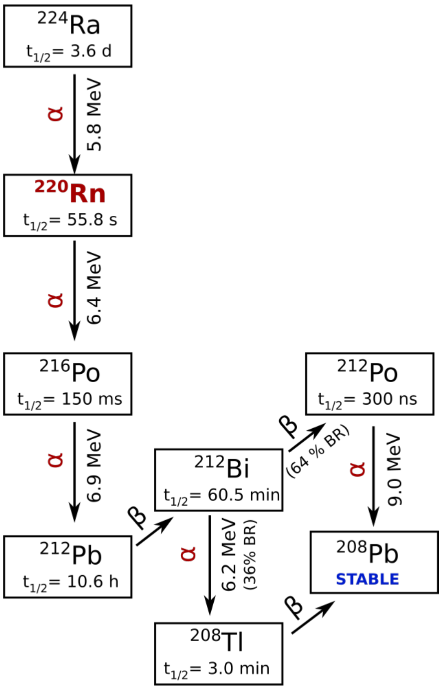

Figure B.1: ^{220}Rn decay chain. Figure from [154].

difference between the S1s was fit with an exponential function that yielded a half-life of (301.3 ± 1.6) ns.

The abundance of an element at time t and step n of the decay chain is given by:

$$N_n(t) = \sum_{i=1}^{n} \left[N_i(0) \times \left(\prod_{j=1}^{n-1} \lambda_j \right) \times \left(\sum_{j=1}^{n} \frac{e^{-\lambda_j t}}{\prod_{p=i,p\neq j}^{n} (\lambda_p - \lambda_j)} \right) \right] \tag{B.2}$$

where $\lambda = \dfrac{1}{T_{1/2}}$ and $N_i(0)$ is the number of counts at time zero for the decay step i. Instead of assuming an initial number of nuclei at time zero, I considered a flux of 40 Hz injected constantly through the needle valve. This function is computed up to $n = 4$ and it is shown in figure B.2. After ∼100 minutes the rate of the α-decay is higher than the threshold to operate safely the PMTs and the DAQ, ∼245 Hz. From an operational point of view it is not feasible to close the valve after 100 minutes as it would require repeating it several times to collect enough statistics for the calibration. Thus the procedure remained unchanged.

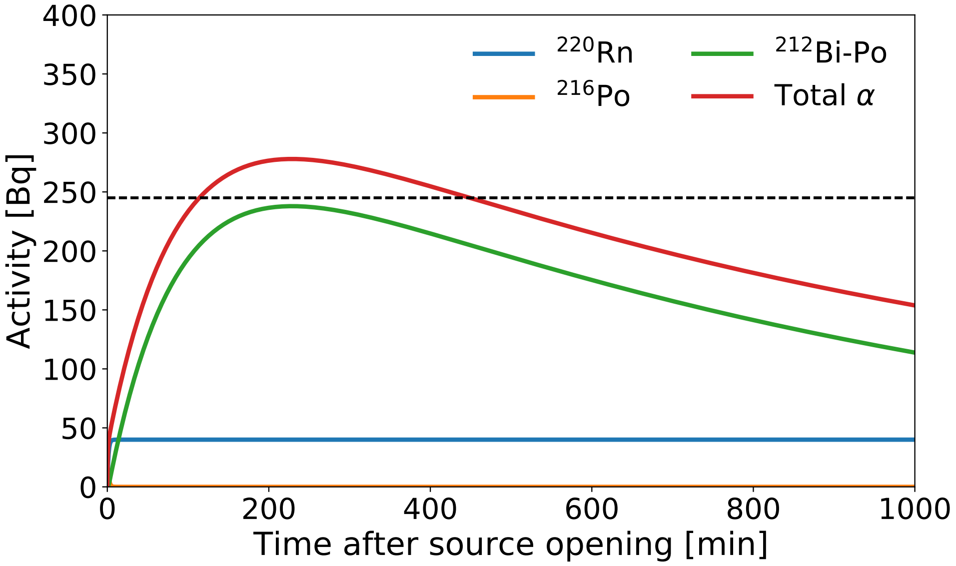

Figure B.2: Simulated rate of α-decays during the ^{220}Rn calibration in XENON1T. The dashed black line is the high-rate threshold for safe operations.

List of Figures

1.1 Galactic rotation curve and a colliding galaxy cluster. 3

1.2 Planck 2018 temperature power spectrum. 4

1.3 Equilibrium and relic abundance of WIMP particles. 6

1.4 Scheme of the methods used for DM search. 7

1.5 Direct detection channels and main current experiments. 8

1.6 WIMP direct detection differential event rate for different target materials. 9

1.7 Upper limits on the SI DM-nucleon cross section as a function of the DM mass. 11

1.8 Neutrino oscillation probability as function of the baseline distance and the neutrino energy 14

1.9 Neutrino mass orderings. 15

1.10 Feynman diagrams and signatures of the double beta decays. 19

1.11 Nuclear mass as a function of the atomic number Z. 20

1.12 Nuclear matrix elements for some of the $0\nu\beta\beta$ decay candidates. 21

1.13 Effective Majorana mass $|m_{\beta\beta}| \equiv |m_{ee}|$ as function of the lightest neutrino. 26

2.1 Working principle of a dual-phase TPC. 32

2.2 Drawing of the XENON1T TPC and pictures of the PMT arrays. 34

2.3 Spatial distributions of XENON1T DM search data. 37

2.4 XENON1T DM search data distributed in (cS1, cS2_b) and (R^2, cS2_b). . . . 37

2.5 XENON1T 90% confidence level upper limit on σ_{SI}. 38

2.6 Schematic view of XENONnT and its subsystems. 41

2.7 CAD rendering of the XENONnT TPC with the PMT arrays in the cryostat. 42

2.8 Projection of the XENONnT sensitivity and discovery power in the search for spin-independent WIMP-nucleon couplings. 44

3.1 One of the first XENON1T events after processing. 46

3.2 Examples of reconstruction of saturated waveforms. 49

3.3 Rate of xenon APs in the five LED datasets used to monitor SR0 and SR1. 50
3.4 Example of a high-energy event induced by a series of Compton scatters in the LXe. 52
3.5 Relative differences in signal size and reconstructed position between *pax_v6.10.1* and *pax_v6.8.0*.. 53
3.6 Topology of the events detected in XENON1T. 54
3.7 Single-site and multi-site background event distributions in SR1. 55
3.8 Examples of two-dimensional rotated Gaussian fit. 56
3.9 Anti-correlation between the measured LY and QY. 57
3.10 Single-site and multi-site electronic recoil energy spectra of background in SR1. 58
3.11 Fit on the ^{214}Bi peaks above 2 MeV. 58
3.12 Measured relative energy resolution for SS and MS events. 59
3.13 Measured relative energy resolution for SS events during SR2 tests. 61

4.1 *PosDiff* cut definition and events removed by the cut. 66
4.2 Stopping power and track length for electrons in LXe. 68
4.3 *S2Width* cut definition extended to high energies. 68
4.4 Blinded and sidebands regions. 69
4.5 Background distribution in a 9×9 grid and relative figure of merit. 70
4.6 Maximisation of the fiducial volume. 71
4.7 Total acceptance for the $0\nu\beta\beta$ decay selections. 73
4.8 Simulated intrinsic background between 1600 keV and 3200 keV. 75
4.9 Simulated external background between 1600 keV and 3200 keV. 76
4.10 Data MonteCarlo matching fit between 1600 keV and 3200 keV. 77
4.11 Empirical sensitivity to the $0\nu\beta\beta$ decay for XENON1T and XENONnT. . 79

5.1 Light calibration system of XENONnT. 81
5.2 Simulated LCE for the final configuration of the fibers in XENONnT. . . . 83
5.3 Radial position of the fibers for 30° and 60° relative rotation. 85
5.4 Example of LCE in case of 30° rotation and with two sets of fibers broken. 86
5.5 Fibers during the preparation for the installation. 87
5.6 Pictures of the bottom PMT array and field cage copper wires during the installation. 90
5.7 Pictures of the resistor chains and field cage copper rings during the installation. 91

5.8 Pictures of the assembled TPC aboveground and during the lifting underground. 92
5.9 Pictures of the connected cables on the top of the bell and scheme of the final working fibers. 93
5.10 The TPC installed underground. 94
5.11 Connections between the PMTs, the HV and the DAQ. 96
5.12 Picture of the pulse generator, the LEDs and the first signals. 97
5.13 PMT map at the end of the first XENONnT commissioning phase. 98
5.14 Gain computation procedure in XENON1T and XENONnT. 101
5.15 LED calibration aquisition window. 102
5.16 Example of LED-off and LED-on integrated spectra. 103
5.17 Occupancy and gain calculated for the 494 XENONnT PMTs. 104

A.1 The Xurich-II detector. 110
A.2 Xurich-II characterisation: liquid level and gain. 111
A.3 Waveform of a ^{83m}Kr event detected by Xurich-II. 111
A.4 Electronic recoil band width measured in Xurich-II. 112
A.5 Design of the Xurich-II TPC upgraded with a SiPM array. 113

B.1 ^{220}Rn decay chain. 115
B.2 Simulated rate of α-decays during the ^{220}Rn calibration in XENON1T. . . 116

List of Tables

1.1 Neutrino oscillation parameters summary. 16
1.2 Double beta decay candidates with Q-value above 2 MeV 22
1.3 Some of the leading present, planned and future experiments for $0\nu\beta\beta$ search. 25

2.1 Isotope components of natural xenon. 29
2.2 The XENON1T ER background rates in (1,12) $\mathrm{keV_{ee}}$ and in 1.3 t fiducial volume. 36
2.3 Best fit expected event counts with 278.8 days livetime in the 1.3 t fiducial mass in the NR signal reference region. 38
2.4 Electron drift velocity in LXe for different cathode voltages. 39

3.1 Mono-energetic lines used for the electronic recoil energy calibration. . . . 55

4.1 List of event selections used for the $0\nu\beta\beta$ decay search with their brief description. 65
4.2 Values used to compute the empirical sensitivity in XENON1T and XENONnT. 78

5.1 Characteristics of optical fibers in XENONnT. 82
5.2 Vertical position and transparency of the main components of the XENONnT TPC. 83
5.3 Comparison of the LCE on the PMT arrays. 84
5.4 Contamination measured with the ICP-MS in the PMMA fibers. 87
5.5 Type-3 fibers properties. 88

Bibliography

[1] P. A. Zyla et al. (Particle Data Group). "Review of Particle Physics". In: *Progress of Theoretical and Experimental Physics* 2020.8 (Aug. 2020). ISSN: 2050-3911.

[2] F. Zwicky. "Die Rotverschiebung von extragalaktischen Nebeln". In: *Helvetica Physica Acta* 6 (1933), pp. 110–127.

[3] V. C. Rubin, Jr. Ford W. K., and N. Thonnard. "Extended rotation curves of high-luminosity spiral galaxies. IV. Systematic dynamical properties, Sa through Sc". In: *Astrophys. J. Lett.* 225 (1978), pp. L107–L111.

[4] M. Persic, P. Salucci, and F. Stel. "The Universal rotation curve of spiral galaxies: 1. The Dark matter connection". In: *Mon. Not. Roy. Astron. Soc.* 281 (1996), p. 27.

[5] A. Refregier. "Weak Gravitational Lensing by Large-Scale Structure". In: *Annual Review of Astronomy and Astrophysics* 41.1 (2003), 645–668. ISSN: 1545-4282.

[6] G. D'Amico, M. Kamionkowski, and K. Sigurdson. *Dark Matter Astrophysics.* 2009. arXiv: `0907.1912`.

[7] M. Roos. *Dark Matter: The evidence from astronomy, astrophysics and cosmology.* 2010. arXiv: `1001.0316`.

[8] D. Clowe et al. "A Direct Empirical Proof of the Existence of Dark Matter". In: *The Astrophysical Journal* 648.2 (2006), pp. L109–L113.

[9] *The MOSFIRE Deep Evolution Field Survey.* URL: `http://mosdef.astro.berkeley.edu/for-the-public/public/galaxy-masses/`.

[10] D. Harvey et al. "The nongravitational interactions of dark matter in colliding galaxy clusters". In: *Science* 347.6229 (2015), 1462–1465. ISSN: 1095-9203.

[11] W. Hu and S. Dodelson. "Cosmic Microwave Background Anisotropies". In: *Annual Review of Astronomy and Astrophysics* 40.1 (2002), 171–216. ISSN: 1545-4282.

[12] D. N. Spergel et al. "Three-Year Wilkinson Microwave Anisotropy Probe (WMAP) Observations: Implications for Cosmology". In: *The Astrophysical Journal Supplement Series* 170.2 (2007), pp. 377–408.

[13] Planck Collaboration et al. *Planck 2018 results. VI. Cosmological parameters.* 2018. arXiv: `1807.06209`.

[14] E. W. Kolb and M. S. Turner. *The Early Universe.* Vol. 69. 1990. ISBN: 978-0-201-62674-2.

[15] R.D. Peccei and H.R. Quinn. "CP Conservation in the Presence of Instantons". In: *Phys. Rev. Lett.* 38 (1977), pp. 1440–1443.

[16] P. W. Graham et al. "Experimental Searches for the Axion and Axion-Like Particles". In: *Annual Review of Nuclear and Particle Science* 65.1 (2015), pp. 485–514.

[17] R. Battesti et al. "Axion Searches in the Past, at Present, and in the Near Future". In: *Axions: Theory, Cosmology, and Experimental Searches.* Ed. by Markus Kuster, Georg Raffelt, and Berta Beltrán. Berlin, Heidelberg: Springer Berlin Heidelberg, 2008, pp. 199–237. ISBN: 978-3-540-73518-2.

[18] G. Jungman, M. Kamionkowski, and K. Griest. "Supersymmetric dark matter". In: *Physics Reports* 267.5 (1996), pp. 195 –373. ISSN: 0370-1573.

[19] S. Profumo, L. Giani, and O. F. Piattella. *An Introduction to Particle Dark Matter.* 2019. arXiv: `1910.05610`.

[20] O. Adriani et al. "An anomalous positron abundance in cosmic rays with energies 1.5–100 GeV". In: *Nature* 458.7238 (2009), 607–609. ISSN: 1476-4687.

[21] S. Profumo. "Dissecting cosmic-ray electron-positron data with Occam's razor: the role of known pulsars". In: *Open Physics* 10.1 (2012), 1–31. ISSN: 2391-5471.

[22] A. A. Abdo et al. "Measurement of the Cosmic Ray $e^+ + e^-$ Spectrum from 20 GeV to 1 TeV with the Fermi Large Area Telescope". In: *Phys. Rev. Lett.* 102 (18 2009), p. 181101.

[23] M. Aguilar et al. "First Result from the Alpha Magnetic Spectrometer on the International Space Station: Precision Measurement of the Positron Fraction in Primary Cosmic Rays of 0.5–350 GeV". In: *Phys. Rev. Lett.* 110 (14 2013), p. 141102.

[24] M.L. Ahnen et al. "Indirect dark matter searches in the dwarf satellite galaxy Ursa Major II with the MAGIC telescopes". In: *Journal of Cosmology and Astroparticle Physics* 2018.03 (2018), 009–009. ISSN: 1475-7516.

[25] H. Abdallah et al. “Search for dark matter signals towards a selection of recently detected DES dwarf galaxy satellites of the Milky Way with H.E.S.S.” In: *Phys. Rev. D* 102 (6 2020), p. 062001.

[26] The Cherenkov Telescope Array Consortium et al. *Sensitivity of the Cherenkov Telescope Array for probing cosmology and fundamental physics with gamma-ray propagation.* 2020. arXiv: `2010.01349`.

[27] J. M. Gaskins. “A review of indirect searches for particle dark matter”. In: *Contemporary Physics* 57.4 (2016), 496–525. ISSN: 1366-5812.

[28] J. Conrad and O. Reimer. “Indirect dark matter searches in gamma and cosmic rays”. In: *Nature Physics* 13.3 (2017), 224–231. ISSN: 1745-2481.

[29] F. Kahlhoefer. “Review of LHC dark matter searches”. In: *International Journal of Modern Physics A* 32.13 (2017), p. 1730006. ISSN: 1793-656X.

[30] O. Buchmueller, C. Doglioni, and L. Wang. “Search for dark matter at colliders”. In: *Nature Physics* 13.3 (2017), 217–223. ISSN: 1745-2481.

[31] M. Aaboud et al. “Search for dark matter at $\sqrt{s} = 13$ TeV in final states containing an energetic photon and large missing transverse momentum with the ATLAS detector”. In: *The European Physical Journal C* 77.6 (2017). ISSN: 1434-6052.

[32] A. M. Sirunyan et al. “Search for dark matter particles produced in association with a Higgs boson in proton-proton collisions at $\sqrt{\mathrm{s}} = 13$ TeV”. In: *Journal of High Energy Physics* 2020.3 (2020). ISSN: 1029-8479.

[33] T. Marrodán Undagoitia and L. Rauch. “Dark matter direct-detection experiments”. In: *Journal of Physics G: Nuclear and Particle Physics* 43.1 (2015), p. 013001.

[34] M. Schumann. “Direct detection of WIMP dark matter: concepts and status”. In: *Journal of Physics G: Nuclear and Particle Physics* 46.10 (2019), p. 103003.

[35] J. I. Read. “The local dark matter density”. In: *Journal of Physics G: Nuclear and Particle Physics* 41.6 (2014), p. 063101. ISSN: 1361-6471.

[36] M. C. Smith et al. “The RAVE survey: constraining the local Galactic escape speed”. In: *Monthly Notices of the Royal Astronomical Society* 379.2 (2007), 755–772. ISSN: 1365-2966.

[37] P. Toivanen et al. “Large-scale shell-model calculations of elastic and inelastic scattering rates of lightest supersymmetric particles (LSP) on I-127, Xe-129, Xe-131, and Cs-133 nuclei”. In: *Phys. Rev. C* 79 (2009), p. 044302.

[38] P. Klos et al. “Large-scale nuclear structure calculations for spin-dependent WIMP scattering with chiral effective field theory currents”. In: *Phys. Rev. D* 88 (8 2013), p. 083516.

[39] R. Bernabei et al. “First model independent results from DAMA/LIBRA-phase2”. In: *Nuclear Physics and Atomic Energy* 19.4 (2018), 307–325. ISSN: 2074-0565.

[40] M. Antonello et al. “The SABRE project and the SABRE Proof-of-Principle”. In: *The European Physical Journal C* 79.4 (2019). ISSN: 1434-6052.

[41] R. Agnese et al. “Results from the Super Cryogenic Dark Matter Search Experiment at Soudan”. In: *Phys. Rev. Lett.* 120 (6 2018), p. 061802.

[42] Q. Arnaud et al. “Optimizing EDELWEISS detectors for low-mass WIMP searches”. In: *Phys. Rev. D* 97 (2 2018), p. 022003.

[43] A. H. Abdelhameed et al. “First results from the CRESST-III low-mass dark matter program”. In: *Phys. Rev. D* 100 (10 2019), p. 102002.

[44] A. Aguilar-Arevalo et al. “Constraints on Light Dark Matter Particles Interacting with Electrons from DAMIC at SNOLAB”. In: *Phys. Rev. Lett.* 123 (18 2019), p. 181802.

[45] C. Amole et al. “Dark matter search results from the complete exposure of the PICO-60 C_3F_8 bubble chamber”. In: *Phys. Rev. D* 100 (2 2019), p. 022001.

[46] K. Abe et al. “A direct dark matter search in XMASS-I”. In: *Physics Letters B* 789 (2019), pp. 45 –53. ISSN: 0370-2693.

[47] R. Ajaj et al. “Search for dark matter with a 231-day exposure of liquid argon using DEAP-3600 at SNOLAB”. In: *Phys. Rev. D* 100 (2 2019), p. 022004.

[48] D. S. Akerib et al. “The Large Underground Xenon (LUX) Experiment”. In: *Nucl. Instrum. Meth.* A704 (2013), pp. 111–126.

[49] D. S. Akerib et al. “Results from a Search for Dark Matter in the Complete LUX Exposure”. In: *Phys. Rev. Lett.* 118 (2 2017), p. 021303.

[50] E. Aprile et al. “The XENON1T Dark Matter Experiment”. In: *Eur. Phys. J.* C77.12 (2017), p. 881.

[51] E. Aprile et al. “Dark Matter Search Results from a One Ton-Year Exposure of XENON1T”. In: *Phys. Rev. Lett.* 121 (11 2018), p. 111302.

[52] P. Agnes et al. “DarkSide-50 532-day dark matter search with low-radioactivity argon”. In: *Phys. Rev. D* 98 (10 2018), p. 102006.

[53] J. Aalbers et al. “DARWIN: towards the ultimate dark matter detector”. In: *JCAP* 1611 (2016), p. 017.

[54] E. Baracchini et al. “A 1 m3 Gas Time Projection Chamber with Optical Readout for Directional Dark Matter Searches: the CYGNO Experiment”. In: *2019 IEEE Nuclear Science Symposium and Medical Imaging Conference (NSS/MIC)* (2019).

[55] S. E. Vahsen et al. *CYGNUS: Feasibility of a nuclear recoil observatory with directional sensitivity to dark matter and neutrinos*. 2020. arXiv: `2008.12587`.

[56] F. Reines and C. L. Cowan. “The neutrino”. In: *Nature* 178 (1956), pp. 446–449.

[57] C. L. Cowan et al. “Detection of the Free Neutrino: a Confirmation”. In: *Science* 124.3212 (1956), pp. 103–104. ISSN: 0036-8075.

[58] B. Pontecorvo. “Inverse beta processes and nonconservation of lepton charge”. In: *Sov. Phys. JETP* 7 (1958), pp. 172–173.

[59] R. Davis, D. S. Harmer, and K. C. Hoffman. “Search for Neutrinos from the Sun”. In: *Phys. Rev. Lett.* 20 (21 1968), pp. 1205–1209.

[60] J. N. Abdurashitov et al. “Solar neutrino flux measurements by the Soviet-American gallium experiment (SAGE) for half the 22-year solar cycle”. In: *Journal of Experimental and Theoretical Physics* 95.2 (2002), 181–193.

[61] M. Altmann et al. “Complete results for five years of GNO solar neutrino observations”. In: *Physics Letters B* 616.3 (2005), pp. 174 –190. ISSN: 0370-2693.

[62] S.P. Mikheyev and A.Yu. Smirnov. “Resonant neutrino oscillations in matter”. In: *Progress in Particle and Nuclear Physics* 23 (1989), pp. 41 –136. ISSN: 0146-6410.

[63] L. Wolfenstein. “Neutrino oscillations in matter”. In: *Phys. Rev. D* 17 (9 1978), pp. 2369–2374.

[64] Y. Fukuda et al. “Evidence for Oscillation of Atmospheric Neutrinos”. In: *Phys. Rev. Lett.* 81 (8 1998), pp. 1562–1567.

[65] Q. R. Ahmad et al. “Direct Evidence for Neutrino Flavor Transformation from Neutral-Current Interactions in the Sudbury Neutrino Observatory”. In: *Phys. Rev. Lett.* 89 (1 2002), p. 011301.

[66] OPERA Collaboration, N. Agafonova, et al. “Observation of tau neutrino appearance in the CNGS beam with the OPERA experiment”. In: *Progress of Theoretical and Experimental Physics* 2014.10 (Oct. 2014). ISSN: 2050-3911.

[67] K. Abe et al. “Indication of Electron Neutrino Appearance from an Accelerator-Produced Off-Axis Muon Neutrino Beam”. In: *Phys. Rev. Lett.* 107 (4 2011), p. 041801.

[68] K. Abe et al. “Observation of Electron Neutrino Appearance in a Muon Neutrino Beam”. In: *Phys. Rev. Lett.* 112 (6 2014), p. 061802.

[69] L. Chau and W. Keung. “Comments on the Parametrization of the Kobayashi-Maskawa Matrix”. In: *Phys. Rev. Lett.* 53 (19 1984), pp. 1802–1805.

[70] P. Hernandez. *Neutrino Physics.* 2017. arXiv: `1708.01046`.

[71] P. F. de Salas et al. *2020 Global reassessment of the neutrino oscillation picture.* 2020. arXiv: `2006.11237`.

[72] S. M. Bilenky and C. Giunti. “Neutrinoless double-beta decay: A probe of physics beyond the Standard Model”. In: *International Journal of Modern Physics A* 30.04n05 (2015), p. 1530001. ISSN: 1793-656X.

[73] M. J. Dolinski, A. W.P. Poon, and W. Rodejohann. “Neutrinoless Double-Beta Decay: Status and Prospects”. In: *Ann. Rev. Nucl. Part. Sci.* 69 (2019), pp. 219–251.

[74] R. Saakyan. “Two-Neutrino Double-Beta Decay”. In: *Annual Review of Nuclear and Particle Science* 63.1 (2013), pp. 503–529.

[75] S. Dell’Oro et al. “Neutrinoless Double Beta Decay: 2015 Review”. In: *Advances in High Energy Physics* 2016 (2016), 1–37. ISSN: 1687-7365.

[76] A. B. Balantekin. “Fundamentals in Nuclear Physics: From Nuclear Structure to Cosmology”. In: *Physics Today* 59.6 (2006), pp. 62–64.

[77] J. Kotila and F. Iachello. “Phase-space factors for double-β decay”. In: *Phys. Rev. C* 85 (3 2012), p. 034316.

[78] E. Caurier et al. “The shell model as a unified view of nuclear structure”. In: *Reviews of Modern Physics* 77.2 (2005), 427–488. ISSN: 1539-0756.

[79] F. Šimkovic et al. “$0\nu\beta\beta$ and $2\nu\beta\beta$ nuclear matrix elements, quasiparticle random-phase approximation, and isospin symmetry restoration”. In: *Phys. Rev. C* 87 (4 2013), p. 045501.

[80] F. Iachello and A. Arima. *The Interacting Boson Model.* Cambridge Monographs on Mathematical Physics. Cambridge University Press, 1987.

[81] T. R. Rodríguez and G. Martínez-Pinedo. “Energy Density Functional Study of Nuclear Matrix Elements for Neutrinoless $\beta\beta$ Decay”. In: *Phys. Rev. Lett.* 105 (25 2010), p. 252503.

[82] J. Engel and J. Menéndez. “Status and future of nuclear matrix elements for neutrinoless double-beta decay: a review”. In: *Reports on Progress in Physics* 80.4 (2017), p. 046301. ISSN: 1361-6633.

[83] K. Zuber. “Neutrinoless double beta decay”. In: *Pramana* 79.4 (2012), 781–791. ISSN: 0973-7111.

[84] E.L. Fireman. “A measurement of the half-life of double beta-decay from (50)Sn-124”. In: *Phys. Rev.* 75 (1949), pp. 323–324.

[85] M. G. Inghram and J. H. Reynolds. “Double Beta-Decay of Te^{130}”. In: *Phys. Rev.* 78 (6 1950), pp. 822–823.

[86] E. Fiorini et al. “A Search for Lepton Nonconservation in Double Beta Decay With a Germanium Detector”. In: *Phys. Lett. B* 25 (1967), pp. 602–603.

[87] S. R. Elliott, A. A. Hahn, and M. K. Moe. “Direct evidence for two-neutrino double-beta decay in $^{82}\mathrm{Se}$”. In: *Phys. Rev. Lett.* 59 (18 1987), pp. 2020–2023.

[88] O. Cremonesi and M. Pavan. “Challenges in Double Beta Decay”. In: *Adv. High Energy Phys.* 2014 (2014), p. 951432.

[89] M. Agostini et al. “Probing Majorana neutrinos with double-β decay”. In: *Science* 365.6460 (2019), 1445–1448. ISSN: 1095-9203.

[90] S. I. Alvis et al. “Search for neutrinoless double-β decay in $^{76}\mathrm{Ge}$ with 26 kg yr of exposure from the Majorana Demonstrator”. In: *Phys. Rev. C* 100 (2 2019), p. 025501.

[91] V. D’Andrea. “Neutrinoless Double Beta Decay Search with $^{76}\mathrm{Ge}$: Status and Prospect with LEGEND”. In: *54th Rencontres de Moriond on Electroweak Interactions and Unified Theories (Moriond EW 2019) La Thuile, Italy, March 16-23, 2019.* 2019.

[92] D. Q. Adams et al. “Improved Limit on Neutrinoless Double-Beta Decay in $^{130}\mathrm{Te}$ with CUORE”. In: *Phys. Rev. Lett.* 124 (12 2020), p. 122501.

[93] The CUPID Interest Group. *CUPID pre-CDR.* 2019. arXiv: `1907.09376`.

[94] G. Anton et al. “Search for Neutrinoless Double-β Decay with the Complete EXO-200 Dataset”. In: *Phys. Rev. Lett.* 123 (16 2019), p. 161802.

[95] F. Monrabal et al. “The NEXT White (NEW) detector”. In: *Journal of Instrumentation* 13.12 (2018), P12010–P12010.

[96] nEXO Collaboration, S. Al Kharusi, et al. *nEXO Pre-Conceptual Design Report*. 2018. arXiv: 1805.11142.

[97] C. Adams et al. *Sensitivity of a tonne-scale NEXT detector for neutrinoless double beta decay searches*. 2020. arXiv: 2005.06467.

[98] A. Gando et al. “Search for Majorana Neutrinos Near the Inverted Mass Hierarchy Region with KamLAND-Zen”. In: *Phys. Rev. Lett.* 117 (8 2016), p. 082503.

[99] A. Giuliani et al. *Double Beta Decay APPEC Committee Report*. 2019. arXiv: 1910.04688.

[100] F. Agostini et al. “Sensitivity of the DARWIN observatory to the neutrinoless double beta decay of ^{136}Xe”. In: *Eur. Phys. J. C* 80.9 (2020), p. 808.

[101] M. Schumann. “Dark matter 2014”. In: *EPJ web of conferences*. Vol. 96. EDP Sciences. 2015, p. 01027.

[102] E. Aprile et al. “Design and performance of the XENON10 dark matter experiment”. In: *Astroparticle Physics* 34 (Apr. 2011), pp. 679–698.

[103] J. Angle et al. “First Results from the XENON10 Dark Matter Experiment at the Gran Sasso National Laboratory”. In: *Phys. Rev. Lett.* 100 (2 2008), p. 021303.

[104] J. Angle et al. “Limits on Spin-Dependent WIMP-Nucleon Cross Sections from the XENON10 Experiment”. In: *Phys. Rev. Lett.* 101.9 (2008). ISSN: 1079-7114.

[105] Xenon100 Collaboration et al. “The XENON100 dark matter experiment”. In: *Astroparticle Physics* 35 (Apr. 2012), pp. 573–590.

[106] E. Aprile et al. “XENON100 dark matter results from a combination of 477 live days”. In: *Phys. Rev. D* 94 (12 2016), p. 122001.

[107] *WebElements*. URL: `https://www.webelements.com/xenon/isotopes.html`.

[108] C. E. Dahl. “The physics of background discrimination in liquid xenon, and first results from Xenon10 in the hunt for WIMP dark matter”. PhD thesis. Princeton U., 2009. URL: `http://inspirehep.net/record/1374815/files/E.Dahlthesis.pdf`.

[109] E. Aprile et al. “Energy resolution and linearity of XENON1T in the MeV energy range”. In: *Eur. Phys. J. C* 80.8 (2020), p. 785.

[110] E. Aprile et al. “Conceptual design and simulation of a water Cherenkov muon veto for the XENON1T experiment”. In: *Journal of Instrumentation* 9.11 (2014), P11006–P11006. ISSN: 1748-0221.

[111] E. Aprile et al. “The XENON1T dark matter experiment”. In: *Eur. Phys. J. C* 77.12 (2017), p. 881.

[112] E. Aprile et al. “Lowering the radioactivity of the photomultiplier tubes for the XENON1T dark matter experiment”. In: *The European Physical Journal C* 75.11 (2015). ISSN: 1434-6052.

[113] E. Aprile et al. “XENON1T dark matter data analysis: Signal reconstruction, calibration, and event selection”. In: *Phys. Rev. D* 100 (5 2019), p. 052014.

[114] P. Barrow et al. “Qualification Tests of the R11410-21 Photomultiplier Tubes for the XENON1T Detector”. In: *JINST* 12.01 (2017), P01024.

[115] E. Aprile et al. “The XENON1T Data Acquisition System”. In: *JINST* 14.07 (2019), P07016.

[116] E. Aprile et al. “First Dark Matter Search Results from the XENON1T Experiment”. In: *Phys. Rev. Lett.* 119 (18 2017), p. 181301.

[117] E. Aprile et al. “XENON1T dark matter data analysis: Signal and background models and statistical inference”. In: *Phys. Rev. D* 99 (11 2019), p. 112009.

[118] E. Aprile et al. “Constraining the Spin-Dependent WIMP-Nucleon Cross Sections with XENON1T”. In: *Phys. Rev. Lett.* 122 (14 2019), p. 141301.

[119] E. Aprile et al. “First Results on the Scalar WIMP-Pion Coupling, Using the XENON1T Experiment”. In: *Phys. Rev. Lett.* 122 (7 2019), p. 071301.

[120] E. Aprile et al. “Search for Light Dark Matter Interactions Enhanced by the Migdal Effect or Bremsstrahlung in XENON1T”. In: *Phys. Rev. Lett.* 123 (24 2019), p. 241803.

[121] E. Aprile et al. “Light Dark Matter Search with Ionization Signals in XENON1T”. In: *Phys. Rev. Lett.* 123 (25 2019), p. 251801.

[122] E. Aprile et al. “Excess electronic recoil events in XENON1T”. In: *Phys. Rev. D* 102 (7 2020), p. 072004.

[123] E. Aprile et al. “Observation of two-neutrino double electron capture in ^{124}Xe with XENON1T”. In: *Nature* 568.7753 (2019), pp. 532–535.

[124] E. Aprile et al. “Removing krypton from xenon by cryogenic distillation to the ppq level”. In: *The European Physical Journal C* 77.5 (2017). ISSN: 1434-6052.

[125] E. Aprile et al. “XENONnT Technical Design Report”. In: (2018). URL: `https://xe1t-wiki.lngs.infn.it/lib/exe/fetch.php?media=xenon:xenonnt:doc:xenonnt-tdr.pdf`.

[126] E. Aprile et al. *Projected WIMP Sensitivity of the XENONnT Dark Matter Experiment.* 2020. arXiv: `2007.08796`.

[127] S. Agostinelli et al. “GEANT4: A Simulation toolkit”. In: *Nucl. Instrum. Meth. A* 506 (2003), pp. 250–303.

[128] B. Lenardo et al. “A Global Analysis of Light and Charge Yields in Liquid Xenon”. In: *IEEE Transactions on Nuclear Science* 62.6 (2015), pp. 3387–3396.

[129] E. Aprile et al. “Physics reach of the XENON1T dark matter experiment.” In: *Journal of Cosmology and Astroparticle Physics* 2016.04 (2016), pp. 027–027.

[130] *The pax data processor v6.8.0.* Version 6.8.0. Mar. 2018. DOI: `10.5281/zenodo.1195785`. URL: `https://doi.org/10.5281/zenodo.1195785`.

[131] G F Knoll. *Radiation detection and measurement; 4th ed.* New York, NY: Wiley, 2010. URL: `https://cds.cern.ch/record/1300754`.

[132] M. Abadi et al. *TensorFlow: Large-Scale Machine Learning on Heterogeneous Systems.* Software available from tensorflow.org. 2015. URL: `http://tensorflow.org/`.

[133] *Lund/LBNL Nuclear Data Search.* URL: `http://nucleardata.nuclear.lu.se/toi/`.

[134] D. S. Akerib et al. “Signal yields, energy resolution, and recombination fluctuations in liquid xenon”. In: *Phys. Rev. D* 95 (1 2017), p. 012008.

[135] E. Aprile et al. “The XENON100 dark matter experiment”. In: *Astropart. Phys.* 35.9 (2012), 573–590. ISSN: 0927-6505.

[136] K. Ni et al. “Searching for neutrino-less double beta decay of ^{136}Xe with PandaX-II liquid xenon detector”. In: *Chin. Phys.* C43.11 (2019), p. 113001.

[137] M. Szydagis et al. *NESTCollaboration/nest: New, flexible LXe NR yields and resolution model + G4 improvements + linear Noise + much more.* Version v2.0.1. Aug. 2019.

[138] P. Sorensen. “Anisotropic diffusion of electrons in liquid xenon with application to improving the sensitivity of direct dark matter searches”. In: *Nuclear Instruments and Methods in Physics Research Section A: Accelerators, Spectrometers, Detectors and Associated Equipment* 635.1 (2011), 41–43. ISSN: 0168-9002.

[139] *Stopping-power and range tables for electrons.* URL: https://physics.nist.gov/PhysRefData/Star/Text/ESTAR.html.

[140] C. Wittweg. “Thesis in preparation”. PhD thesis. Universität Münster.

[141] J. B. Albert et al. “Improved measurement of the $2\nu\beta\beta$ half-life of ^{136}Xe with the EXO-200 detector”. In: *Phys. Rev. C* 89 (1 2014), p. 015502.

[142] J. Menéndez et al. “Disassembling the nuclear matrix elements of the neutrinoless $\beta\beta$ decay”. In: *Nuclear Physics A* 818.3-4 (2009), 139–151. ISSN: 0375-9474.

[143] P. Sorensen and K. Kamdin. “Two distinct components of the delayed single electron noise in liquid xenon emission detectors”. In: *Journal of Instrumentation* 13.02 (2018), P02032–P02032.

[144] P. Sorensen. *Electron train backgrounds in liquid xenon dark matter search detectors are indeed due to thermalization and trapping.* 2017. arXiv: 1702.04805.

[145] E.H. Bellamy et al. “Absolute calibration and monitoring of a spectrometric channel using a photomultiplier”. In: *Nuclear Instruments and Methods in Physics Research Section A: Accelerators, Spectrometers, Detectors and Associated Equipment* 339.3 (1994), pp. 468 –476. ISSN: 0168-9002.

[146] F. Kaether and C. Langbrandtner. “Transit time and charge correlations of single photoelectron events in R7081 photomultiplier tubes”. In: *Journal of Instrumentation* 7.09 (2012), P09002–P09002.

[147] M. Anthony et al. “Characterization of photomultiplier tubes with a realistic model through GPU-boosted simulation”. In: *Journal of Instrumentation* 13.02 (2018), T02011–T02011.

[148] R. Saldanha et al. “Model independent approach to the single photoelectron calibration of photomultiplier tubes”. In: *Nuclear Instruments and Methods in Physics Research Section A: Accelerators, Spectrometers, Detectors and Associated Equipment* 863 (2017), pp. 35 –46. ISSN: 0168-9002.

[149] J. Aalbers. *AxFoundation/strax: v0.11.1.* Version v0.11.1. June 2020. URL: https://doi.org/10.5281/zenodo.3894675.

[150] L. Baudis et al. “A Dual-phase Xenon TPC for Scintillation and Ionisation Yield Measurements in Liquid Xenon”. In: *Eur. Phys. J.* C78.5 (2018), p. 351.

[151] F. Piastra. “Materials Radioassay for the XENON1T Dark Matter Experiment, and Development of a Time-projection Chamber for the Study of Low-energy Nuclear Recoils in Liquid Xenon”. PhD thesis. Universität Zürich, 2017. URL: `https://www.physik.uzh.ch/groups/groupbaudis/darkmatter/theses/xenon/FrancescoPiastra.pdf`.

[152] E. Aprile et al. “Observation of anticorrelation between scintillation and ionization for MeV gamma rays in liquid xenon”. In: *Phys. Rev. B* 76 (1 2007), p. 014115.

[153] L. Baudis et al. “The first dual-phase xenon TPC equipped with silicon photomultipliers and characterisation with ^{37}Ar”. In: *The European Physical Journal C* 80.5 (2020). ISSN: 1434-6052.

[154] S. Bruenner et al. *Radon daughter removal from PTFE surfaces and its application in liquid xenon detectors.* 2020. arXiv: `2009.08828`.